NANYANG TECHNOLOGICAL UNIVERSITY

SYNTHESIS OF POLYOXOMETALATE NANO-ARCHITECTURES FOR ENVIRONMENTAL APPLICATIONS

LUA SHUN KUANG

Interdisciplinary Graduate School
Nanyang Environmental and Water Research Institute/
Environmental Chemistry and Materials Centre

2017

SYNTHESIS OF POLYOXOMETALATE NANO-ARCHITECTURES FOR ENVIRONMENTAL APPLICATIONS

LUA SHUN KUANG

Interdisciplinary Graduate School
Nanyang Environmental and Water Research Institute/ Environmental Chemistry and Materials Centre

A thesis submitted to the Nanyang Technological University in partial fulfilment of the requirement for the degree of Doctor of Philosophy

2017

Acknowledgements

The journey through a PhD is never an easy one. It is the great people we meet in the process which is the most important. My utmost appreciation and gratitude is hereby express to my supervisor, Associate Professor Dong ZhiLi. It is his constant support, encouragement and guidance which allowed me to pull through with my PhD study. I will also like to express my gratitude towards my co-supervisor, Associate Professor Lim Teik Thye; my mentor, Professor Ng Wun Jern and my TAC member, Associate Professor Zhang QiChun, for their advices and assistance during this journey.

I would also like to thank my friends and family for the encouragement and support throughout this period and their understanding when I am having difficulties.

To the administrative staffs and technical staffs, Dr. Wang Bochuan Victor, Dr. Tay Yee Yan, Dr. Ang Derrick, Dr. Zviad Tsakadze, Dr. Tang Yuxin, Mr. Zhang Li-Zhi, Mr. Alan Lim Ming Pin, Ms. Sharon Tan, Ms Sandy Leong, Mr. Phon Kin Sheng, Mrs Lim-Tay Chew Wang, Mr. Ong Chee Yung, Mr. Tan Han Khiang, Mrs. Maria Chong Ai Shing and Ms. Pearlyn See Shen Yen, Dr. Ronn Goei, Mr. Jacky Khoo, Ms. Deirdre Lim, Ms. Hera Catharina Adam, I'm thankful for your time and effort in helping me throughout my time in NTU. To my group members who have left or joined the research "family" though the years, I'm thankful for being able to work with all of you.

Finally, I would like to express my sincere acknowledgement to Nanyang Technological University, Interdisciplinary Graduate School, Nanyang Environment and Water Research Institute (NEWRI) for the PhD research scholarship. I would also like to acknowledge the support by MOE Academic Research Fund (AcRF) Tier 1 RG 76/12 (M4011088.070).

Table of Contents

Summary

Polyoxometalates are unique molecular metal oxides containing early transition elements in their highest oxidation state. They have highly tuneable structure which allows their design from an atomic level, thus their potential in various applications in a wide field of research is made viable. The structural and physical properties are important understanding required in the toolbox of researchers for the design of polyoxometalates based materials. Due to their highly soluble nature, the heterogenization of polyoxometalates will be favourable from the perspective of sustainable development. The facile separation of catalyst will improve the feasibility of polyoxometalates for environmentally sustainable applications, making the synthesis and design of polyoxometalates based nano-architecture a necessary endeavour.

In the first part of the study, polyoxometalates (POMs) of the series $H_{(3+n)}[PV_nMo_{(12-n)}O_{40}]$ (PVMA) were prepared and investigated to assist in the design of POMs based materials. Basic characterizations of PVMAs were performed to understand the structural and physiochemical characteristics. Two simple design approaches: (1) surfactant encapsulation of POMs and (2) surface modification of metal oxide for immobilization of POMs were adopted with the aim of obtaining a heterogenizing PVMA. In order to further investigate the redox characteristic of PVMA, PVMA-2 was chosen for incorporation with TiO_2 for investigation of redox properties. The TiO_2 nanoplates immobilized with PVMA-2 via (3-aminopropyl)triethoxysilane as a coupling agent showed synergistic effect of PVMA-2 on TiO_2 surface and the potential of such material in application as anodes in lithium ion battery. This also provides insights for design of POMs immobilized materials for environmental applications.

In the second part of the study, amine functionalized high surface area titanate nanotube was modified with PVMA-2. The synthesis utilizes the high surface area of titanate nanotubes for immobilization of PVMA-2, obtaining heterogeneity and high surface area in the as-prepared material for application as a photocatalyst. Structural characteristics and physical properties of PVM-X%S-TNT (X = 2, 5, 10) was characterized by various

technique herein. PVM-5%S-TNT was found to be optimized for the photocatalytic degradation of MB with H_2O_2 added as an oxidant. The photocatalytic efficiency of the material was also tested against rhodamine B, methyl orange and acid orange 7. The results provided useful insights on the mechanism for photocatalytic degradation of organic dye by PVMA-2.

In the final part of this study, a series of surfactant encapsulated heteropolyanion (SEH-n) based on $H_{(3+n)}[PV_nMo_{(12-n)}O_{40}]$ (PVMAs) was prepared. The morphological optimisation of the SEHs was studied by the control of solvent polarity and PVMA to surfactant ratio used. Investigation by TEM revealed the formation of particles with multi-lamellar nano-structure in the SEHs. The performance of SEHs as catalysts for the removal of bisphenol–A under ambient conditions was evaluated. Factors influencing the performance of the SEH–n are the relative stability of the Keggin structure and electron accepting property. The hydrophobic property of the nano–sized SEHs provides good aqueous stability and allows excellent recoverability of the catalyst from the aqueous solution after treatment.

The studies show a potential for further development, design and understanding of polyoxometalates based nano-architecture which can find a niche in environmental application. The recommendations for future work are communicated in the concluding chapter.

List of Publications

Part of the findings in the following journal paper(s) were presented in this thesis:

1. S.K. Lua, W.D. Oh, L.Z. Zhang, L. Yao, T.T. Lim, Z.L.Dong (2015). A molybdovanadophosphate-based surfactant encapsulated heteropolyanions with multi-lamellar nano-structure for catalytic wet air oxidation of organic pollutant under mild conditions. *RSC Advances*, 5, 115, 94743-94751.

Co-authorship publications:

1. W.D. Oh, S.K. Lua, Z.L. Dong and T.T. Lim (2014). High surface area DPA-hematite for efficient detoxification of bisphenol A *via* peroxymonosulfate activation. *Journal of Materials Chemistry A*, 38, 15836-15845.
2. L. Yao, S.K. Lua, L.Z. Zhang, R. Wang and Z.L. Dong (2014). Dye removal by surfactant encapsulated polyoxometalates. *Journal of Hazardous Materials, 280, 428-435.*
3. C.M. Fan, M.D. Regulacio, Y. Chen, S.H. Lim, S.K. Lua, Q.H. Xu, Z.L. Dong, A.W. Xu and M.Y. Han (2014) Colloidal nanocrystals of orthorhombic Cu2ZnGeS4: phase-controlled synthesis, formation mechanism and photocatalytic behaviour. *Nanoscale*, 7, 3247-3253.
4. W.D. Oh, S.K. Lua, Z.L. Dong and T.T. Lim (2015). Performance of magnetic activated carbon composite as peroxymonosulfate activator and regenerable adsorbent *via* sulfate-radical mediated oxidation processes. *Journal of Hazardous Materials*, 284, 1-9.
5. W.D. Oh, S.K. Lua, Z.L. Dong and T.T. Lim (2015). A novel three-dimensional spherical $CuBi_2O_4$ consisting of nanocolumn arrays with

persulfate and peroxymonosulfate activation functionalities for 1H—benzotriazole removal. *Nanoscale*, 7, 8149 – 8158.

6. W.D. Oh, S.K. Lua, Z.L. Dong and T.T. Lim (2015). Rational design of hierarchically-structured $CuBi_2O_4$ composites by deliberate manipulation of the nucleation and growth kinetics of $CuBi_2O_4$ for environmental applications. *Nanoscale*, 8, 2016 – 5054.

Table Captions

Figure Captions

Main text typed in Times New Roman, Size 12. Must start on odd page (right hand page). Figures must be numbered sequentially within chapters.

Figure 2.1. Structure of isopolyanion (a) Lindqvist, M6O19; heteropolyanions (b) Keggin, XM12O40 and (c) Dawson, X2M18O64; Molybdenum-blue (d) Mo154 and (e) Mo368.

Figure 2.2. Periodic table showing polyoxometalates forming elements.

Figure 2.3 The formation of Keggin structure $[XM_{12}O_{40}]^{n-}$.

Figure 2.4 The structural hierarchy of heteropolyanion showing the primary Keggin structure, secondary structure and tertiary structure. Reproduced from ref.[3] with permission from The Royal Society of Chemistry.

Figure 2.5 The different rotational isomers of the Keggin structure.

Figure 2.6 Lacunary species formed from Keggin-type heteropolyanion[1].

Figure 2.7 Polyhedra representation of a "sandwich-type" heteropolytungstate. The different types of tungsten atoms are labelled a1, a2, a3, b and c. The mimicked M oxide surface occupies the four central edge linked polyhedra. Adapted with permission from Journal of the American Chemical Society[16].

Figure 2.8 (a) Anderson-Evans structure and (b) Dexter-Silverton structure heteropolyanion.

Figure 2.9 The distribution of 12:1 molar ratio of [MoO4]2- and [HPO4]2-at different pH values. Adapted with permission from ref.[10]. Copyright 1986 American Chemical Society.

Figure 2.10 Ball and stick structure of mixed-addenda [PVnMo12-nO40] (a) n = 0, (b) n = 1 and (c) n = 2 Adapted with permission from ref [7]. Copyright 2011 American Chemical Society.

Figure 2.11 Cyclic Voltammogram of Keggin $[PMo_{12}O_{40}]^{3-}$ in 50% ethanol/water mixture containing 0.1 M HCl. Copyright 1991 Wiley. Used with permission from reference[12].

Figure 2.12 Keggin polyoxometalate, PMo12O403- undergoing 24 electrons redox process, acting as an "electron-sponge". Reprinted with permission from reference[14]. Copyright 2012 American Chemical Society.

Figure 2.13 Three types of heterogeneous catalysis by heteropolyanions.

Figure 2.14 The key strategies for preparation of heterogeneous polyoxometalates-based catalyst. Reproduced from reference[5] with permission of The Royal Society of Chemistry.

Figure 2.15 (a) TEM image and SAED pattern of $H_3PW_{12}O_{40}/TiO_2$nanocomposite, (b) UV-vis diffuse reflectance spectra of TiO_2, $H_3PW_{12}O_{40}$ and $H_3PW_{12}O_{40}/TiO_2$ composite. Visible photocatalytic degradation of various dyes using the nanocomposite. Reprinted from reference[18]. Copyright 2005. With permission from Elsevier.

Figure 2.16 FESEM images of (a) TiO_2 nanotubular array, and cross-sectional SEM images of (b) TiO_2 tubules, (c) $PW_{12}O_{40}$-TiO_2 tubules, and (d) enlarged view of $PW_{12}O_{40}$-TiO_2 tubules. Reproduced from reference[6].

Figure 2.17 SEM images of (a-c) 3DOM-TiO_2, (d-f) 3DOM PW_{11}Co-APS-TiO_2 and (g-i) PW_{11}Co-APS-TiO_2. Reprinted from reference[17]. Copyright 2014. With permission from Elsevier.

Figure 3.2 XRD diffractogram of FTIR spectra of (a) $H_4[PVMo_{11}O_{40}]$, (b) $H_5[PV_2Mo_{10}O_{40}]$ and (c) $H_6[PV_3Mo_9O_{40}]$ with the characteristic reflection peaks of the Keggin structure labelled.

Figure 3.3 Thermogravimetric analysis weight loss profile of (a) $H_4[PVMo_{11}O_{40}]$, (b) $H_5[PV_2Mo_{10}O_{40}]$ and (c) $H_6[PV_3Mo_9O_{40}]$.

Figure 3.4 (a) Schematic of PVMA-2 modified TiO2 NP synthesis. As synthesized TiO2 (b) SEM micrograph and (c) EDX spectra. PVMA-2 modified TiO2 (d) SEM micrograph and (e) EDX spectra. Solvothermal synthesis (f) without PVMA-2 in aqueous layer and (f) with APTES in organic layer.

Figure 3.5 XRD diffractogram of (a) $H_5[PV_2Mo_{10}O_{40}]\cdot 29H_2O$, TiO_2 synthesized (b) without PVMA-2 in aqueous layer, (c) with PVMA-2 in aqueous layer and (d) PVMA-2 modified TiO_2 NPs (TiO_2-PVM).

Figure 3.6 TEM micrograph of TiO_2 NP (a) at low magnification (inset shows the corresponding SAED pattern taken close to [100] zone axis) (b) at high magnification. TEM micrograph of TiO_2-POM (c) at low magnification and (d) at high magnification (inset shows corresponding SAED pattern).

Figure 3.7 (a) FTIR spectra of (i) PVMA-2, (ii) TiO_2 NP, (iii) APTES modified TiO_2 NP and (iv) TiO_2-PVM. (b) N_2 adsorption/desorption isotherm of (i) PVMA-2, (ii) TiO_2 NP and (iii) TiO_2-PVM.

Figure 3.8 Cyclic voltammograms of (a) TiO_2, (b) PVM and (c) TiO_2-PVM electrodes at 0.01-3 V potential window and a scan rate of 0.2 mV s^{-1} for the first three cycles. Galvanostatic discharge-charge voltage profiles at 0.1 A g^{-1} for the 1st, 2nd, 5th and 10th cycle of (d) TiO_2, (e) POM and (f) POM-TiO_2 electrode.

Figure 3.9 (a) Rate capability of the TiO_2, PVMA-2 and TiO_2-PVM electrodes at various current densities. (b) Cycling performance of the as-prepared samples at 10.0 A g^{-1}. All of the measurements were evaluated at potential range of 0.01-3 V.

Figure 3.10 (a) Equivalent circuit for electrochemical system. (b) Nyquist plots of as-prepared samples.

Figure 3.11 Characterizations of POM-TiO2 electrode after 100 cycles: (a-b) Low-magnification TEM images; (c) high-magnification TEM image with inset SAED pattern; (d) HAADF image and its corresponding elemental mapping images of (e) P, (f) V, (g) Mo, (h) O and (i) Ti elements.

Figure 4.1 (a) Schematic of P-TNT preparation and surface modification with POMs, SEM micrograph of (b) P-TNT, (c) PVM-2%S-TNT, (d) PVM-5%S-TNT and (e) PVM-10%S-TNT.

Figure 4.2 FTIR spectra of (a) $H_5[PV_2Mo_{10}O_{40}]$, (b) P-TNT, (c) PVM-2%S-TNT, (d) PVM-5%S-TNT and (e) PVM-10%S-TNT.

Figure 4.3 FESEM Dark Field micrograph of (a) P-TNT, (b) PVM-2%S-TNT, (c) PVM-5%S-TNT and (d) PVM-10%S-TNT.

Figure 4.4 XPS spectra of (a) PVM-2%S-TNT, (b) PVM-5%S-TNT and (c) PVM-10%S-TNT.

Figure 4.5 XPS spectra of Mo 3d5/2, V 2p and Ti 2p of PVM modified materials.

Figure 4.6 N_2 adsorption desorption isotherm of (a)(i) $H_5[PV_2Mo_{10}O_{40}]$, (ii) P-TNT, (iii) PVM-2%S-TNT, (iv) PVM-5%S-TNT and (v) PVM-10%S-TNT. (b) Pore size distribution of (i) P-TNT and (ii) PVM-5%S-TNT.

Figure 4.7 XRD diffractogram of (a) $H_5[PV_2Mo_{10}O_{40}]$, (b) P-TNT, (c) PVM-2%S-TNT, (d) PVM-5%S-TNT and (e) PVM-10%S-TNT.

Figure 4.8 HRTEM micrograph showing the local structure of P-TNT (a) low magnification, (b) high magnification; PVM-2%S-TNT (c) low magnification, (d) high magnification; PVM-5%S-TNT (e) low magnification, (f) high magnification; PVM-10%S-TNT (g) low magnification, (h) high magnification

Figure 4.9 UV-Vis spectra of as prepared P-TNT and PVM-X%S-TNT (X= 2, 5, 10).

Figure 4.10 Photocatalytic activity of PVM-X%S-TNT (X= 2, 5, 10) under simulate visible light irradiation (Xe arc lamp 150 W, 420-630 nm, intensity 409 W m^{-2}). [MB] = 5 mg L^{-1}, catalyst dosage = 0.4 g L^{-1}, pH = 2 (inset shows adsorption of MB by the materials in 60 min) (b) Photocatalytic activity of PVM-X%S-TNT (X= 2, 5, 10) under simulated visible light irradiation. [MB] = 5 mg L^{-1}, catalyst dosage = 0.4 g L^{-1}, pH = 2, $[H_2O_2]$ = 98 mM. (c) UV-vis spectroscopy of MB showing a decrease in concentration over time.

Figure 4.11 Effect of (a) different H_2O_2 concentration. [MB] = 5 mg L-1, catalyst dosage = 0.4 g L-1, pH = 2 and (b) different catalyst loading of PVM-5%S-TNT on the degradation of MB.

Figure 4.12 (a) Effect of pH on degradation of MB (inset shows colour of catalyst recovered), (b)(i) Degradation of different dye using PVM-5%S-TNT, structure of (ii) methylene blue, (iii) rhodamine B, (iv) methyl orange and (v) acid orange 7.

Figure 4.13 Suggested mechanism for photocatalytic activity of PVM-X%S-TNT under visible light irradiation.

Figure. 5.1 SEM micrograph of (a) PVMA–2, (b) casted film of SEH, (c) bulk powder of SEH, (d) PVMA-2: DMDOA in ~1:2 ratio, (e) PVMA-2:DMDOA in ~1:3 ratio and (f) SEH from mixed solvent of chloroform : n-butanol in 3:1 ratio.

Fig. 5.2 Schematic illustration for synthesis and formation of SEH-2 from PVMA-2 and influence of DMDOA:HPA ratio.

Fig. 5.3 High-resolution TEM micrograph of (a) SEH–1, (b) SEH–2, (c) SEH–3 and (d) SEH–2 at showing lattice fringes about 0.2 nm d-spacing inside each Keggin cluster with a diameter of ca. 1 nm (white circles).

Figure 5.4 XRD patterns of PVMA-1, DMDOA·Br, SEH-1, SEH-2 and SEH-3. The peaks of PVMA-1 are indexed to single phase $H_4PVMo_{11}O_{40}$. Peaks in all SEHs between 15-25° indicate the presence of MLNS.

Fig. 5.5. BET sorption isotherm of (a) PVMAs and (b) SEHs. (c) FTIR of (i) $H_4[PMo_{11}VO_{40}]$, (ii) dimethyldioctadecylammonium bromide (iii) SEH–1, (iv) SEH–2 (v) SEH–3. (d)Thermo-gravimetric analysis weight loss profile of (i) SEH–1 (ii) SEH–2 (iii) SEH–3.

Figure 5.6 (a) Removal efficiency of BPA using SEHs and PVMA–2 without aeration. (b) Removal efficiency of BPA using SEHs and PVMA–2 with aeration.

Figure 5.7 (a) BPA removal without aeration by (i) DMDOA:MVPA-2 2:1, (ii) DMDOA:MVPA-2 3:1 prepared with chloroform : *n*-butanol in 3:1 ratio; and (iii) DMDOA:MVPA-2 5:1 in pure chloroform. BPA removal with aeration by (iv) DMDOA:MVPA-2 2:1, (v) DMDOA:MVPA-2 3:1 prepared with chloroform : *n*-butanol in 3:1 ratio; and (vi) DMDOA:MVPA-2 5:1 in pure chloroform. (b) BPA removal using SEH–2 with aeration and in argon purged solution, showing limited adsorption effects in the absence of oxygen.

Figure 5.8. BPA removal efficiency (a) at pH3, pH9 and without pH adjustment; (b) at different SEH loading of 1.0, 0.8, 0.5, 0.2 g L^{-1} and (c) at initial BPA concentration of 20, 10, 5 mg L^{-1}.

Figure 5.9 XPS analysis results of SEH-2 (a) (i) before catalytic experiment and ii) after catalytic experiment. XPS spectra of (b) Mo and (c) V (blue = before catalytic experiment, red = after catalytic experiment).

Figure 5.10 (a) FTIR spectrum of fresh SEH–2 and used SEH–2. Fresh catalyst exhibits characteristic peaks of water, while the used catalyst shows no presence of water after drying post usage. The Characteristic peaks of MVP–2 and DMDOA are consistent before and after catalytic procedure. (b) BPA removal by SEH-2 over 3 consecutive cycles,

Abbreviations

ANSTO	Australian Nuclear Science and Technology Organization
ATR	Attenuated Total Reflectance
BEI	Backscatter Electron Images
BSE	Backscattered Electron
BVS	Bond Valence Sum
EDS	Energy Dispersive X-ray Spectroscopy
EPMA	Electron Probe Microanalysis
FTIR	Fourier Transform Infrared Spectroscopy
HRTEM	High Resolution Transmission Electron Microscopy
PXRD	Powder X-ray Diffraction
SAED	Selected Area Electron Diffraction
SEM	Scanning Electron Microscopy
SEI	Secondary Electron Images
TEM	Transmission Electron Microscopy
XRD	X-ray Diffraction
Z	Atomic Number

Chapter 1

Introduction

In this chapter, the background, objective, overview and outcomes of this dissertation will be presented. The key areas and insufficiency in related research and the motivation of this work will be highlighted. In the objective section, the goal of this dissertation which is to design polyoxometalates nano-architecture as a catalyst based on their redox and photoredox properties and eventually explore their potential environmental applications. Outcomes of individual chapters covered in this dissertation will be highlighted in the overview section.

1.1. Background

Polyoxometalates are early transition metal oxides clusters in their highest oxidation state[12]. Due to their highly alterable chemical and physical properties, which can be adjusted according to specific requirements of reactions or application over a range of sizes from atomic or molecular level to nanomaterials or even microstructures, attention on polyoxometalates is seeing an increase in recent years[19-24]. The application of polyoxometalates in various fields i.e. in analytical chemistry[25], material science[26], magnetism[27], medicine[28], memory devices[29] and photochemistry[30] have been studied by various research groups. However, their application in catalysis[31] is still the most prominent due to their interesting redox[32] and semiconductor-like[33] properties. Early research of polyoxometalates were performed to study their properties in homogeneous catalysis of organic pollutants[34-38] and removal of metal ions[39,40]. However, from the perspective of sustainable development, it is essential to prepare heterogenized polyoxometalates to improve their viability in practical application.

Metal oxide have mainly been the material of choice as catalyst for removal of organic pollutants via advanced oxidation processes[41,42]. The most well know and studied metal oxide is titanium dioxide which is highly valued due to its low toxicity, high stability, insoluble and resistant to most chemicals[43]. However, it is also well known that titanium dioxide works as a photocatalyst under ultraviolet radiation due to the large bandgap of ~ 3.2 eV[44]. Even though there are methodologies[45] which allow the bandgap to be tuned towards visible light harvesting, but this remains a challenge to researchers. In view of such a problem, polyoxometalates which are easily tuneable from atomic or molecular scale are potential solution for preparing of environmentally friendly material for environmental applications.

While a homogeneous system for catalysis favours higher activity, a heterogeneous system has several advantages:

1. Facile separation of catalyst from reaction for reuse and recycling
2. Reduces the dissolution of catalyst leading to secondary pollution of dissolved

metals.

3. Improvement of stability of polyoxometalates which dissociate to form component oxide anions under low concentration.[46]

It is thus imperative to undertake the design of polyoxometalates-based heterogeneous catalysis *via* formation of nano-architecture for their application as functional materials. In recent years, the application of nanoparticles towards the removal of micropollutants is receiving increased attention [47]. The polyoxometalates (POMs) nano-architecture catalyst developed in this project may be applied after the ultrafiltration step of the secondary effluent treatment process. The application and effectiveness of POMs-based catalyst with nano-architecture could be investigated with other toxic organics present in wastewater.

1.2. Knowledge gap and motivation

In the application of polyoxometalates as heterogeneous catalyst, various strategies have been adopted in their preparation. Some of the recent advances are well covered in a recent review by Zhou et. al.[5] for liquid-phase organic transformation and Marci et. al.[48] for photocatalysis. While it is encouraging to see reports and studies of polyoxometalates in catalytic system, the process for the preparation of the material are often neglected. As the process for preparation of these materials is intrinsic to their effectiveness as catalyst, it is important to carefully characterize and elucidate the role of polyoxometalates in the catalytic processes. Therefore, the preparation of polyoxometalates nano-architectures and how the design influences their effectiveness represents an area of study necessary for future development.

They key motivation of this research is the interdisciplinary study and development of catalytic material as sustainable technologies. Wastewater treatment technologies represents an important aspect in safeguarding of our water sources. This is especially important in Singapore as the wastewater here is being used as the feed water to be used for the production of NEWater [49]. Wastewater comes from combined sewage from domestic, municipal and industrial origins and contains a wide spectrum of chemicals and

pathogens [50]. Therefore, different treatment technologies must be adopted to effectively treat the wastewater, to remove the various constituents to acceptable levels before the water could be further treated at the water reclamation plants. A convenient classification of these treatments are: physical treatments, chemical treatments, combination of physical and chemical treatments and biological treatments.

Based on the composition of the wastewater, as no single treatment can completely remove the complex matrix of components in wastewater, different treatments must be applied to effectively remove them. Typically, in a centralized wastewater treatment plant, preliminary treatment is carried out by screening off debris and sandy materials, this is followed by primary treatment in a primary clarifier by gravitational sedimentation process. In the secondary treatment, aeration tanks with activated sludge is used to degrade organic pollutants especially biochemical oxygen demand (BOD) in the wastewater. The water is then passed on to the final clarifier and the clear supernatant is discharged as the secondary effluent [51]. After this treatment process, removal BOD and suspended solids up to 90 % is typically achieved.

At this stage, the secondary effluent still contains low amounts of suspended solids, inorganics, virus, bacterial, protozoa and organics. The water will then undergo microfiltration/ultrafiltration which removes most of the remaining turbidity, bacteria and protozoa. Various advance oxidation processes [52] could be applied on the secondary effluent at different stages to removal micropollutants. The primary target here are the micropollutants which remain within the water matrix. Even though most micropollutant are biodegradable to varying extents, long period of time is required to effectively remove them via biological processes [53].

The process of secondary effluent treatment includes ultrafiltration, reverse osmosis and UV-disinfection. The proposed application of the catalyst after ultrafiltration also improves the recoverability of the catalyst with less particulate contaminant. The reduction in undesirable matrix present after the ultrafiltration process will minimize potential fouling and thus extend the useful lifetime of the catalytic material. The removal

of organic pollutants by the catalyst at this stage of the wastewater treatment process also reduces the components which may lead to fouling of the reverse osmosis membrane in the later stage of the treatment process.

An additional separation unit could be added after the catalytic oxidation treatment and the catalyst could be recovered for reuse again. Possible ways of catalyst separation could be achieved by magnetic separation via incorporation of magnetite nanocrystals with POMs [13]. Use of the POMs based nano-architecture catalyst could also see possible application in specific industry if they exhibit high efficiency in removal of certain organics present in the industrial effluents.

Polyoxometalates are easily tuneable from atomic or molecular scale is a potential solution for preparing of environmentally friendly material for environmental applications. This allows us to prepare the materials which are benign for application and during the usage life-cycle of the material. In the consideration of the support material systems, TiO_2 has long been a long favoured material due to its low cost, low toxicity, stability and availability. For the use of surfactant, the stability of the catalyst and ease of control of morphology by surfactant and solvent in the construction of nano-architecture are the primary reasons for this material system. Furthermore, the potential of such nano-architectures which can be carefully designed for environmental application is a frontier which scientific exploration is warranted. With the above target as motivation, this study aims to design and synthesize polyoxometalates based nano-architectural material as catalyst.

1.3. Objective and scope

The use of the prepared material lies at the heart of wastewater treatment processes, which is why a strong foundation in the preparation and understanding of these polyoxometalates based material, is essential. The scope of work covered in each part of the study is outline below:

1. Synthesis of mixed-addenda transition metal substituted polyoxometalates $H_{3+n}PV_nMo_{12-n}O_{40}$ (n= 1, 2, 3).
   a. Synthesis of titanium dioxide nano-structure for immobilization with polyoxometalates
   b. To prepare a nano-architecture *via* immobilize polyoxometalates on titanium dioxide surface using coupling agent.
   c. To investigate the redox properties of immobilized polyoxometalates as environmentally friendly rechargeable battery component.
2. Fabrication of polyoxometalates immobilized on high surface area titanate nanotubes for polyoxometalates immobilization.
   a. To optimize the surface modification for effective functionalization.
   b. To evaluate the performance of the prepared material as a visible light activated photocatalyst.
3. Heterogenization of polyoxometalates *via* surfactant encapsulation strategy.
   a. To understand the influence of solvent and surfactant ratio in the formation of surfactant encapsulated polyoxometalates nano-architecture.
   b. Evaluation of surfactant encapsulated polyoxometalates as a catalyst for wet air oxidation of bisphenol A (BPA) under ambient condition.
   c. To investigate the mechanism of BPA removal using surfactant encapsulated polyoxometalates.

1.4. Dissertation Overview

The dissertation addresses the design and synthesis of polyoxometalates nano-architectures which is fundamental to effectively evaluate their potential environmental applications.

Chapter 1 provides a background of polyoxometalates as catalyst and the motivation for the research, followed by the presentation of the outlines and scope of the dissertation.

Chapter 2 reviews the literature concerning the structural, physical and chemical

properties of polyoxometalates. The understanding of these properties is necessary for researchers practicing within the field. The strategies for heterogenization of polyoxometalates and their environmental applications are covered with specific emphasis.

Chapter 3 describes the synthesis of $H_{3+n}PV_nMo_{12-n}O_{40}$ (n= 1, 2, 3) polyoxometalates and their use in the preparation of the nano-architectural design. Based on the surface immobilization of polyoxometalates on TiO_2 nanoplates, the redox properties of the design were elucidated through its application as a rechargeable lithium ion battery catalyst.

Chapter 4 further develops from the previous chapter by immobilizing the polyoxometalate on high surface area titanate nanotubes. The surface modification was optimized and the material was evaluated for photocatalytic degradation of methylene blue.

Chapter 5 employs a surfactant encapsulation strategy to prepare polyoxometalates heterogeneous catalyst with multi-lamellar-nano-structure. The catalyst was evaluated for the catalytic wet air oxidation of bisphenol A.

Chapter 6 presents a summary of all the major findings in this dissertation with some recommendations for future work.

Chapter 2

Literature Review

Polyoxometalates are unique molecular metal oxides containing early transition elements in their highest oxidation state. They have highly tuneable structure which allows their design from an atomic level, thus their potential in various applications in a wide field of research is made viable. The structural and physical properties are important understanding required in the toolbox of researchers for the design of polyoxometalates based materials. Due to their highly soluble nature, the heterogenization of polyoxometalates will be favourable from the perspective of sustainable development. The facile separation of catalyst will improve the feasibility of polyoxometalates for environmentally sustainable applications. Particular focus on heterogenization strategies by immobilization on titanium oxide and solidification by organic cations is discussed along with some areas of application.

2.1. Introduction

The development, design and engineering of new generation functional materials applying a bottom up approach[54-56] in synthesis is of great value and interest to researchers, as such strategies have fundamental importance in the progression of science and technology. The preparation of materials *via* such methodology allows the consideration of factors like active sites, uniform composition and distribution, thus providing more robust and reliable synthesis protocols. The successful design of such material is however impossible without the fundamental knowledge of active species and shedding light on their structure and nature of their reactivity. The formulation requirements for the composition and structure is therefore highly important to establish structural-reactivity relationships for the preparation of new generation of advanced functional materials.

The foundation of which this thesis is formed upon is the motivation to develop advanced functional material based on nano-architectural design of relevant precursors in the preparation of heterogeneous catalysts. The primary target of design for incorporation of an active precursor in the preparation of functional material is polyoxometalates. Polyoxometalates can be simply defined as early-transition metal-oxygen-anion clusters and has seen rapid growth in application as a catalyst in recent years[20,48,57,58].

Polyoxometalates as a metal oxide with discrete molecular structure are usually composed of early transition metals in their d^0 or d^1 electronic configuration. The most common early transition metals seen in polyoxometalates are tungsten (W(VI)), molybdenum (Mo(V), (VI)) and vanadium (V(V)). These metals are bridged by oxygen atoms and based on isolobal analogy, substitutions can be made which can enrich polyoxometalates physiochemical properties[59]. Therefore, polyoxometalates has also found applications in analytical chemistry[25], material science[26], magnetism[27], medicine[28], memory devices[29] and photochemistry[30]. Since catalysis improves the efficiency of reaction processes, it is therefore the economic driving force of polyoxometalates research. Many transition metals oxides are known to exhibit wide range of reactivity in organic synthesis[60], playing the role of good heterogeneous catalysts. Use of polyoxometalates for reaction like methanol oxidation[61] and olefin

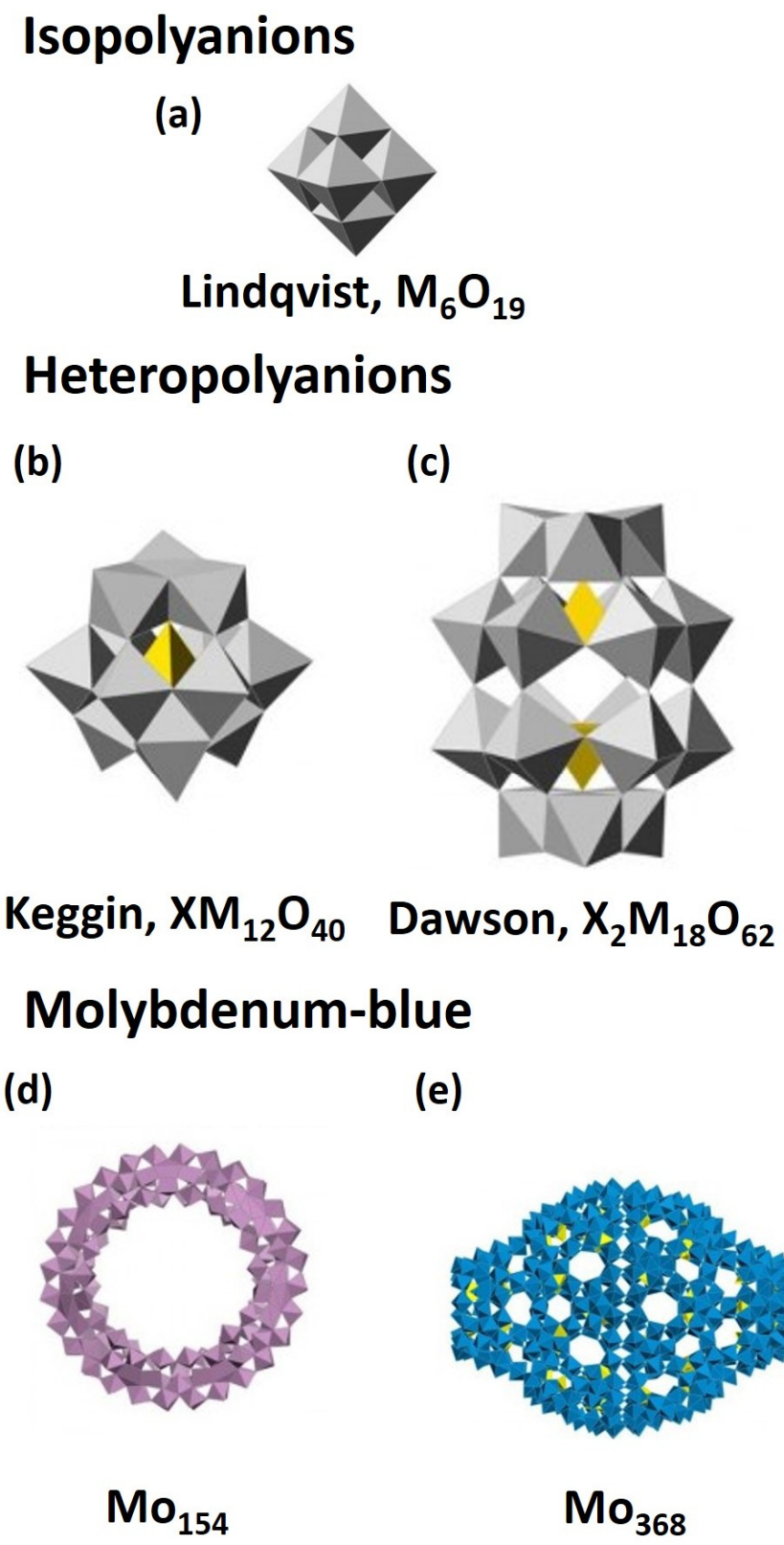

Figure 2.1 Structure of isopolyanion (a) Lindqvist, M_6O_{19}; heteropolyanions (b) Keggin, $XM_{12}O_{40}$ and (c) Dawson, $X_2M_{18}O_{64}$; Molybdenum-blue (d) Mo_{154} and (e) Mo_{368}.

epoxidation[62,63] are well documented and they are recognised as a soluble oxide analogues. This makes polyoxometalates good representation of surface models for mechanism studies in catalytic reactions[16]. The versatility of polyoxometalates as catalyst and their compatibility with environmental friendly oxidants like O_2 and H_2O_2 directs the needed attention and focus on their applications.

2.2. The structures of polyoxometalates

Polyoxometalates can be largely classified into three categories: isopolyanions, heteropolyanions and molybdenum-blue and molybdenum-brown reduced polyoxometalates centres[64]. The categories above also represent the versatility in size of polyoxometalates. For example, isopolyanions such as. Lindqvist $Mo_6O_{19}^{2-}$ (Figure 2.1(a)) are less than 1 nm in diameter[65]. Heteropolyanion of Keggin $XM_{12}O_{40}$ (Figure 2.1(b)) or Wells-Dawson $X_2M_{18}O_{62}$ (Figure 2.1(c)) structure are approximately 1 nm in diameter. Reduced molybdenum-blue like Mo_{154} (Figure 2.1(d)) with car-tire-shaped ring structure[66] or "hedgehog-like"[67] cluster of Mo_{368} (Figure 2.1(e)) with diameter of 3.5 and 6 nm respectively. The above examples and a vast number of other polyoxometalates can be generally prepared in aqueous medium by acidification and with control of various reaction conditions, i.e. type and concentration of metal oxide anions, pH and type of acid, concentration and type of electrolyte, concentration of heteroatom, introduction of additional ligands, addition of reducing agents and adjustments of temperature and solvent.

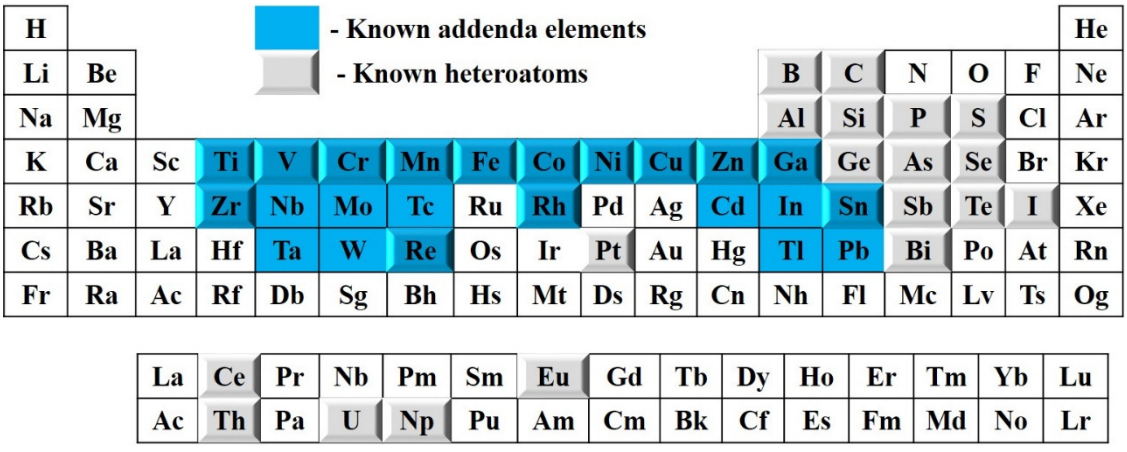

Figure 2.2 Periodic table showing polyoxometalates forming elements.

To obtain a further understanding of polyoxometalates, it is necessary to learn of the terminology used in the field. The simplest polyoxometalates, isopolyanion of Lindqvist structure has a general formula of $M_6O_{19}^{2-}$, where early transition M are generally known as the addenda atoms. The shift towards heteropolyanion involves the presence of a heteroatom. This is exemplified by the Keggin structure $XM_{12}O_{40}$ where X as the heteroatom acts as a template for the condensation of the transition metal oxide anions by introduction of PO_4^{3-} and SiO_4^{4-} forming the centre XO_4 in Keggin structure. Figure 2.2. shows the most common early transition elements found as addenda atoms in polyoxometalates[68].

While the best candidates for addenda atoms of polyoxometalates are vanadium (V), chromium (Cr), niobium (Nb), molybdenum (Mo), tantalum (Ta) and tungsten (W), largest amount of known polyoxometalates are formed by V, Mo and W. Polychromate, polyniobates and polytantalate are less observed due to limitation in oxygen coordination numbers of these elements in aqueous solution. Since the formation of polyoxometalates structure is likely through the addition of tetrahedral monomeric units, while Cr is preferentially 4 coordinate and Ta and Nb are preferentially 6 coordinate, this increases the difficulty of these elements forming polyoxometalates. The most common heteroatom in the formation of heteropolyanions can also be seen in Figure 2.2. In the Keggin structure, the structure is based on these heteroatoms position in the centre as a XO_4 tetrahedron, which is surrounded by 4 groups of M_3O_{13} trimers, formed from three groups of edge-sharing MO_6 octahedra as shown in Figure 2.3. to summarise the formation of the structure, it is useful to look at the following reactions for the polycondensation formation of polyoxometalates:

$$6VO_4^{3-} + 10H^+ \rightarrow [V_6O_{19}]^{8-} + 5H_2O \qquad \text{Eqn (2.1)}$$

$$PO_4^{3-} + 12MoO_4^{2-} + 24H^+ \rightarrow [PMo_{12}O_{40}]^{3-} + 12\,H_2O \qquad \text{Eqn (2.2)}$$

The polycondensation reaction with vanadium and molybdenum oxides in Eqn (2.1) and (2.2) shows the adoption of 6 coordinate from 4 coordinate metal-oxygen bonding. This give rise to the formation of the basic unit commonly referred to as the primary structure in Figure 2.4. Incorporation of counter-cations along with several primary

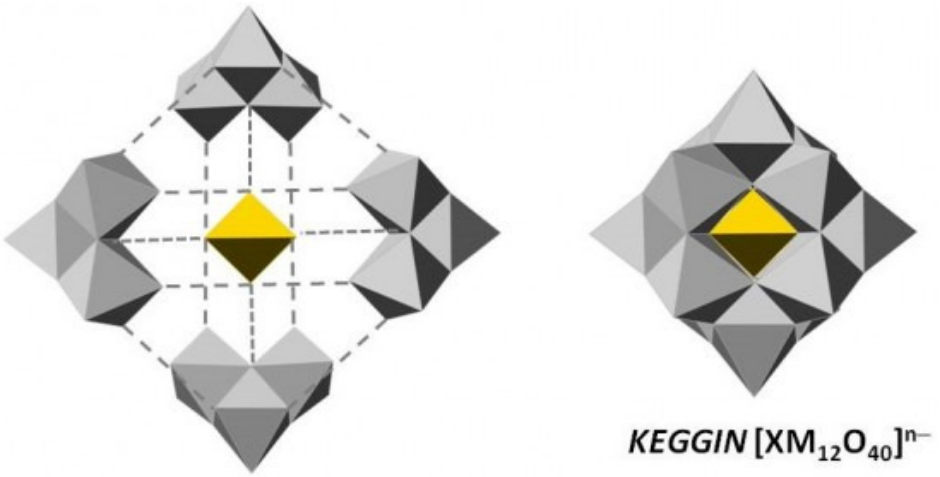

Figure 2.4 The formation of Keggin structure $[XM_{12}O_{40}]^{n-}$.

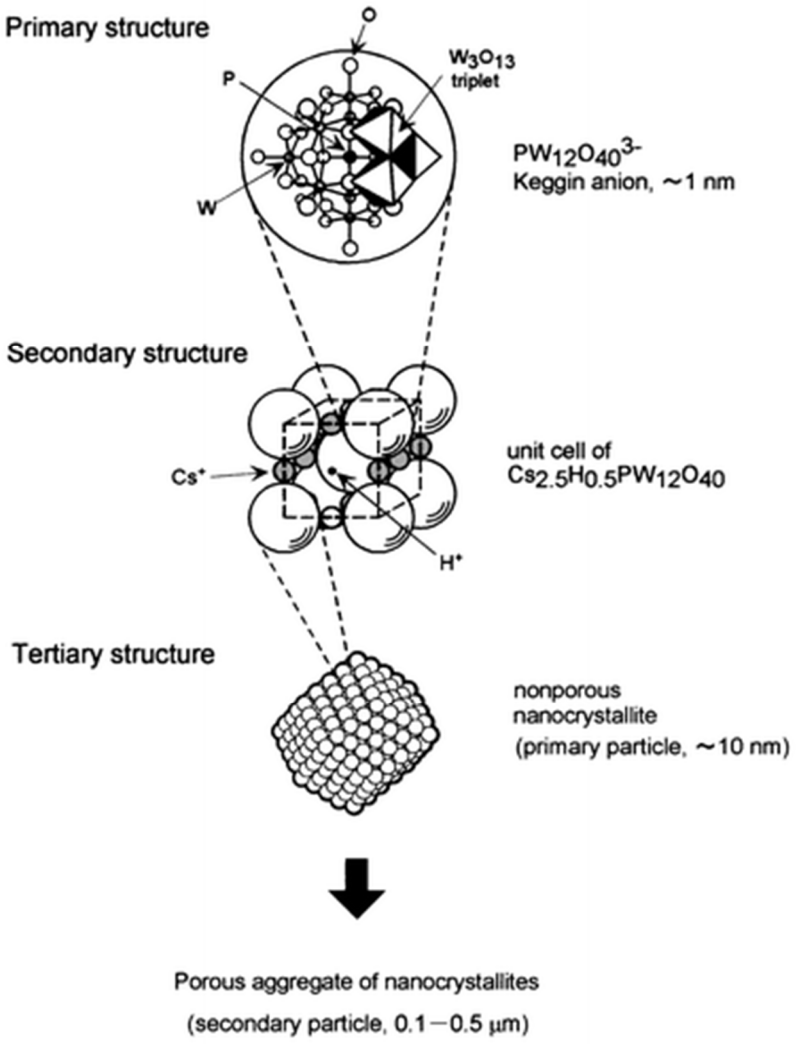

Figure 2.3 The structural hierachy of heteropolyanion showing the primary Keggin structure, secondary structure and tertiary structure. Reproduced from ref.[3] with permission from The Royal Society of Chemistry.

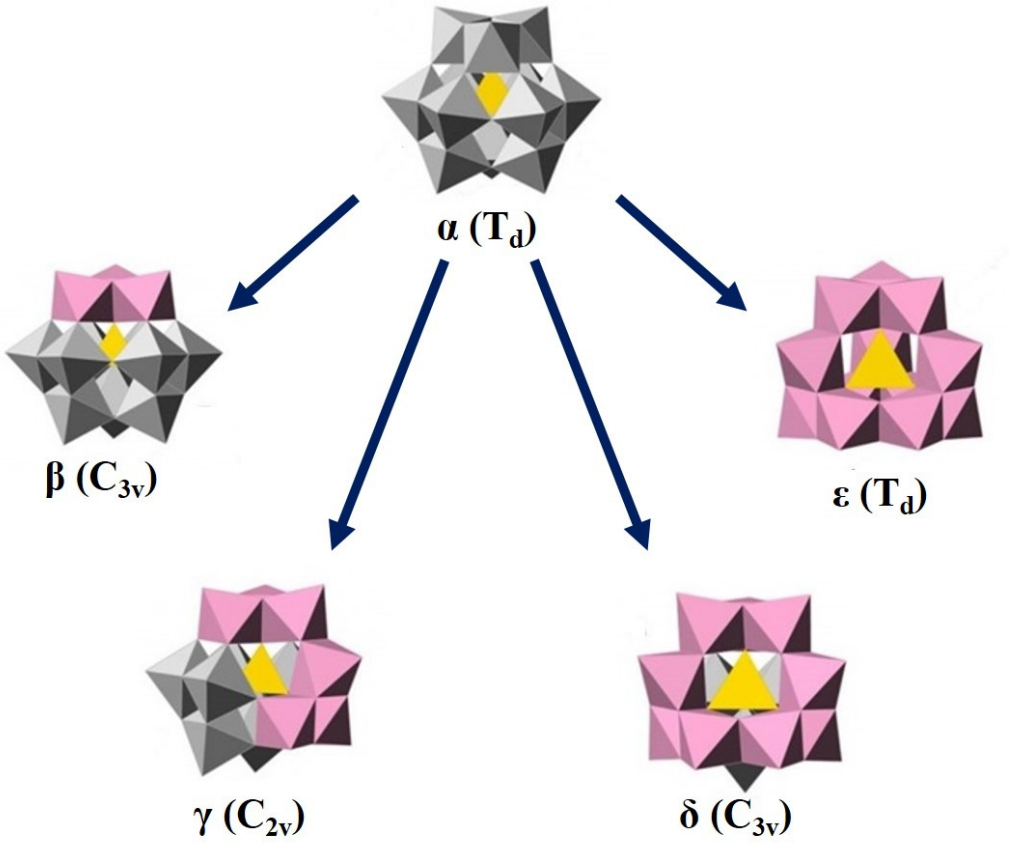

Figure 2.5 The different rotational isomers of the Keggin structure.

units forms the basis of the secondary structure, giving the crystal structure and packing of heteropolyanions. In the case when the counteraction is H^+, the water of crystallisation in the heteropolyanion will lead to the formation of a dioxonium ion, $H_5O_2^+$ which links four Keggin anions together[69]. The water molecules present in the acidic form of heteropolyanion greatly influence the adsorption and catalytic properties[3,70]. These water molecules can be easily lost with increase in temperature and are completely removed when dehydrated up to ca. 350 – 500 °C. This also means that in the acidic form, the loss of water leads to the removal of the dioxonium ions, thus contributing to the thermal instability of heteropolyanions. However, the thermal stability can be improved with appropriate counter-cations. With the assembly of the secondary structure into solid particles, the tertiary structure is formed and this contributes to properties like particle size, pore structure and surface area[31].

In addition, each of the M_3O_{13} trimers around the Keggin-type heteropolyanions can rotate about their axis by 60°, giving rotational isomers[71]. The native form of the Keggin structure is the α-isomer, while the rotation of the trimers forms the β, γ, δ and

ε isomers and the symmetry of the structure changes as summarised in Figure 2.5. The most stable isomers are the α and β form as there are less edge-sharing octahedral in the structure, giving more linear M-O-M bonds and d-orbital to p-orbital π interactions[72]. The numbers of possible isomers increase greatly with the formation of mixed-addenda heteropolyanion, e.g. $[SiW_{10}V_2O_{40}]^{6-}$. When the $[SiW_{10}V_2O_{40}]^{6-}$ anion has an α configuration, a total of five positional isomers are possible, this increases to 13 isomers when a β anion structure is adopted. The synthesis of mixed-addenda heteropolyanion can be achieved by the mixing of stoichiometric amount of the related oxide, while other synthetic route allows the access to mix-addenda heteropolyanion *via* the formation of lacunary species.

Lacunary species adds to the diversity of polyoxometalates chemistry and structure when vacant site are made available by adjustment in solution pHs. For example, the Keggin structure is able to have some of the MO_6 octahedra removed by pH adjustment towards basic conditions to form mono-, di- or tri-vacant lacunary species. Only the α, β and γ isomers are known to form lacunary species, possibly due to these

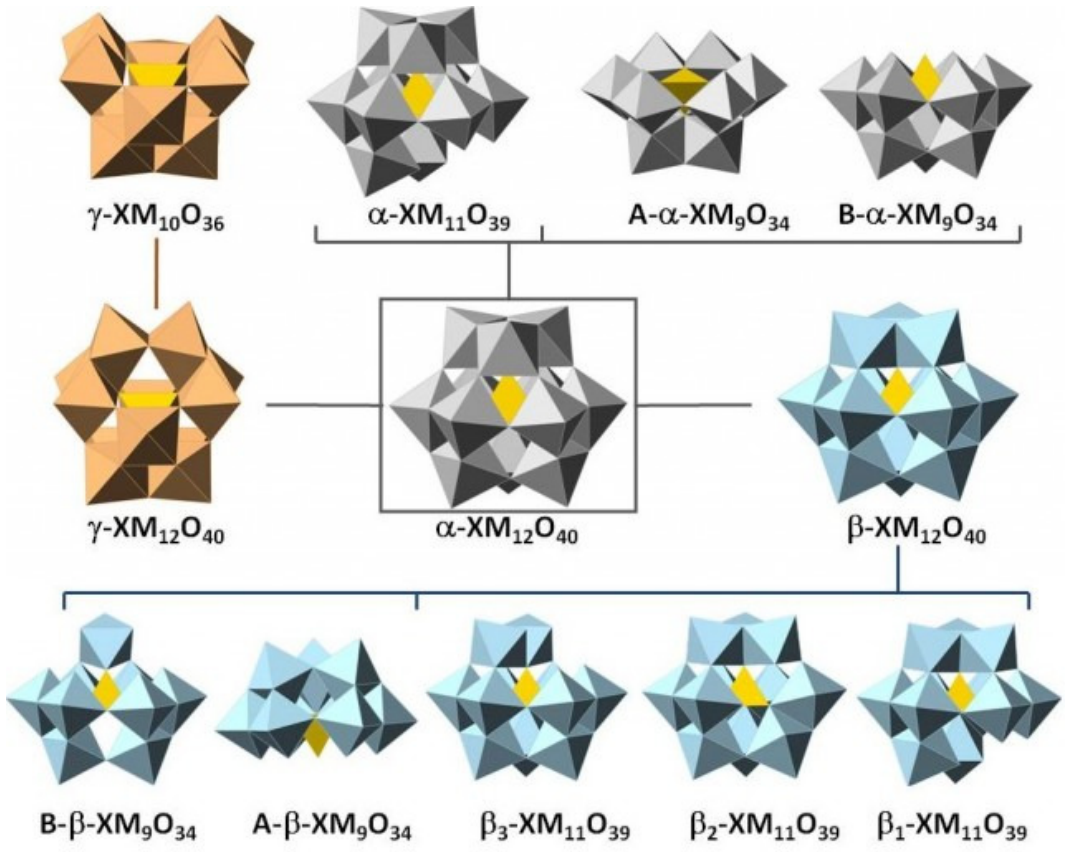

Figure 2.6 Lacunary species formed from Keggin-type heteropolyanion[1].

isomers having better stability as compared to the other rotational isomers. Figure 2.6 summarises the various known lacunary species of the three isomers. With an increase in pH, the most stable form of the Keggin structure heteropolyanion, α-$XM_{12}O_{40}$, loses adjacent MO_6 octahedra. The monovacant lacunary structure α-$XM_{11}O_{39}$ is generated with the loss of one octahedra[73], while the A-α-XM_9O_{34} is formed when three corner sharing octahedral M_3O_{15} is lost and B-α-XM_9O_{34} is formed when three edge sharing octahedral M_3O_{13} is lost[74]. Depending on the rotational isomer and the octahedral removed from the isomers, various lacunary species can be obtained.

The formation of lacunary species represents the opportunity to introduce various metal into the heteropolyanion structure. It also allows the formation of heteropolyanion based building blocks whereby the formation of the Dawson structure (Figure 2.1 (c)) which consists of 2 lacunary units of A-α-XM_9O_{34}. The presence of such lacunary structure in polyoxotungstates provide surfaces with tungsten bridging oxygen in a triangular array. This feature has a close resemblance to discrete fragments of metal oxide surface while makes heteropolytungstates attractive as mimics or discrete models of metal oxide supported heterogeneous catalysts[16]. In the attempts to prepare such experimental models, interesting dimerization reaction has been observed giving rise to “sandwich” structure as shown in Figure 2.7.

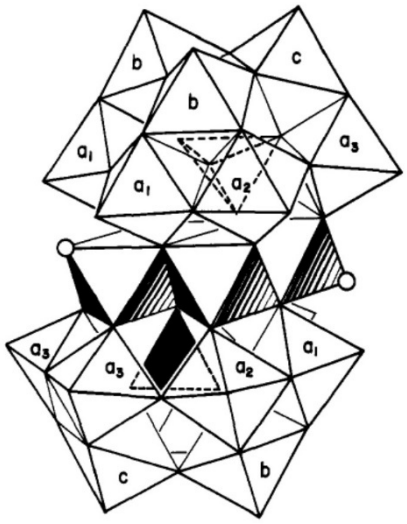

Figure 2.7 Polyhedra representation of a "sandwich-type" heteropolytungstate. The different types of tungsten atoms are labeled a_1, a_2, a_3, b and c. The mimicked M oxide surface occupies the four central edge linked polyhedra. Adapted with permission from Journal of the American Chemical Society[16].

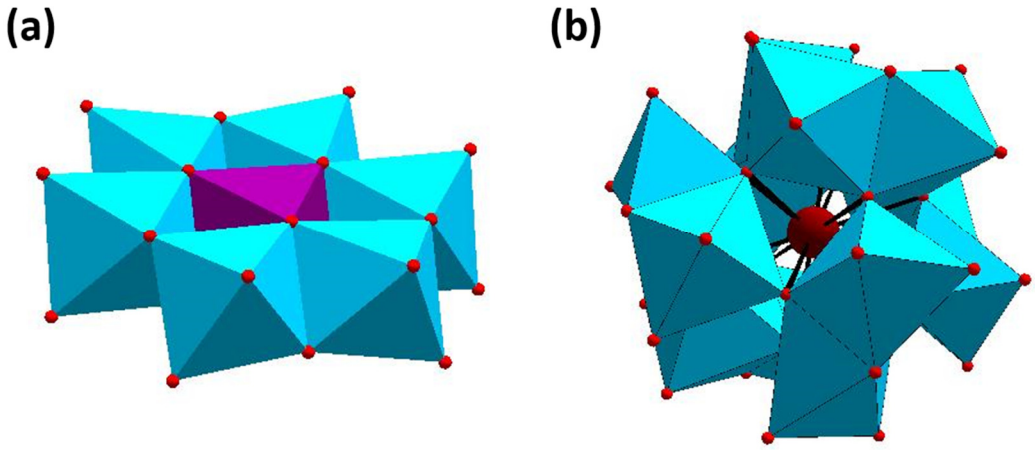

Figure 2.8 (a) Anderson-Evans structure and (b) Dexter-Silverton structure heteropolyanion.

The discussion of the Keggin and Dawson structures above are all based on the tetrahedron centre. The tetrahedron can be considered as one of the "parent" structure of highly symmetrical heteropolyanion. The central "parent" structures can be clearly distinguished as the tetrahedron, octahedron and icosahedron forming central polyhedron of XO_n (n = 4, 6, 12), where the symmetry of the whole heteropolyanion is determined. The structural type containing an octahedron as the central polyhedron is shown in Figure 2.8(a). The Anderson-Evans structure (e.g. $[Te^{6+}Mo_6O_{24})^{6-}$) is a type of 6-heteropolyanions with heteroatom in the octahedral pocket in the centre of a closed ring edge sharing MO_6 octahedra arranged in a coplanar manner[75]. The least common type of heteropolyanion are those with an icosahedron as the central polyhedron. The Dexter-Silverton structure[76] is a 12-heteropolyanion with a general formula of $[XM_{12}O_{42}]^{x-12}$. It common contains molybdenum as the addenda with cerium(IV), thorium(IV) or uranium(IV) as heteroatoms. The central polyhedron is an icosahedron surrounded by 12 MO_6 octahedra arranged in face-sharing pairs (Figure 2.8(b).

2.3. Properties of polyoxometalates

2.3.1. Crystal structure

Polyoxometalates or heteropoly-compounds generally form ionic crystals[77] which can accommodate large amount or water of crystallisation and counteraction within the large interstices formed due to the size of the heteropolyanion and the requirement due

to their ionic charge. The water of crystallisation forms the hydronium ion, $H_5O_2^+$, where the water molecules are held together by hydrogen bonding with a proton. The removal of the water is easy and reversible by simple increment of temperature up to 150°C. As mentioned earlier, water plays an important part in the crystal structure and packing of the heteropolyanion. Therefore, this influences the packing arrangement of the heteropolyanion as the water is lost or gained by the structure. A good example will be the different crystallographic space groups exhibited by 12-tungstophosphoric acid ($H_3PW_{12}O_{40}$). In the most highly hydrated state $H_3PW_{12}O_{40}\cdot 29H_2O$, the crystal structure has a cubic *Fd3m* space group[78]. A decrease in the water present in the structure to $H_3PW_{12}O_{40}\cdot 21H_2O$ lead to a structure with orthorhombic *Pcca* space group[79]. Further loss of water to $H_3PW_{12}O_{40}\cdot 14H_2O$ and $H_3PW_{12}O_{40}\cdot 6H_2O$ further transform the crystallographic structure to triclinic *P1*[80] and cubic *Pn3m*[81] respectively. Therefore, variation in the structure of polyoxometalates makes it difficult to obtain highly reproducible X-ray crystallographic information especially when powdered material is used instead of single crystal samples.

2.3.2. Solubility

The heteropolyanions has anionic charge delocalised over the large number of atoms present in the structure, resulting in very low lattice energies in the crystals related compound. The oxygen atoms on the exterior of heteropolyanions are strongly polarised towards the addenda, causing these non-basic oxygen unable to form hydrogen-bonds effectively[77]. This causes the heteropolyanions to be weakly solvated in solution and the solubility of heteropoly-compounds is largely dependent on the solvation energy of the counteraction. Heteropolyacid are highly soluble in polar solvents containing oxygen i.e. ethanol, diethyl ether etc. When countercations with small ionic radius i.e. Li^+ or Na^+ are used, the solubility is similar to the acidic form. This changes when larger countercations i.e. NH_4^+, K^+ or Cs^+ are used, making the resulting salt to be insoluble. The use of organic cations like alkylammonium or pyridinium[82] are effective for the isolation of heteropolyanions from aqueous solutions and for their application as catalyst in organic media.

2.3.3. Solution stability

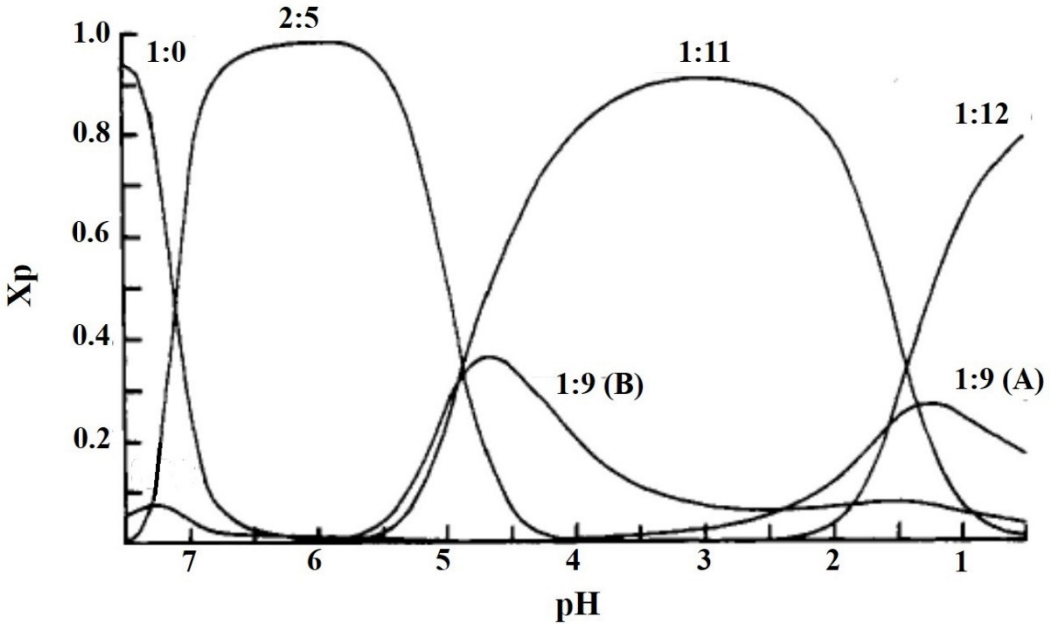

Figure 2.9 The distribution of 12:1 molar ratio of $[MoO_4]^{2-}$ and $[HPO_4]^{2-}$at different pH values. Adapted with permission from ref.[10]. Copyright 1986 American Chemical Society.

Heteropolyanions in solution are constantly in an equilibrium state as a function of solution pH. Figure 2.9 shows the distribution of an aqueous solution of phosphomolybdic acid ($H_3PMo_{12}O_{40}$) which contains 1:12 molar ratio of HPO_4^{2-} and MoO_4^{2-}. The pH of the solution during the isolation of the crystalline material is important since the abundance of the desired species will be affected at different pH ranges. However, even without deliberate pH control, studies have shown that typical Keggin heteropolyanion are able to retain their structure when concentration is relatively high[46]. On the contrary, when the concentration is too low ($<10^{-2}$ mol L^{-1}),

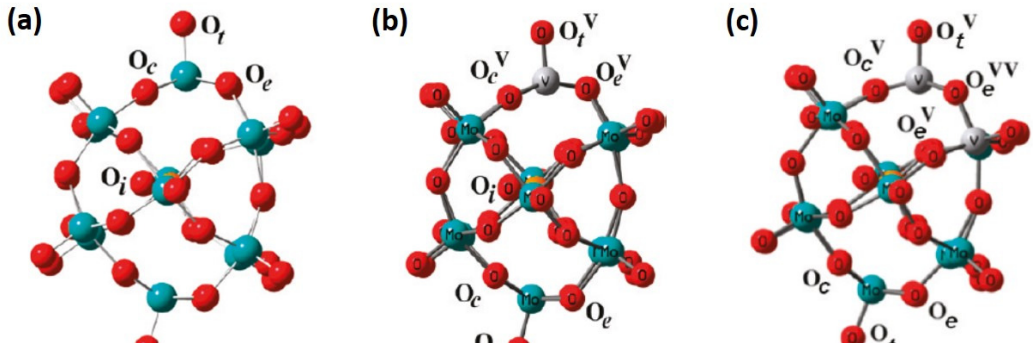

Figure 2.10 Ball and stick structure of mixed-addenda $[PV_nMo_{12-n}O_{40}]$ (a) n = 0, (b) n = 1 and (c) n = 2 Adapted with permission from ref [7]. Copyright 2011 American Chemical Society.

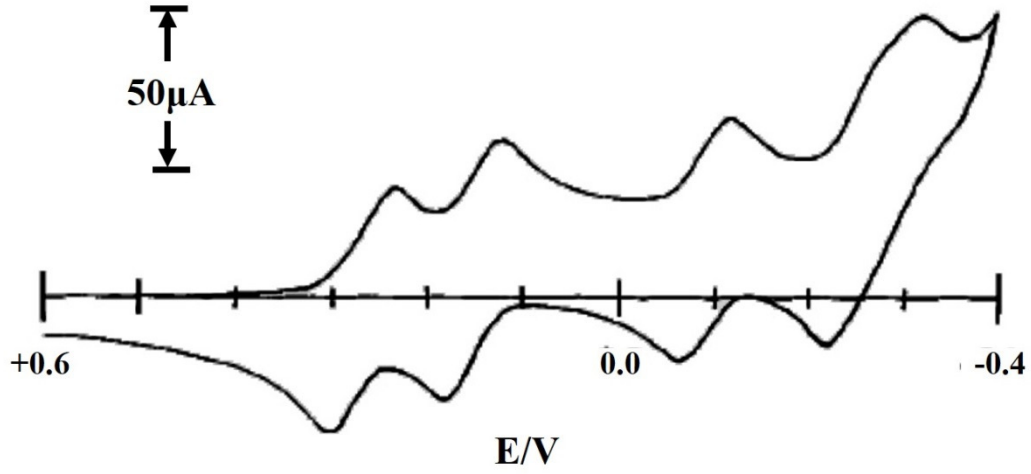

Figure 2.11 Cyclic Voltammogram of Keggin $[PMo_{12}O_{40}]^{3-}$ in 50% ethanol/water mixture containing 0.1 M HCl. Copyright 1991 Wiley. Used with permission from reference[12].

degradation of the heteropolyanion may occur. In order to circumvent the degradation of heteropolyanion in aqueous media, the use of organic medium should be considered as the stability of polyoxometalates/heteropolyanion increases in organic medium[46]. This allow for effective use of low concentration for synthesis or catalysis in organic media which will otherwise be difficult in aqueous media. Other strategies to improve the stability of heteropolyanion in solution includes the use of mixed-addenda heteropolyanion. Due to the improved solution stability of mixed-addenda heteropolyanion, the use of $[PV_nMo_{12-n}O_{40}]$ is chosen as the main focus in this dissertation. The structure of mixed addenda $[PV_nMo_{12-n}O_{40}]$ is shown in Figure 2.10. With the substitution of vanadium for molybdenum, the stability of the heteropolyanion is improved to a certain extent and improves the feasibility for practical application.

2.3.4. Redox Properties

The diverse redox chemistry of polyoxometalates/heteropolyanions is the subject of study, granting accessibility to their vast potential in chemical analysis[83,84] and catalysis[85-87]. The redox ability of polyoxometalates can be classified into two types according to Pope[12]. Type I is the mono-oxo type polyoxometalates, while type two is the cis-dioxo type. Mono-oxo types are best represented by the Keggin and Dawson structure and their derivatives where the addenda atoms have only 1 terminal oxygen

atom (M=O). In the cis-dioxo type, each addenda atom has two terminal oxygen arranged in cis-position, this type of polyoxometalates is best represented by the Dexter-Silverton structure.

In the mono-oxo type polyoxometalates, the MO_6 octahedra has a lowest unoccupied molecular orbital (LUMO) that is non-bonding metal centred orbital[88], this allows the mono-oxo type polyoxometalates to be easily reduced and oxidised reversibly forming mixed valence species. The reduced species are able to retain the anion structure and forms heteropoly-blues. In the cis-dioxo type polyoxometalates, the LUMO is anti-bonding with respect to the terminal metal oxygen bond (M=O), this leads to resistant towards reduction with low reversibility of the formed complexes[12]. Therefore, Keggin type polyoxometalates which are of the mono-oxo type are more useful for oxidation catalysis.

Since polyoxometalates contain transition metals which are fully oxidised (d^0), this makes them resistant to oxidation, granting redox stability. By virtue of the highly oxidised state of polyoxometalates, type I polyoxometalates are able to accept many electrons. The increase in the negative charge of the anion is stabilised by protonation provided from the solvent while the anion structure is preserved throughout. This has been shown by electrochemical studies in Figure 2.11, where Keggin-type heteropoly-molybdate of $[PMo_{12}O_{40}]^{3-}$ shows a series of reversible one/two electron redox reaction[12]. The reduction of the heteropolyanion can be clearly observed by the intense blue colour with increasing number of electrons gained, thereby the name heteropoly-blue. The electronic spectra of heteropoly-blues show strong d-d bands in the visible region. The oxidising potential of polyoxometalates is strongly dependent on their addenda atom. Therefore, by making use of mixed-addenda heteropolyanion, it is possible to influence the redox potential to cater to required applications.

The Keggin type polyoxometalates $[PV_nMo_{12-n}O_{40}]^{(3+n)-}$ used for studies in this dissertation has been studied in much detail for its redox properties[7,89]. It has application in catalytic oxidation application[90-92] due to their fairly high oxidation potential[46] and ease of re-oxidation by oxygen[93]. The reaction representative of the reduction and oxidation processes are as follow:

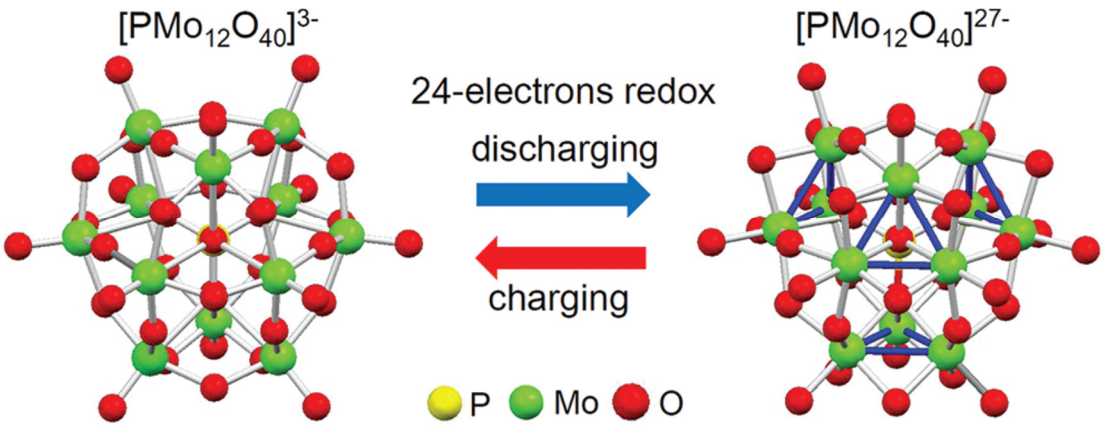

Figure 2.12 Keggin polyoxometalate, $PMo_{12}O_{40}^{3-}$ undergoing 24 electrons redox process, acting as an "electron-sponge". Reprinted with permission from reference[14]. Copyright 2012 American Chemical Society.

$$[PV_nMo_{12-n}O_{40}]^{(3+n)-} + x\,H^+ + Red \rightarrow H_x[PV_nMo_{12-n}O_{40}] + Ox \qquad \text{Eqn (2.3)}$$

$$H_x[PV_nMo_{12-n}O_{40}] + \frac{x}{4}O_2 \rightarrow [PV_nMo_{12-n}O_{40}]^{(3+n)-} + \frac{m}{2}H_2O \qquad \text{Eqn (2.4)}$$

Where Red is the reducing agent, Ox is its oxidised form. The oxidation by oxygen in solution does not proceed in the case of single addenda $PMo_{12}O_{40}^{3-}$, therefore mixed addenda polyoxometalates are preferred in use as oxidation catalysts.

To add on to the redox capabilities of Keggin type polyoxometalates, their ability to be reduced without impairment of the anion structure allows a single addenda Keggin polyoxometalates to accept up to 24 electrons[94] forming a super-reduced state. This allows them to be used as “electron sponge”[14], where the molecular structure of the anion reduces in size in order to form Mo^{4+} metal-metal bonded triangles (Figure 2.12) in order to accommodate the super-reduced state. The incorporation of $PMo_{12}O_{40}^{3-}$ into lithium ion batteries (LIBs), forming what Wang et. al.[14] termed as the molecular-cluster batteries is expected to provide high capacity, rapid discharging/charging multi-electron redox reaction by polyoxometalates and expedite lithium ion diffusion. Alternatively, their use as secondary charge storage sites in anode material is also feasible[11]. Therefore, a minor part of this dissertation will explore synthetic strategy of polyoxometalates immobilization and their redox properties in LIBs.

2.4. Catalysis by polyoxometalates

Heterogeneous catalysis by polyoxometalates can be divided into three types, namely surface, bulk type I and bulk type II[70] as shown in Figure 2.13. Surface type catalysis refers to typical heterogeneous catalysis which takes place on the surface of the catalyst. The kinetics of such catalysis is largely affected by the surface area of the catalyst. In bulk type I catalysis, the heteropolyanion acts as a pseudoliquid phase, adsorbing the reactants for the reaction to take place. Lastly, bulk type II catalysis principally occur on the surface of the catalyst, however the rapid migration of redox carriers facilitates the bulk solid to take part in the redox catalysis.

The advantages of heteropolyanions as catalyst is summarized by Okuhara et. al. as shown in Table 1[2]. Since the use of polyoxometalates provide the opportunity for catalyst design at atomic and molecular level, it is possible to find many practical applications for them. However, when considering the viability for environmental application in aqueous system, the heterogenization of polyoxometalates is the fundamental objective required to be achieved. This can proceed by the primary strategy of molecular design from the incorporation of ligands for functionalisation[26] , architectural design by immobilization on solid supports[48] or use of ligands or counter-cations to form interesting nano-architectures[4]. Various strategies for preparation of polyoxometalates as heterogeneous catalyst are shown in Figure 2.14. Immobilizing catalytically active polyoxometalates onto solid supports is an efficient and facile strategy to heterogenise polyoxometalates for catalytic applications.

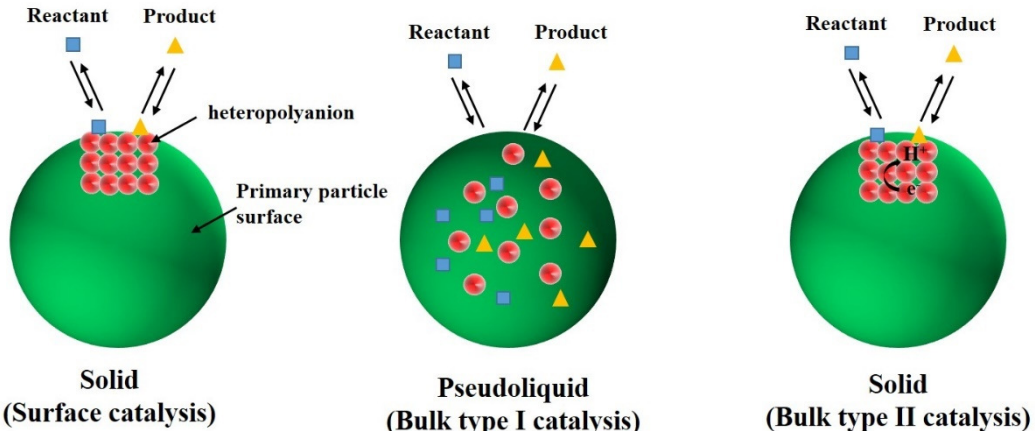

Figure 2.13 Three types of heterogeneous catalysis by heteropolyanions.

Table 2.1 Advantages of heteropolyanion catalysts. Reprinted from reference[2]. Copyright 1996, with permission from Elsevier (Academic Press, Inc.)

1. Catalyst design at atomic/molecular levels based on the following:
• Acidic and redox properties These two important properties for catalysis can be controlled by choosing appropriate constituent elements, i.e. • type of polyanion • addenda atom • heteroatom • counteranion, etc
• Multifunctionality Acid-redox, acid-base, multi-electron transfer, photosensitivity, etc.
• Tertiary structure, bulk-type behaviour
2. Molecularity-metal oxide cluster
• Molecular design of catalysts
• Cluster models of mixed oxide catalyst and of relationships between solid and solution catalysts
• Description of catalytic processes at atomic/molecular levels Spectroscopic studies and stoichiometry are realistic Model compounds of reaction intermediates
3. Unique reaction field
• Bulk-type catalysis "Pseudoliquid" and bulk type II behaviour provide unique three dimensional reaction environment for catalysis.
• Pseudoliquid behaviour Spectroscopic and stoichiometric studies are feasible and realistic
• Phase-transfer catalysis
• Shape selectivity
4. Unique basicity of polyanion
• Selective coordination and stabilization of reaction intermediates in solution and in pseudoliquid phase
• Ligands and supports for metals and organometallics

2.4.1. Immobilized polyoxometalates and their applications

The immobilization of polyoxometalates on solid supports can be effectively categorised into two groups: (1) polyoxometalate is supported on catalytically inactive materials and (2) polyoxometalate is supported on catalytically active material. The support material chosen are typically porous materials and preferably be nano-sized particles. The fulfilment of the two criteria would provide a platform for uniform distribution of active sites thereby decreasing the mass transfer resistance. It is therefore imperative to select suitable supports in order to design effective and efficient polyoxometalates base heterogeneous catalysts. Table 2 summaries typical supports used for polyoxometalates heterogenization and their applications. From the selected examples of polyoxometalates immobilized materials shown in table 2, the use of polyoxometalates in oxidative catalysis, adsorption, pollutant degradation is relatively well established. The preparation multifunctional polyoxometalates by design with suitable solid support and diverse chemical properties of polyoxometalates therefore enable their application as solution for various environmental problems. Controlling of the polyoxometalates composition from the atomic and molecular level also bestow researchers the ability to design environmentally benign materials and ensure sustainability.

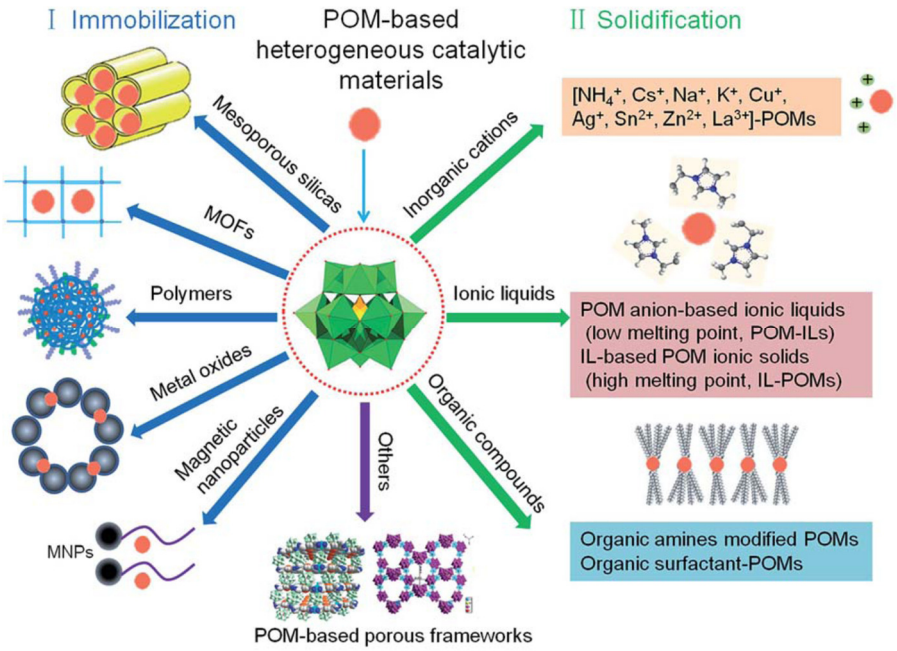

Figure 2.14 The key strategies for preparation of heterogeneous polyoxometalates-based catalyst. Reproduced from reference[5] with permission of The Royal Society of Chemistry.

Table 2.2 Polyoxometalates immobilized materials and their applications.

Supports	Polyoxometalates used	Methodology for immobilization	Application	Ref.
Mesoporous silica				
SiO_2	$[C_nmim]_3PW_{12}O_{40}$	One pot hydrothermal impregnation	Oxidative desulfurization	95
SBA-15	$H_5PV_2Mo_{10}O_{40}$	Electrostatic interaction	Selective propene oxidation	96
Core-shell structured SiO_2	$H_3PMo_{12}O_{40}$	Electrostatic interaction	Safranine T dye degradation	97
Amorphous silica	$((n\text{-}C_4H_9)_4N)_4[PW_{11}FeO_{39}]$	Hydrogel impregnation	Alcohol oxidation with H_2O_2	98
SiO_2 encapsulated γ-Fe_2O_3	$[PW_{12}O_{40}]^{3-}$, $[SiW_{12}O_{40}]^{4-}$ and $[PMo_{12}O_{40}]^{3-}$	Impregnation method	Oxidative esterification	99
Nano silica ball	$H_{(3+n)}PV_nMo_{(12-n)}O_{40}$	Impregnation method	Methylene blue degradation with H_2O_2	100
SiO_2	$H_3PW_{12}O_{40}$ / $H_4SiW_{12}O_{40}$	One-pot synthesis	Photocatalytic degradation of organochlorine pesticides	101
Anionic exchange resin				
D301R	$Na_5PW_{11}O_{39}Mn(H_2O)$	Ion-exchange	Rhodamine B dye degradation	102
D201	$Na_3PW_{12}O_{40}$, $Na_4SiW_{12}O_{40}$	Ion-exchange	Photocatalytic degradation of dyes	103
MOFs				
HKUST-1	$H_3PW_{12}O_{40}$	One-pot synthesis	Selective heavy metal adsorption	104
HKUST-1	$H_3PMo_{12}O_{40}$, $H_4PVMo_{11}O_{40}$, $H_5PV_2Mo_{10}O_{40}$, $H_6PV_3Mo_9O_{40}$	One pot synthesis	Selective oxidation of alcohol	105
MIL-101	$K_4PW_{11}VO_{40}$, $H_3PW_{12}O_{40}$, $K_4SiW_{12}O_{40}$	One-pot solvothermal synthesis	Selective adsorption of cationic dyes	106
MIL-101 (Cr)	$Na_{10}[Co_4(H_2O)_2(PW_9O_{34})_2]$	Ion-exchange method, via electrostatic interaction	Water oxidation catalyst	107

Table 2.3 Polyoxometalates immobilized materials and their applications. (cont'd)

Supports	Polyoxometalates used	Methodology for immobilization	Application	Ref.
MOF				
Phosphorescent MOF built from $[Ir(ppy)_2(bpy)]^+$and $[Ru(bpy)_3]^{2+}$-derived dicarboxylate ligands	$[Ni_4(H_2O)_2(PW_9O_{34})_2]^{10-}$	One-pot in-situ assembly	Visible-light hydrogen evolution reaction	108
MOF-5	$H_6P_2W_{18}O_{62}$	One-pot solvothermal synthesis	Selective adsorption of cationic dye	109
MIL-101(Fe)	$H_3PW_{12}O_{40}$	One-pot solvothermal synthesis	Cationic dye removal	110
Polymers				
D380 macroporous benzylamine	$((NBu_4)_6[\alpha_2\text{-}P_2W_{17}O_{61}(SiC_6H_4CH_2N_3)_2O])$	Covalent immobilization	Tetrahydrothiophene oxidation	111
Azo-Tr/TeEG@CD	$PW_{11}VO_{40}{}^{4-}$	Electrostatic interaction with polyoxometalates as connection nodes between monomers	Filtration of small organic molecules	112
PVDF membrane	$((C_{18}H_{37})_2(CH_3)_2N)_5(PV_2Mo_{10}O_{40})$	Direct incorporation *via* phase inversion technique	Reactive black 5 dye removal	113
Metal Oxides				
TiO_2	$H_3PW_{12}O_{40}$, $H_4SiW_{12}O_{40}$	Sol-gel method	Photocatalytic degradation of malachite green	114
3-aminopropyl functionalized TiO_2	$[Ru^{IV}{}_4(OH)_2(H_2O)_4(\gamma\text{-}PW_{10}O_{36})_2]^{9-}$	Electrostatic interaction	Light-induced water oxidation	115
Tris-LDH-CO_3	$Na_3PW_{12}O_{40}$, $K_6P_2W_{18}O_{62}$, $Na_9La_{W=10}O_{36}$	Anion-exchange method	Dye degradation	116

2.4.2. Titanium dioxide-supported polyoxometalates

The immobilization of polyoxometalates on titanium dioxide is of particular interest as this represents a combination of two materials, both with semiconductor-like properties[33]. Titanium dioxide has been extensively studied as a photocatalyst as it has relatively high chemical stability, is non-toxic, low-cost and easily available. The combination of titanium dioxide with polyoxometalates is therefore able to provide a material design which is environmentally friendly. Yang et. al.[18] prepared a nanoporous anatase and $H_3PW_{12}O_{40}$ composite.by a sol-gel hydrothermal method, which directly embed the polyoxometalates within the anatase lattice forming particles less than 10 nm in size (Figure 2.15(a)). The formation of the nanocomposite resulted in a red-shift from the anatase support as shown in Figure 2.15(b). It was found that the nanocomposite was able to degrade a variety of dye under visible light irradiation. However, the presence of $H_3PW_{12}O_{40}$ within the anatase structure was not obvious other than the influence on light adsorption of the material. The presence of the polyoxometalates was not detectable from powder X-ray diffraction analysis perhaps due to the embedding of the polyoxometalates

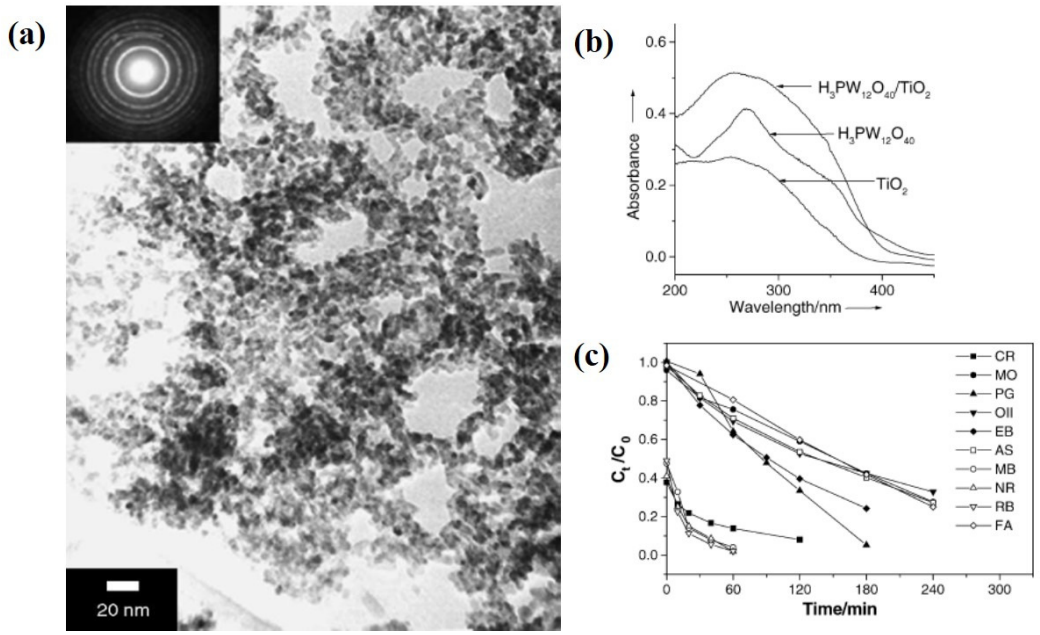

Figure 2.15 (a) TEM image and SAED pattern of $H_3PW_{12}O_{40}/TiO_2$nanocomposite, (b) UV-vis diffuse reflectance spectra of TiO_2, $H_3PW_{12}O_{40}$ and $H_3PW_{12}O_{40}/TiO_2$ composite. Visible photocatalytic degradation of various dyes using the nanocomposite. Reprinted from reference[18]. Copyright 2005. With permission from Elsevier.

within the anatase which does not allow the formation of polyoxometalates crystalline phase for detection.

Xie[6] prepared a $H_3PW_{12}O_{40}$ titania nanotubular array composite for photocatalysis and photoelectrocatalysis of an endocrine disruptor bisphenol A. The nanotubular array was prepare by a low voltage anodization process (Figure 2.16(a) and (b)), $H_3PW_{12}O_{40}$ was embedded into the nanotubular array (Figure 2.16 (c) and (d)). The composite was able to completely degrade BPA under UV-light illumination. Comparing this with the studies performed by Yang et. al.[18] above, the immobilization of $H_3PW_{12}O_{40}$ does not seem to achieve similar synergistic effect by the formation of composite. In addition, the embedding of $H_3PW_{12}O_{40}$ may not provide good interaction between the titania nanotubular array and the polyoxometalates. The solution is constantly purged by oxygen airflow and the resultant solution shows considerable leaching of $H_3PW_{12}O_{40}$ in the UV-

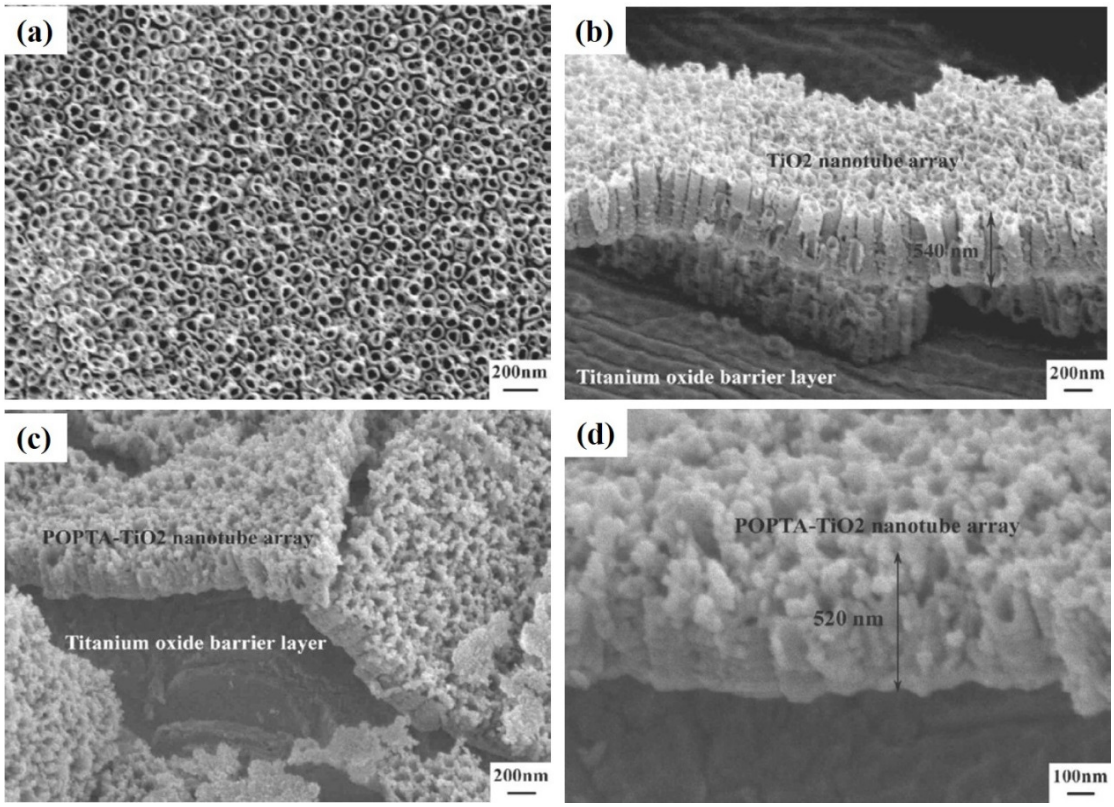

Figure 2.16 FESEM images of (a) TiO_2 nanotubular array, and cross-sectional SEM images of (b) TiO_2 tubules, (c) $PW_{12}O_{40}$-TiO_2 tubules, and (d) enlarged view of $PW_{12}O_{40}$-TiO_2 tubules. Reproduced from reference[6].

vis spectra. The need for supply of an external electrical potential in addition to the use of UV as a light source also reduces the viability of such process for practical usage.

A three-dimensionally ordered macroporous (3DOM) titanium dioxide based catalyst was amine-functionalized for the immobilization of $K_5[PW_{11}Co(H_2O)O_{39}]$ by Lu et. al.[17]. The strategy employed provided a novel and efficient pathway to preparation of a three dimensional architecture for the immobilization of the polyoxometalates. Polystyrene spheres were synthesized and used as a template for the formation of three-dimensional titanium dioxide structure (Figure 2.17 (a-c)). The material was annealed to remove the template and amine-functionalized with (3-aminopropyl)triethoxysilane. The immobilization of $K_5[PW_{11}Co(H_2O)O_{39}]$ was achieve by dative bonding of the amine function group with the cobalt on the polyoxometalates (Figure 2.17 (d-f)). The authors of

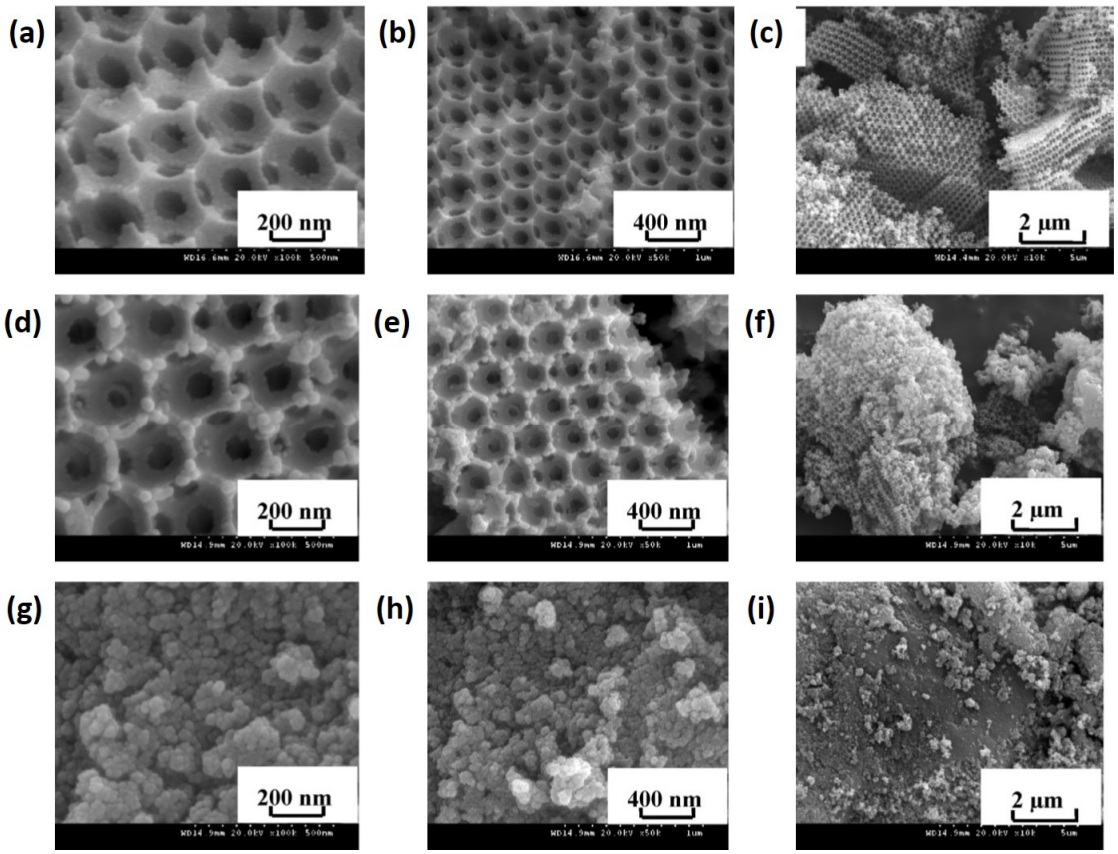

Figure 2.17 SEM images of (a-c) 3DOM-TiO_2, (d-f) 3DOM $PW_{11}Co$-APS-TiO_2 and (g-i) $PW_{11}Co$-APS-TiO_2. Reprinted from reference[17]. Copyright 2014. With permission from Elsevier.

this work also prepared the same material without the use of polystyrene template, which resulted in material with no distinct morphology as shown in Figure 2.17 (g-i)).

The catalyst prepared could effectively degrade organic dye under a combination of UV light and microwave irradiation. The three-dimensional structure is one of the main strengths of the catalyst which allowed efficient mass transport of pollutant to catalyst surface. While the material presents a structural edge for catalytic application, the preparation might not be facile or robust due to problem with incomplete filling of the template. On the other hand, use of UV irradiation and microwave are relatively energy consuming process. It is thus important to weigh the advantage of energy consumption against the effectiveness of the catalytic efficiency of the material. The role of $K_5[PW_{11}Co(H_2O)O_{39}]$ in the prepared material was a mediator to retard the electron-hole pair recombination and does not effectively utilize the catalytic capability of the polyoxometalates.

From the review of the few studies of titanium dioxide material immobilized with polyoxometalates as heterogeneous catalyst, the role of polyoxometalates in catalysis is obscured by the catalytic activity of titanium dioxide. It is therefore of research interest to look into the catalytic and redox activity of polyoxometalates for environmental application for better understanding of their role in catalysis. The effective design of polyoxometalates immobilized catalyst could incorporate the formation of “bulk” heteropolyacid phases which should enhance the bulk type II catalytic capability of polyoxometalates on solid support. Even though one pot type synthesis is desirable from the synthetic point of view, it would be unlikely to achieve the formation of crystalline acid phase of heteropolyacids under such conditions. While direct embedding of polyoxometalates could lead to loss of catalytic sites during application. Optimal conditions for the preparation of such supported catalyst should then involve the use of coupling agent which can stabilize and improve the growth and formation of polyoxometalates on the support surface.

2.4.3. Polyoxometalates supported on other materials

While Table 2 and section 2.4.2. summarizes the various supports used for the immobilization of polyoxometalates and the design parameters to be taken into consideration when preparing polyoxometalates immobilized on titanium dioxide, other carbon based materials have also been used for immobilization. This section will thus provide a brief look into these materials, which includes carbon nanotubes (CNTs)[117,118], graphene oxide (GO)[8] and carbon nitride[119]. The strategies for immobilization of polyoxometalates on these supports are analogous as these materials all contains honeycomb 6-membered aromatic networks. This is as depicted in Figure 2.18 with graphene as an example. Their high surface area, presence of functional groups for modification and electronic properties makes them highly attractive substrates for solid support.

Immobilization of polyoxometalates on carbon based material like CNTs or GO are generally targeted at energy applications. Polyoxometalates can be used as components for environmentally friendly rechargeable LIBs[120,121], which can be safe and non-toxic with careful selection of polyoxometalates used. However, even with the immobilization of polyoxometalates on conducting polymers, polymer support degradation led to detrimental

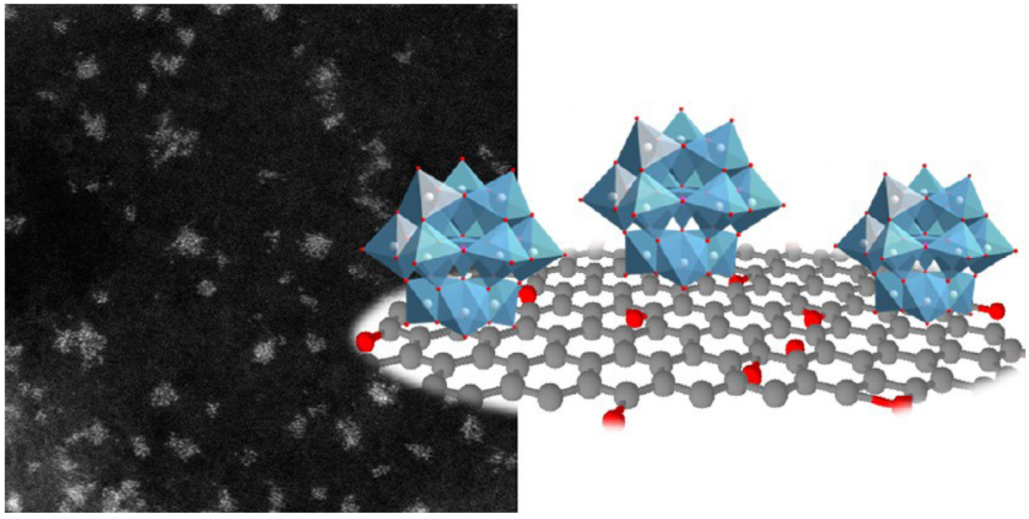

Figure 2.18 Polyoxometalates immobilized on functionalized graphene sheet. Reprinted with permission from reference[8]. Copyright 2013 American Chemical Society.

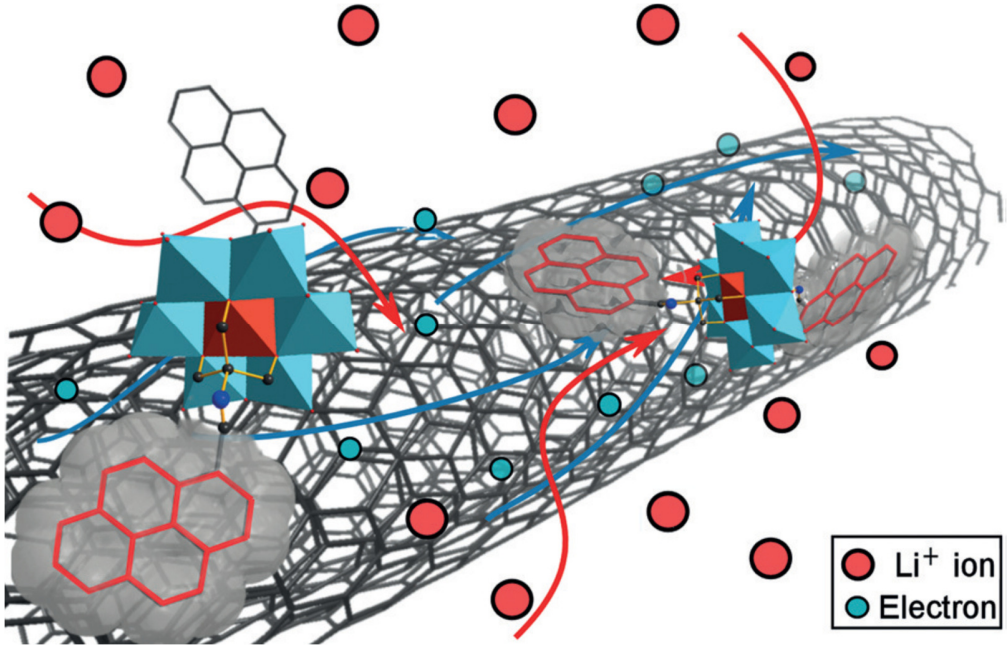

Figure 2.20 Schematic representation of CNT modified with Py-Anderson clusters via noncovalent functionalization. Reprinted from reference[11]. Copyright 2015 With permission from John Wiley and Sons.

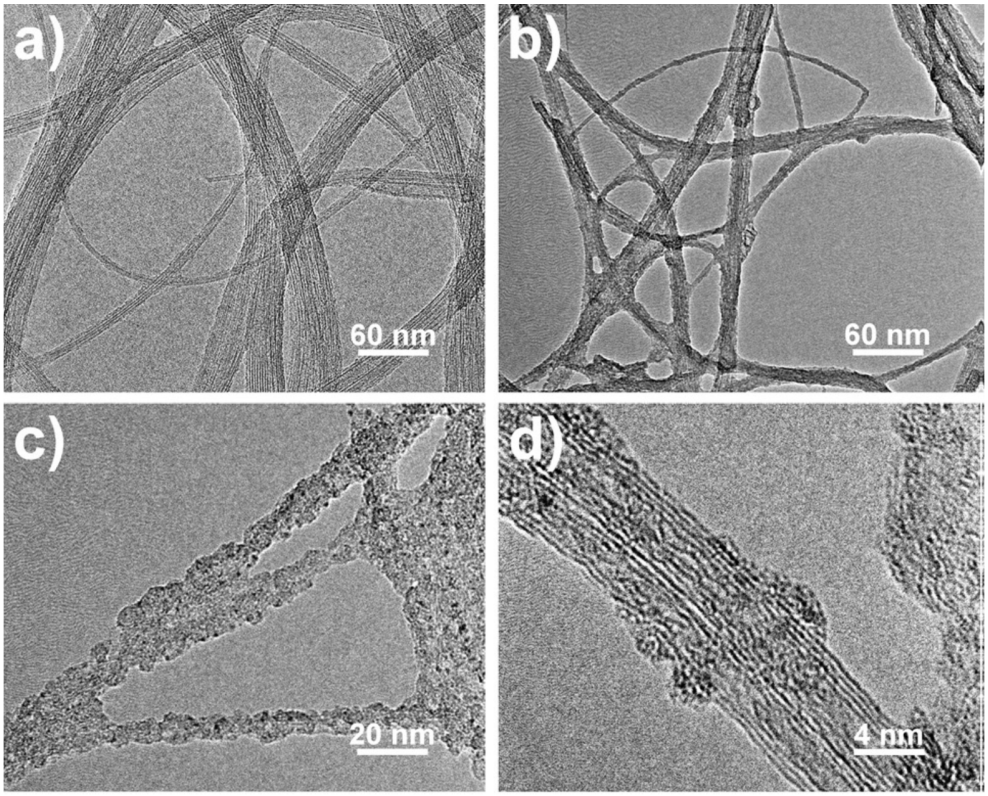

Figure 2.19 TEM micrograph of (a) pristine CNTs, (b-d) Py-Anderson-CNTs nano composite. Reprinted from reference[11]. Copyright 2015 With permission from John Wiley and Sons.

effects on charge-discharge cycling[122-124]. This cycling process also lead to the solubilisation of polyoxometalates[120] which led to charge loss in the fabricated devices.

Figure 2.19 shows the schematic representation of a polyoxometalates immobilized CNT by Huang et. al.[11]. Instead of using electrostatic or covalent immobilization, the immobilization was achieved by first functionalizing the Anderson-type polyoxometalates with pyrene, forming Py-Anderson poyloxometalates. This enables the formation of π- π interaction between the pyrene group and the surface of the CNTs which has a debundling effect on the CNTs. The unmodified CNTs in Figure 2.20(a) has regular and even features while the modified surface with Py-Anderson polyoxometalates are highly uneven, showing the effectiveness of the methodology in the modification of CNT surface. The combination of the two materials provided electrochemical enhancement of the nanocomposite acting as an anode material for LIBs.

He et. al. prepared $H_3PW_{12}O_{40}$ and $H_3PMo_{12}O_{40}$ supported on g-C_3N_4 as a hybrid photocatalyst for degradation of methylene blue and phenol. The immobilization was

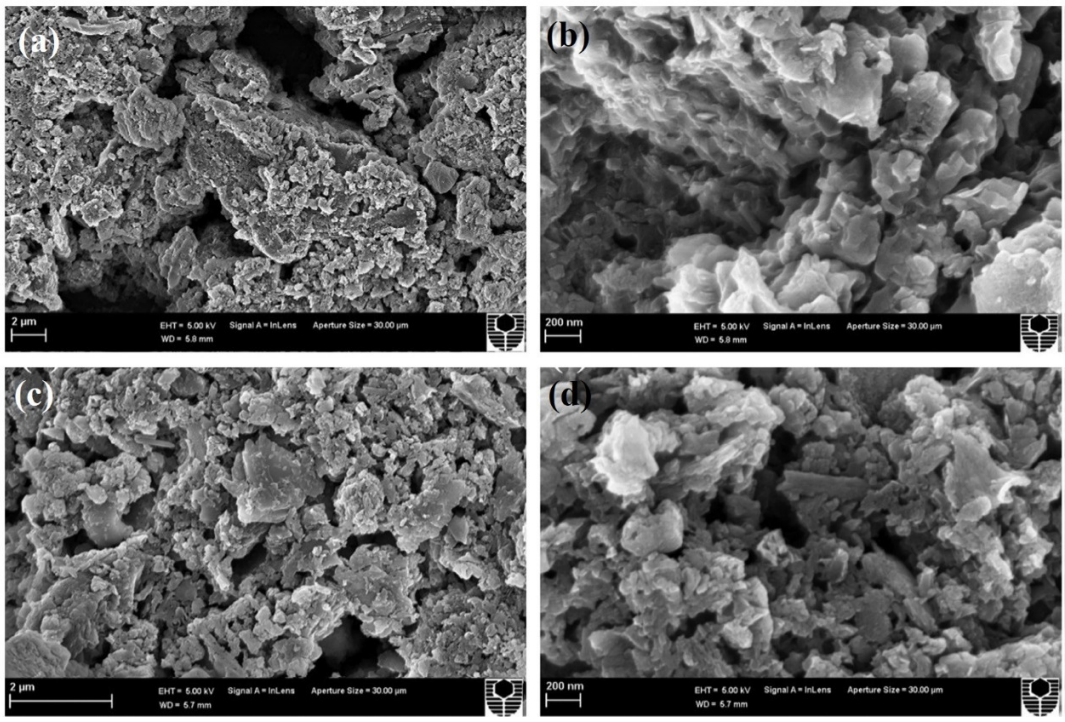

Figure 2.21 SEM micrograph of C_3N_4 modified with (a,b) $PMo_{12}O_{40}$ and (c,d) $PW_{12}O_{40}$. Adapted from reference[9]. Copyright 2015. With permission from Elsevier.

achieved by a one pot hydrothermal synthesis of g-C_3N_4 and polyoxometalates at different loading. The studies indicate that at 6% loading, the material has highest surface area and pore volume which contributed the better photocatalytic performance. The SEM images of the polyoxometalates modified g-C_3N_4 (Figure 2.21) shows that the material prepared has no defined morphology probably due to the poor dispersion of g-C_3N_4 which is difficult to control during the hydrothermal synthesis. However, X-ray diffraction analysis shows the presence of the crystalline planes in the prepared material which may account for the effectiveness of the material for photocatalytic applications.

2.4.4. Polyoxometalates prepared by solidification with counter-cations

The selective use of counter-cations is another strategy for obtaining polyoxometalates-based heterogeneous catalyst. As mentioned in section 2.3.2., the use of cations with large ionic radius, i.e. K^+, Cs^+ or NH_4^+ etc. leads to the formation of insoluble polyoxometalates for use as heterogeneous catalyst. The use of Cs^+ and NH_4^+ as counter-cations are the most extensively studied as these polyoxometalates exhibit tunable micro/mesoporous structures with exceptional BET specific surface area[125]. The use of inorganic cations can be rather limited as compared to the use of organic cations. Organic cations have the versatility of adjustment of the organic functional groups which allow further

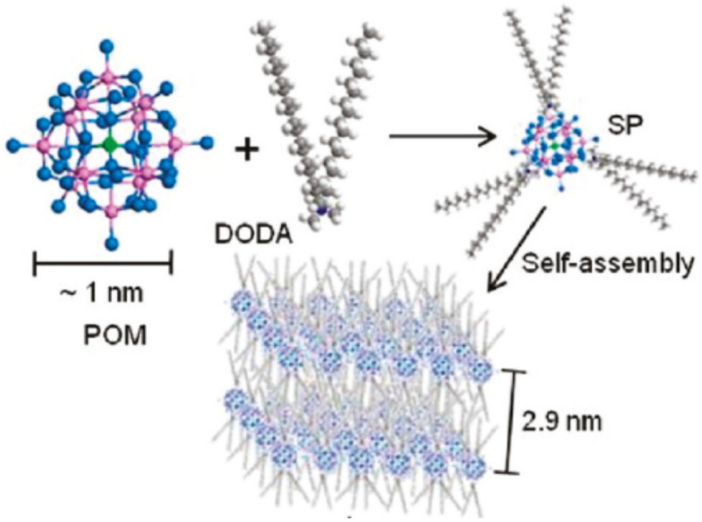

Figure 2.22 Micellar self-assembly of polyoxometalates with dimethyldiocatadecylammonium bromide. Adapted with permission from reference[4]. Copyright 2010 American Chemical Society.

functionalization during the modification with poyloxmetalates anions. Typical organic compounds used in this area are the organic amines, organic surfactants and ionic liquid cations[5]. Of particular interest to us was an organic-inorganic hybrid which was formed by combination of surfactant and POMs, which was used in the preparation of amphiphilic building blocks (Figure 2.22). Studies have been conducted to obtain novel architecture of such organic-inorganic hybrid systems with the aim of functionalizing polyoxometalates for catalytic applications in various media[4]. The development in this aspect is lacking and poorly defined. Some of recent developments of these nano-architectures will be reviewed below.

Pioneering work in this area was done by Mingotaud et. al.[126], where the Keggin anion was reacted with an alkylammonium surfactant, dimethyldioctadecylammonium bromide, in a ligand exchange reaction, prepared as a Langmuir-Blodgett film (LB-film). Many other works that followed adopted a similar concept; an example was report by Wu. et. al.[127], where self-assembled monolayers of surfactant encapsulated polyoxometalates (SEP) formed nano-patterns driven by the self-optimization of surface energy by the

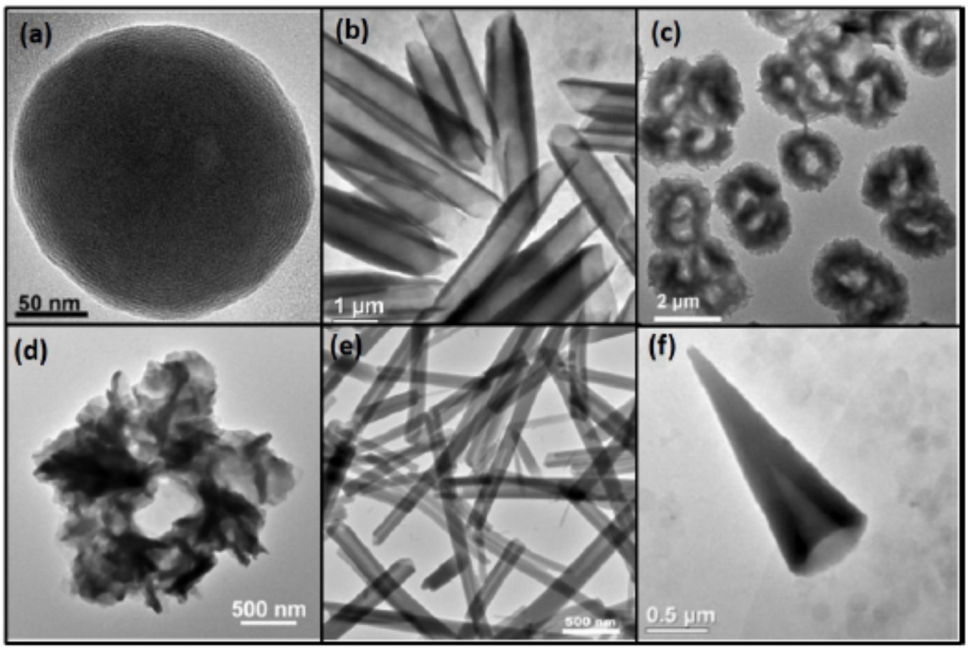

Figure 2.23 SEP assemblies. (a) Fullerene, (b) tubes, (c) rose flows, (d) snow flowers, (e) semi-tubes and (f) cones.

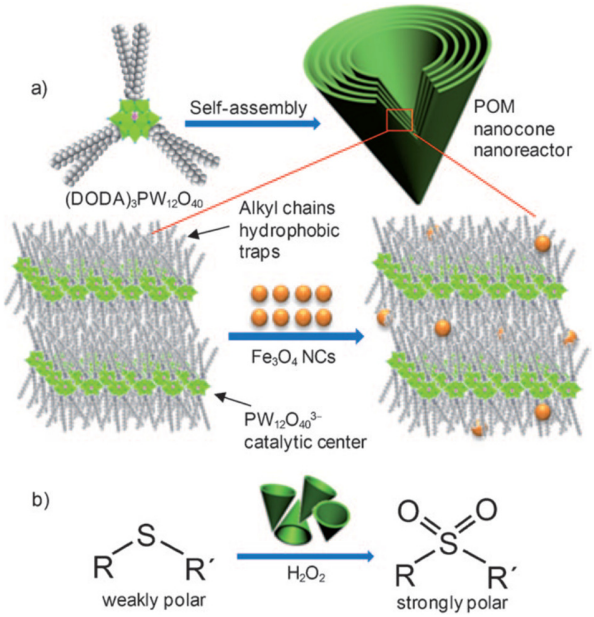

Figure 2.24 (a) Assembly of nanocones from $(DODA)_3PW_{12}O_{40}$ with incorporation magnetite nanocrystal. (b) Oxidation of sulfides using the nanocones as a nanoreactor. Reprinted from reference[13]. Copyright 2011 With permission from John Wiley and Sons.

monolayers. In the domain of formation of SEP nanoparticles, the formations of some unique shape are certainly intriguing. The formation of such lamellar structure giving rise to onion-like appearance in the nanometre domain (Figure 2.23(a))[128] was followed by several other uniquely-shaped hybrid materials prepared by the variation of solution composition. The images of other types of architecture are shown in Figure 2.23, depicting SEPs forming tubular rose flowers, snow-flowers, semi-tubes and cones[129]

Nisar et. al. reported the formation of such a hybrid, with controlled reversibility between nanocones and nanotubes structure achieved by the variation in solvent composition of chloroform and n-butanol[130]. Further development was also achieved by the incorporation of magnetite nanocrystals into these nano-assemblies. They were then used catalytically in the oxidation of dibenzothiophene, diphenyl sulphide and dimethyl sulphide[13]. Such assemblies allow the effective implementation of heterogeneous catalysis and an improved recoverability of the catalyst by the simple use of a magnet (Figure 2.24).

2.5. Brief introduction to advanced oxidation processes

The increasing footprint of recalcitrant organic pollutants in the environment, has made it more difficult to remove them using conventional methods[131] This has led an increasing focus on the development of advanced oxidation processes as an effort to degrade these toxic chemicals. Advanced oxidation processes generate highly reactive radicals in sufficient quantities, where they are capable of oxidizing majority of complex chemical matrix present in effluent water[132,133]. Example of such processes includes Fenton chemistry[134,135], which utilizes the activation of hydrogen peroxide with the aid of iron salts; cavitation, which is generated by irradiation of ultrasonic energy or by means of mechanical constrictions[136]; photocatalytic oxidation, which makes use of semiconductor catalysts working under UV or visible light[137-139] and catalytic wet air oxidation using high temperature and pressure with air as the oxidant[132,140].

The abovementioned methods typically make use of the formation of hydroxyl radicals which has an oxidizing potential of 2.33 V. The reaction kinetics exhibited by hydroxyl radicals are faster than typical chemical oxidant and is unselective over both organic and inorganic pollutants. The added advantage is that some of these methods also reduce the application of additional chemicals, which allows for lower waste generation and greater sustainability in the long run. Herein, a short review of the 2 methods: photocatalytic oxidation and catalytic wet air oxidation will be highlighted in general.

It is known that POMs have been used extensively in the areas of catalysis. The most well-known Keggin POMs like silicotungstic acid, phosphotungstic acid and phosphomolybdic acid are commercialized products which can be easily obtained from chemical suppliers. This is substantial evidence that polyoxometalates has great potential for development as catalyst with improved functionality as exemplified with the nanocone reactors in the previous section. Therefore, the application of polyoxometalates in catalysis for environmental remediation should be given more emphasis as it is an environmentally benign catalyst[33,141].

2.5.1. Introduction to photocatalytic oxidation

Photocatalysis is a process which makes use of light to achieve a catalytic reaction. For applications in environmental remediation, photocatalytic oxidation[43] would be the area of key interest. In order to achieve green and sustainable chemistry with practical application, the use of light as a component in reactions is especially attractive since it is virtually chemical free process which is atom economic. The greater enthrallment of photocatalysis would be the employment of light energy in the spectrum of visible light, which makes up most of the Sun's radiation reaching the Earth's surface. This would give the process a great edge over others due to improved self-sustainability.

The most typical type of photocatalyst used is none other than TiO_2, which has a band gap of 3.2 eV. Shown in Figure 2.25 above is the schematic for photocatalytic oxidation. UV photons with $\lambda < 380$ nm excites the electron from the valence band of TiO_2, creating a hole (h+) which oxidizes volatile organic compounds (VOCs) and water, while the excited electron, e- is able to combine with oxygen to form the superoxide radical. The oxidation forms hydroxyl radicals and also leads to the eventual oxidation of VOCs into CO_2 and H_2O. All the processes involving e- and h+ must effectively compete with the electron hole recombination process occurring in the bulk or surface of the photocatalyst[138] for high efficiency in the degradation of the organic compounds.

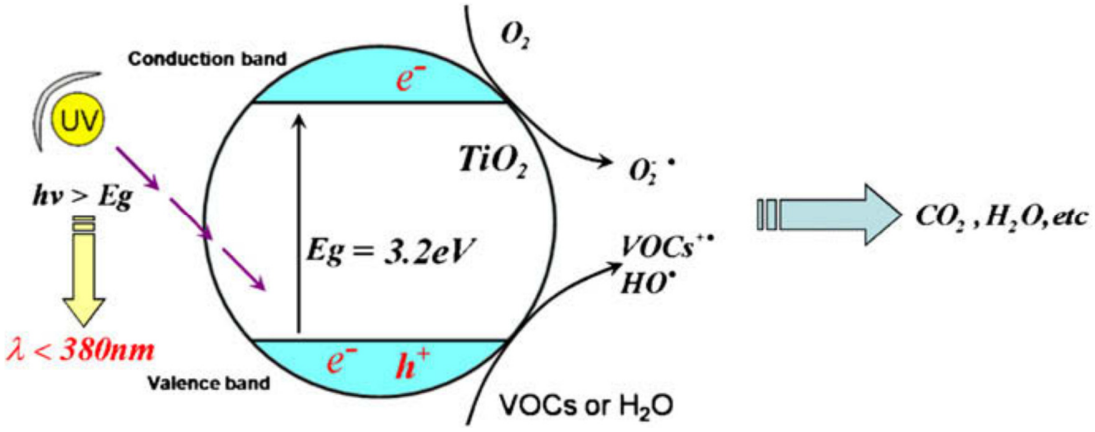

Figure 2.25 Schematic of photocatalytic oxidation using TiO_2 as catalyst for mineralization of volatile organic compounds (VOCs). Reprinted from reference[15]. Copyright 2009. With permission from Elsevier.

Much of the work involving homogeneous photocatalysis using polyoxometalates for water purification has been reported by Papaconstantinou et. al.[35]. It has been demonstrated that the use of Keggin type polyoxometalates has the capability to degrade a variety of organic derivatives. Chlorophenols and chloroacetic acid has been oxidized with the efficiency of polyoxometalates measuring up to that of TiO_2[35]. The removal of phenol, p-cresol[36], atrazine, metal ions (photoreduction)[39], azo-dyes (i.e. Acid orange 7)[38] etc. has been reported in the literature with reasonable effectiveness.
In more recent years, some developments have proceeded in the direction of POM composites with TiO_2 and other material as an enhancement or support for the effective application as a photocatalyst[141].

2.5.2. Catalytic wet air oxidation (CWAO)

Another powerful method used in the purification of wastewater seen in numerous studies over recent years is the catalytic wet air oxidation[142-144]. In comparison to the conventional methodology of wet air oxidation, the addition of oxidation catalysts in the process enable improved oxidation rates at milder conditions. Similar to other advance oxidation processes, CWAO is able to oxidize organics to innocuous inorganic products like H_2O and CO_2. The effectiveness of removal in organics depends on the type and amount present, which will eventually reduce the concentration or completely remove them from the water[145].

CWAO has been developed as a commercial process in the United States from mid-fifties[144]. The process was developed for both homogeneous and heterogeneous application[146]. From the environmental sustainability point of view, heterogeneous catalysis with materials of long lifetime and stability is desired. Common heterogeneous catalysts that have been synthesized are based on metal oxides or precious metal on stable catalyst supports. The list of catalyst includes mixtures of metal oxide of Mn, Co, Cu, Zn and Bi[145].

Heterogeneous catalysis by polyoxometalates under CWAO has been achieved with the use of alkylammonium cationic surfactant as a ligand exchange modifier. Zhao et. al.[147] reported the application of a micellar molybdovanadophosphoric POM with hexadecyltrimethylammonium bromide as the modifier for the catalytic wet air oxidation of phenol. Ambient conditions were used with the addition of air flow to aid in the re-oxidation of the catalyst. Furthermore, a few other reports of such micellar POMs system have been reported[148-150] for the degradation of dibenzothiophene, azo-dyes and thiocynate. Even though these works showed encouraging results of such systems, the structure of the materials are ill-defined and does not necessary reflect the true picture of the reactor system.

2.6. Conclusion

Polyoxometalates represents an extremely wide and diverse area of research. From the introduction of the various categorization and parent structure shown in this chapter, the size and structural diversity is the key to discovering new frontiers for the application of polyoxometalates. The formation of lacunary species also presents a platform for researchers to access the catalytic mechanism of heterogeneous catalyst from a homogenous perspective due to the highly soluble nature of polyoxometalates. Catalysis by polyoxometalates under the homogeneous regime has been well explored. However, in view of the need for sustainable technologies in catalysis, the highly soluble nature of polyoxometalates hinders their application as heterogeneous catalyst. Research has been done extensively on the heterogenization of polyoxometalates *via* immobilization on solid supports and solidification by choice of appropriate counter-cations. The use of heterogenised polyoxometalates in catalysis and redox-based reactions has also been studied. Design of such materials can be viewed from the perspective of nano-architectural design, where a bottom-up approach by combination of various component to construct advanced functional materials prove to be of significant value. Therefore, well-defined methods for heterogenization are required so as to understand the structural design essential to make the prepared materials effective catalysts. This will allow us to better understand the catalytic function of modified polyoxometalates catalysts which is a

target within this dissertation. The use of dye as model molecules for degradation is often reported and will be covered hereafter. Furthermore, the use of more challenging alternative molecules is also considered to attain better understanding of heterogeneous catalytic process by polyoxometalates.

Chapter 3

The synthesis of polyoxometalates nano-architectures, engineering, design and redox activity studies

Polyoxometalates (POMs) of the series $H_{(3+n)}[PV_nMo_{(12-n)}O_{40}]$ (PVMA) were prepared and investigated to assist in the design of POMs based materials. Basic characterizations of PVMA were performed to understand the structural and physiochemical characteristics. Two simple design approaches: (1) surfactant encapsulation of POMs and (2) surface modification of metal oxide for immobilization of POMs were adopted with the aim of obtaining a heterogenizing PVMA. In order to further investigate the redox characteristic of PVMA, PVMA-2 was chosen for incorporation with TiO_2 for application as anodes of lithium-ion battery. The preparation of TiO_2 via hydrothermal synthesis with the presence of PVMA-2 provided morphological control of TiO_2 growth with the use of unique interface created by two immiscible solvents. The TiO_2 nanoplates immobilized with PVMA-2 via (3-aminopropyl)triethoxysilane as a coupling agent was studied for its redox properties. The results show enhanced performance of the TiO_2-PVM hybrid in comparison with the individual components demonstrating the synergistic effect TiO_2-PVM hybrid and the potential of such material for application in lithium ion battery. This also provides insights for design of POMs immobilized materials for environmental applications.

3.1. Introduction

Polyoxometalates plays an important in catalysis, therefore, it is essential to have fundamental understanding of the synthesis of polyoxometalates. Research accounting for the synthesis of polyoxometalates are well-documented[16,32,46,151-155]. The studies done in this area usually involves the use of synthetic strategies involving the preparation of polyoxometalates in aqueous and non-aqueous mediums[156-158], incorporation of organic and organometallic functionalities to polyoxometalates structure[159], replacement of oxygen with sulphur as ligand[160] and the use of a synthon based approach for syntheses of large polyoxometalates clusters[161,162]. The basic preparation and understanding of the physiochemical properties of polyoxometalates is essential in understanding the approach for effective use of polyoxometalates and practicing within the research field. Therefore, this chapter primarily focuses on the synthesis, design and engineering of the materials providing a foundation for the work presented in this dissertation.

The most commonly studied polyoxometalates is the heteropolyacid (HPA) best represented by the Keggin structure[163]. HPA typically have low surface area and high solubility, which makes it challenging to use them as catalytic materials in aqueous media[3]. In this chapter, the synthesis of a mixed addenda Keggin type heteropolyanion of the series $H_{(3+n)}[PV_nMo_{(12-n)}O_{40}]$ (PVMA) will be described and characterized. Much research has been performed by researchers on this series due to their high redox reversibility, where re-oxidation can be achieved with molecular oxygen as a benign oxidant[93]. With the motivation to design and engineer PVMA towards a heterogeneous catalyst in aqueous media, this chapter will firstly cover the preparation of polyoxometalates-based organic-inorganic surfactant encapsulated heteropolyanion which will be studied in detail in Chapter 5. Secondly, a surface modification approach will then be studied by immobilizing polyoxometalates onto a metal oxide surface. The synthesis firstly targets the direct incorporation of PVMA into TiO_2 while controlling the formation of (001) facets *via* a hydrofluoric acid (HF) free synthesis. By making use of solvent interface between two immiscible mediums, direct incorporation PVMA-2 into the TiO_2 crystal structure *via* a one-pot synthesis was attempted in this chapter. This was done to

restrict the growth and allow the formation of TiO_2 nano-plates with large quantity of a single facet. Exposed (001) facets of TiO_2 are highly reactive and have been used in advance oxidation processes as a photocatalyst[45,164], dye-sensitized solar cell[165] and photocatalytic water splitting[166,167]. Such nanostructure has also found application as lithium-ion battery anodes[168] as the structure facilitates more efficient lithium-ion transport[169]. We believe that the incorporation of PVMA-2 here which is a highly redox-active molecular metal oxide will provide synergistic effect as a lithium ion battery catalyst. This will be exemplified at the end of this chapter to investigate the redox capabilities of PVMA-2, establishing parameters for the use of such material design for application in environmental remediation.

3.2. Experimental

3.2.1. Materials

All chemicals used are of reagent grade and used without further purification. Disodium hydrogen phosphate (Na_2HPO_4), sodium vanadate ($NaVO_3$), sodium molybdate dihydrate ($Na_2MoO_4 \cdot 2H_2O$), titanium(IV) tetraisopropoxide ($Ti(OCH(CH_3)_2)$), (3-aminopropyl)triethoxysilane ($H_2N(C_3H_6)Si(OC_2H_5)_3$) was purchased from Sigma-Aldrich. Hexane (C_6H_{12}, Aik Moh) hydrochloric acid (HCl, 37%, Merck), ethanol (C_2H_5OH, 99%, Merck) , concentrated sulfuric acid (H_2SO_4, 99%, Honeywell)

3.2.2. Synthesis of $H_4[PVMo_{11}O_{40}]$

$NaVO_3$ (6.1 g, 0.050 mol) was dissolved by boiling in water (100 mL) and mixed with Na_2HPO_4 (7.1 g, 0.050 mol) dissolved in water (100 mL). The mixture was cooled and acidification of the mixture was performed using concentrated sulfuric acid (5 mL), giving rise to a red colour solution. A solution of Na_2MoO_4 $2H_2O$ (133 g, 0.55 mol) dissolved in water (200 mL) was added to the mixture. Concentrated sulfuric acid (85 mL) was added drop-wise with vigorous stirring of the solution. Solution colour transited from dark red to lighter red upon addition of the acid. The aqueous mixture was allowed to cool before

being extracted with diethyl ether (400 mL). The heteropoly etherate was present in the middle layer. After separation was achieved, a stream of air was passed through the heteropoly etherate layer to free it of diethyl ether. The remaining orange solid was dissolved in appropriate amount of water to obtain a saturated solution. The solution was further concentrated in a vacuum desiccator over concentrated sulfuric acid to allow for crystallization of the product. The orange crystals were filtered, collected and left to air dry.

3.2.3. Synthesis of $H_5[PV_2Mo_{10}O_{40}]$

Na_2HPO_4 (7.1 g, 0.050 mol) was dissolved in water (100 mL) and added to $NaVO_3$ (24.4 g, 0.2 mol) dissolved by boiling water. The above solution was cooled and added with concentrated sulfuric acid (5 mL), and solution developed to a red colour. $Na_2MoO_4 \cdot 2H_2O$ (121 g, 0.50 mol) dissolved in water (200 mL) was added to the red solution, followed by slow addition of concentrated sulfuric acid (85 mL) with vigorous stirring. The resulting hot solution was cooled to room temperature. Extraction of the acid was performed using diethyl ether (500 mL). Diethyl ether was removed by passing a stream of air through the extracted medium. The solid that remained was dissolved in water to obtain a saturated solution and concentrated over concentrated sulfuric acid to obtain large red crystals of $H_5[PV_2Mo_{10}O_{40}]$.

3.2.4. Synthesis of $H_6[PV_3Mo_9O_{40}]$

A solution of Na_2HPO_4 (7.1 g, 0.050 mol) was prepared by dissolved in water (50 mL) and added to a solution of $NaVO_3$ (36.6 g, 0.30 mol) dissolved in hot water (200 mL). An addition of concentrated sulfuric acid (5 mL) was made to obtain a cherry red colour solution. $Na_2MoO_4 \cdot 2H_2O$ (54.4 g, 0.225 mol) was dissolved in water and mixed with the acidified mixture. The solution was stirred vigorously with addition of concentrated sulfuric acid (85 mL) simultaneously. The solution was allowed to cool to slow temperature and then extracted with diethyl ether (400 mL). The heteropoly etherate present as the middle layer was collected and freed of diethyl ether by passing of a stream

of air through the solution. A red solid remained and was dissolved in water to obtain a saturated solution. The solution was further concentrated over concentrated sulfuric acid in a vacuum desiccator to formation of red crystals. The red crystals were then filtered and collected.

3.2.5. Synthesis of surfactant encapsulated heteropolyanion (SEH)

The synthesis of the surfactant encapsulated heteropolyanions (SEHs) uses a single phase approach.[170] In the particular synthesis of SEH–1 ($(C_{18}H_{37})_2(CH_3)_2N)_4[PMo_{11}VO_{40}]$, the surfactant, dimethyldioctadecylammonium bromide (DMDOA·Br) (2.83g, 4.48 mmol) was firstly dissolved into a solvent mixture of n-butanol and chloroform in 1:3 volume ratio. The solid MVPA–1 (2.0 g, 1.12 mmol) is added in small portions with ultra-sonication to ensure that each portion is fully dissolved and a clear solution is obtained after each addition. This is performed such that the ratio of MVPA to surfactant was slowly adjusted to 1:4. After the complete addition of MVPA–1, the solvent was allowed to evaporate to dryness and the solid material was collected, herein denoted as surfactant encapsulated heteropolyanion–1 (SEH–1). The same procedure was followed using MVPA–2 and MVPA–3 with adjustment in the stoichiometric ratio of surfactant added, where SEH–2 and SEH–3 were collected upon evaporation of solvent.

3.2.6. Synthesis of $H_5[PV_2Mo_{10}O_{40}]$ modified TiO_2 NP (TiO_2-PVM)

The synthesis of TiO_2 was carried out as follow. 0.2 g of $[H_5[PMo_{10}V_2O_{40}]\cdot 32\ H_2O]$ was dissolved in 1 mL ultrapure water. 9 mL of concentrated HCl (37%, 12M) was added and charged to a 45 mL Teflon sleeve. 0.6 mL of TTIP was mixed with 19.4 mL of hexane, this mixture was then carefully added into the Teflon without mixing with the aqueous layer. The Teflon was then sealed in a stainless-steel autoclave and heated at 170 °C for 24 h. The resulting TiO_2 was collected after cooling and washed 3 times with a mixture of 10 mL of water and ethanol (50% v/v) and dried in a vacuum oven at 40 °C for 24 h. The as-prepared TiO_2 was dispersed into an absolute ethanol solution containing APTES (1.5 % v/v) and magnetically stirred for 24 h for surface aminization. It is then centrifuged and

washed with 10 mL ethanol 3 times before being dried in a freeze dryer for 24h. The surface aminated TiO_2 was dispersed into 15 mL absolute ethanol containing 0.2 g of $[H_5PMo_{10}V_2O_{40}\cdot 32\ H_2O]$ and stirred for 24 h. The resulting POM-TiO_2 was washed until the yellowish colouration $[H_5PMo_{10}V_2O_{40}\cdot 32\ H_2O]$ was no longer observable and then freeze dried for 24 h before used for further application.

3.2.7. Material Characterization

The as prepared samples were grinded with KBr and pressed into pellet form for analysis by Fourier transform infra-red spectroscopy (Perkin Elmer FTIR- Frontier). The morphology and elemental analysis of the as-synthesized TiO_2 and PVMA-2 modified material was analysed by a field emission scanning electron microscope (FESEM JEOL-7600F). Powder XRD patterns were obtained by Bruker D8 Advance Diffractometer with monochromated CuKα (λ = 1.5418 Å) with step size of 0.02° s^{-1}. Brunauer-Emmett-Teller (BET) specific surface area was determined using N_2 adsorption-desorption isotherm analysis at 77K (Quantachrome Quadrasorb SI). Samples were degassed at 423 K for 16 h under vacuum before analysis. Thermogravimetric analysis (TGA) was performed using TA instrument TGA Q500. Temperature was ramped up from room temperature to 100 °C at a rate of 5 °C min^{-1}, held isothermally at 100 °C for 15 mins, ramped up to 200 °C at a rate of 10 °C min^{-1}. It is then finally and ramped up to 500 °C at 10 °C min^{-1}.). Samples were dispersed in ethanol and dripped onto a copper grid with holey carbon support to study the local structure using a transmission electron microscope (TEM JEOL-2100F) at an accelerating voltage of 200 kV with a point to point resolution of 1.9 Å.

3.2.8. Electrochemical studies of redox activity of TiO_2-PVM

All electrodes were prepared by mixing the active materials with Super P and 8% wt of polyvinylidene fluoride (PVDF) binder in a weight ratio of 7:2:1 in N-methylpyrrolidinone (NMP). The slurry was then drop-casted on the copper foil and dried in the vacuum oven overnight. These electrodes were assembled in a coin-type cell using Li foil as reference electrode, a Celgard 2400 membrane as separator, and electrolyte

solution containing 1 M $LiPF_6$ in a mixture of ethylene carbonate (EC) and dimethyl carbonate (DME) with 50:50 w/w ratio. The galvanostatic discharge and charge cycles were carried out in the potential range of 0.01-3.0 V using a NEWARE battery tester. The cyclic voltammetry (CV) was conducted using a Solartron analytical equipment (model 1470E), scanning at a rate of 0.2 mV s^{-1} at 0.01-3 V potential window. Electrochemical impedance spectroscopy (EIS) measurements were performed using a Metrohm autolab electrochemical workstation with an amplitude of 10 mV in the frequency range from 100 kHz to 0.01 Hz.

3.3.1. Characterization of $H_{(3+n)}[PV_nMo_{(12-n)}O_{40}]\cdot x\ H_2O$

The synthesis of Keggin type phosphovanadomolybdic acid (PVMA) lays the foundation for the preparation and modification of materials found in this dissertation. It is therefore of utmost importance to understand the structure properties and physical characteristics of the synthesis crystals. Using FTIR spectroscopy, the characteristic bonding in the PVMA were identified and presented in Figure 3.1. The characteristic peaks of the Keggin structure can be found in the range of 1100 – 700 cm^{-1}. And the characteristic wavenumbers are summarized in Table 1 The main features are from P–O_a bonding of the centre tetrahedral, M–O_b–M corner sharing bridging oxygen, M–O_c–M edge sharing bridging oxygen and M=O_d terminal oxygen (where M = Mo or V). The characteristic bands of P–O_a, M=O_d and M–O_b–M in PVMA undergoes red shift with increase in vanadium substitution, which likely originate from the weaker metal oxygen bond due to vanadium (O.S. = 5+) being in a lower oxidation state that molybdenum (O.S. = 6+).

The powder XRD patterns of PVMA are shown in Figure 3.2. The diffraction peaks show that the PVMA prepared consist of mainly a single crystalline phase. Most of the peaks can be indexed and are consistent with PDF#00-045-0611, PDF#04-015-6856 and PDF#01-084-0235 of $H_4[PVMo_{11}O_{40}]$, $H_5[PV_2Mo_{10}O_{40}]$ and $H_6[PV_3Mo_9O_{40}]$ of space group P4/mnc with tetragonal crystal structure. The lattice parameters of the crystals are close in values with $H_4[PVMo_{11}O_{40}]$ having a=12.862Å and c=18.292 Å, with the incorporation of increasing number of vanadium atoms in place of molybdenum, the influence on the XRD peak position and intensity is minute. The small reflection peaks appearing in the diffraction patterns of each PVMA are common, especially in powdered samples due to loss of water molecules which easily influence the crystal structure of PVMAs.

Table 3.4 Characteristic wavenumbers of as-synthesized $H_{(3+n)}[PV_nMo_{(12-n)}O_{40}]$ (n = 1, 2, 3)

	Characteristic Wavenumber (cm^{-1})			
Sample	**(P–O_a)**	**(M=O_d)**	**(M–O_b–M)**	**(M–O_c–M)**
$H_4[PMo_{11}VO_{40}]$	1060.4	960.2	866.3	776.3
$H_5[PMo_{10}V_2O_{40}]$	1060.3	960.1	864.2	776.1
$H_6[PMo_9V_3O_{40}]$	1059.4	959.3	863.3	776.3

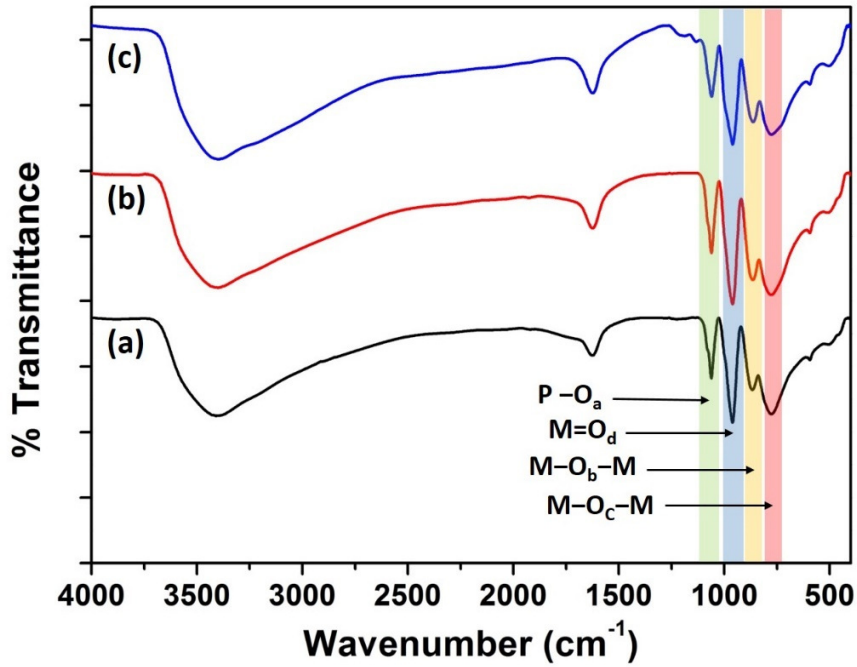

Figure 3.1 FTIR spectra of (a) $H_4[PVMo_{11}O_{40}]$, (b) $H_5[PV_2Mo_{10}O_{40}]$ and (c) $H_6[PV_3Mo_9O_{40}]$.

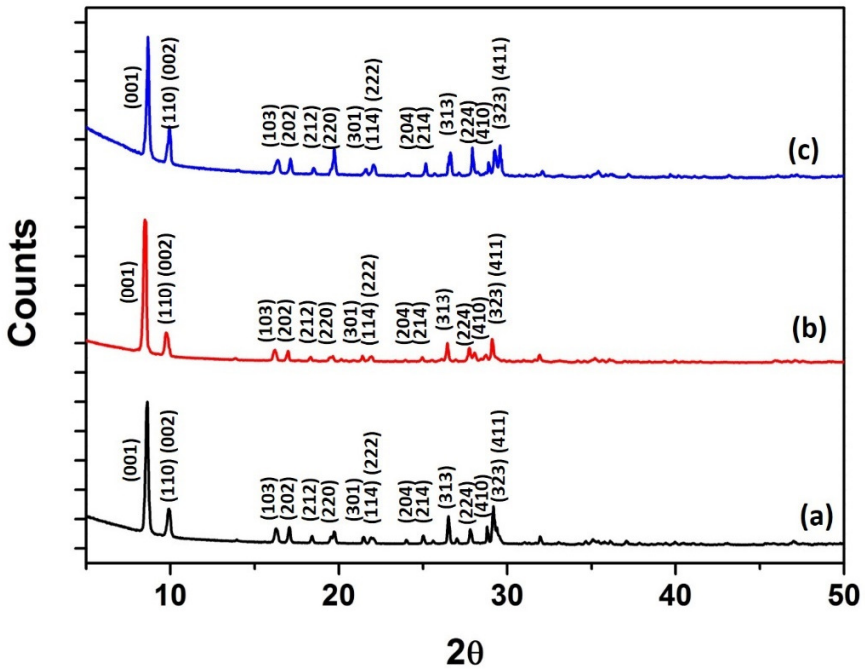

Figure 3.26 XRD diffractogram of (a) $H_4[PVMo_{11}O_{40}]$, (b) $H_5[PV_2Mo_{10}O_{40}]$ and (c) $H_6[PV_3Mo_9O_{40}]$ with the characteristic reflection peaks of the Keggin structure labelled.

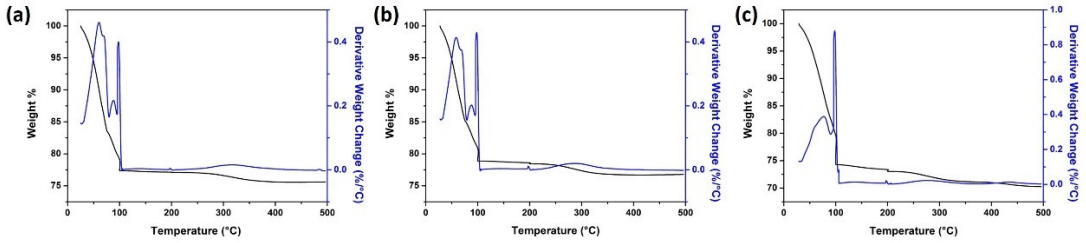

Figure 3.3 Thermogravimetric analysis weight loss profile of (a) $H_4[PVMo_{11}O_{40}]$, (b) $H_5[PV_2Mo_{10}O_{40}]$ and (c) $H_6[PV_3Mo_9O_{40}]$.

Figure 3.3 above shows the thermogravimetric weight loss profile of PVMAs. The crystals effloresce slowly even at room temperature and the large amount of water of crystallization which are loosely attached are easily lost as temperature increases. It can be seen that all 3 samples experience major weight loss as the temperature increases up to 100 °C. The temperature setting for the analysis was made to hold at 100 °C and 200 °C so as to remove the water of crystallization completely. The 2nd derivative weight loss peak appearing around 300 °C is associated with the removal of the structural water molecules holding the secondary structure of the PVMAs. The calculation from the overall weight loss reveals that associated water of crystallization and chemical formula of the PVMs prepared to be $H_4[PMo_{11}VO_{40}]\cdot 32\ H_2O$, $H_5[PMo_{10}V_2O_{40}]\cdot 29\ H_2O$ and $H_6[PMo_9V_3O_{40}]\cdot 35\ H_2O$ respectively.

3.3.2. Synthesis and characterization of TiO_2-PVM

With the aim of heterogenizing PVMA via immobilization, a one-pot solvothermal synthesis was designed to incorporated $H_5[PV_2Mo_{10}O_{40}]$ (henceforth referred to as PVMA-2) into the crystal lattice of TiO_2. The desired outcome was to attain morphological control along with PVMA-2 incorporation in the TiO_2 crystals for the final product. However, the immobilization of PVMA-2 within the TiO_2 was not effective *via* a one-pot synthesis and thus a stepwise modification was adopted as shown in Figure 3.4 (a), the micrograph of the synthesized product is shown in Figure 3.4 (b). Even though the TiO_2 prepared has nano-plate morphology, the EDX spectra in Figure 3.4(c) only show trace amount of molybdenum and vanadium. This indicates that incorporation of

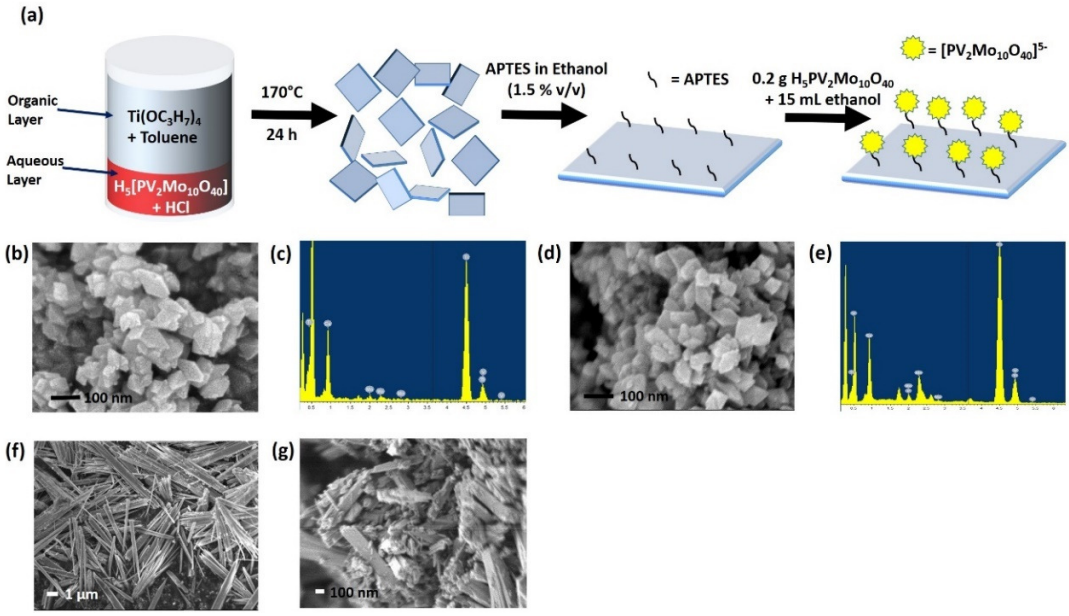

Figure 3.27 (a) Schematic of PVMA-2 modified TiO2 NP synthesis. As synthesized TiO2 (b) SEM micrograph and (c) EDX spectra. PVMA-2 modified TiO2 (d) SEM micrograph and (e) EDX spectra. Solvothermal synthesis (f) without PVMA-2 in aqueous layer and (g) with APTES in organic layer.

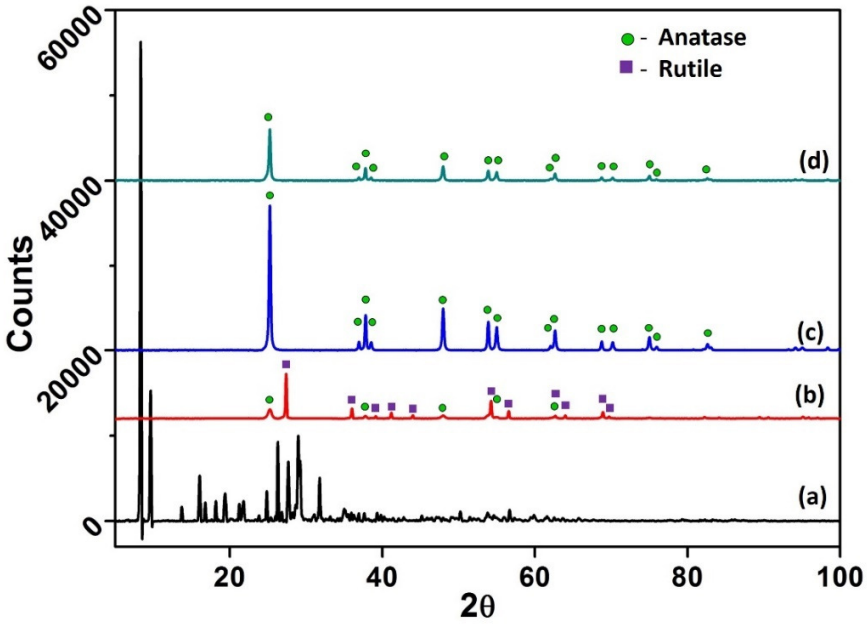

Figure 3.5 XRD diffractogram of (a) $H_5[PV_2Mo_{10}O_{40}]\cdot 29H_2O$, TiO_2 synthesized (b) without PVMA-2 in aqueous layer, (c) with PVMA-2 in aqueous layer and (d) PVMA-2 modified TiO_2 NPs (TiO_2-PVM).

PVMA-2 in the TiO_2 crystal or attachment *via* electrostatic interaction with the surface -OH_2^+ groups is ineffective. The attached PVMA-2 is generally washed off during the washing process as observed by the colour of wash off during the washing cycle. In order to improve the coupling of PVMA-2 with the TiO_2 surface, (3-aminopropyl)triethoxysilane (APTES) was employed as a coupling agent. It can be seen from Figure 3.4(d) that the immobilization of PVMA-2 with the assistance of APTES does not influence the morphology of the final product. Moreover, the EDX spectrum in Figure 3.4(e) shows a substantial increase in elemental composition of molybdenum and vanadium.

In view that the use of PVMA-2 during the solvothermal synthesis process does not contribute to its successful attachment on the TiO_2 surface, synthesis was performed without the use of PVMA-2 in the aqueous phase. Thus, a rod-like morphology with a mixed crystal phase of rutile and anatase was obtained as a result as shown in Figure 3.5(b). The addition of PVMA-2 during the synthesis was able to adjust the hydrolyzation reaction rate, provide morphological control and phase formation of TiO_2[171].This can be seen from the XRD diffractogram of the TiO_2 product obtained in Figure 3.5(c). No crystalline phase of PVMA-2 (Figure 3.5(a)) was observed in the diffractogram, which agrees well with the EDX results that PVMA-2 was not effectively immobilized during the synthesis process. The immobilization of PVMA-2 on TiO_2 using a coupling agent increases the relevant elements of PVMA-2 detected, but does not lead to formation of detectable PVMA-2 crystalline phase. The main influence post-modification was a decrease in the reflection intensity, which can be attributed to the reduction in reflected X-ray due to the surface modification. Further attempts to reduce the number of steps required in synthesis by introducing APTES in the organic phase during synthesis for surface modification proved to be futile and resulted in poor morphological control.

The above unveil the function of PVMA-2 in the morphological control in preparation of the TiO_2 nano-plate. Polyoxometalates are known to be capable of stabilizing and protecting metal nanoparticles during their formation[172], therefore it is likely that Cl^- and

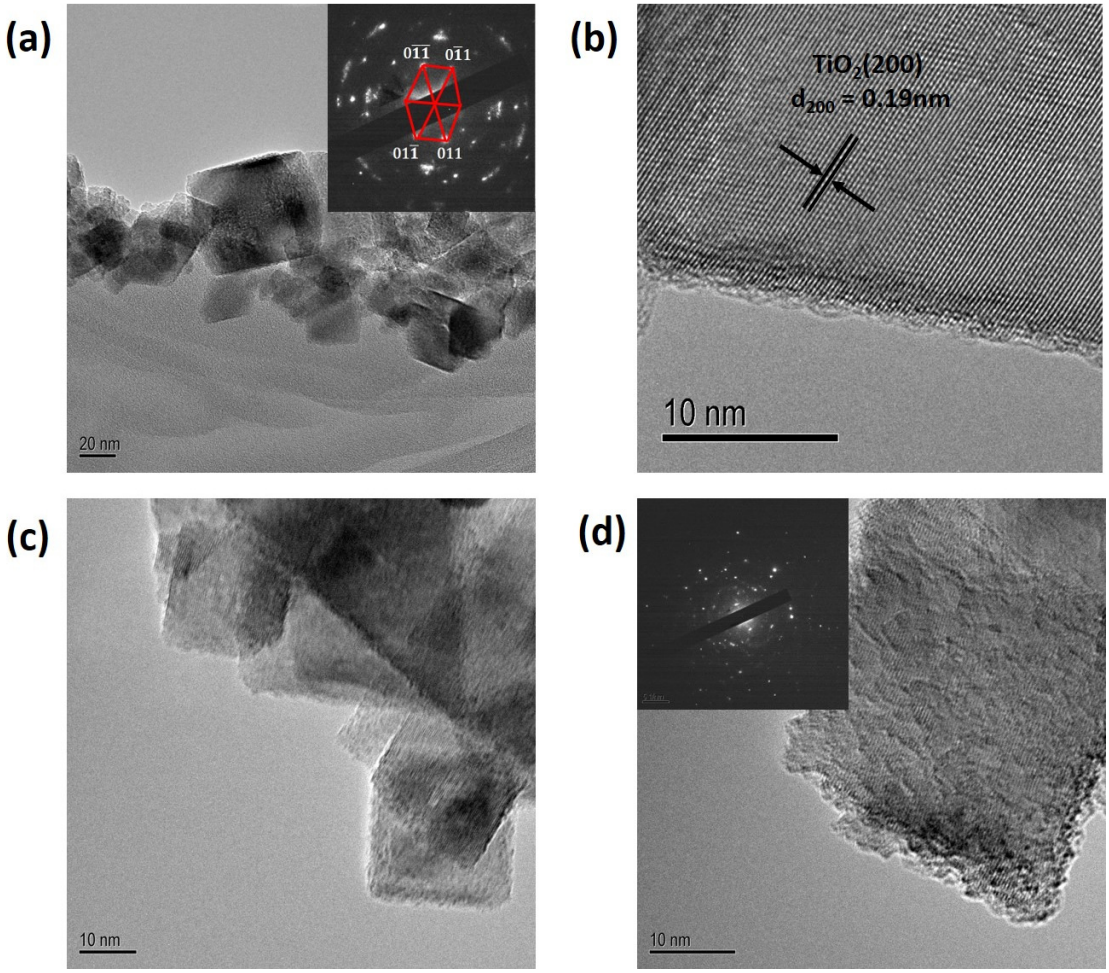

Figure 3.6 TEM micrograph of TiO_2 NP (a) at low magnification (inset shows the corresponding SAED pattern taken close to [100] zone axis) (b) at high magnification. TEM micrograph of TiO_2-POM (c) at low magnification and (d) at high magnification (inset shows corresponding SAED pattern).

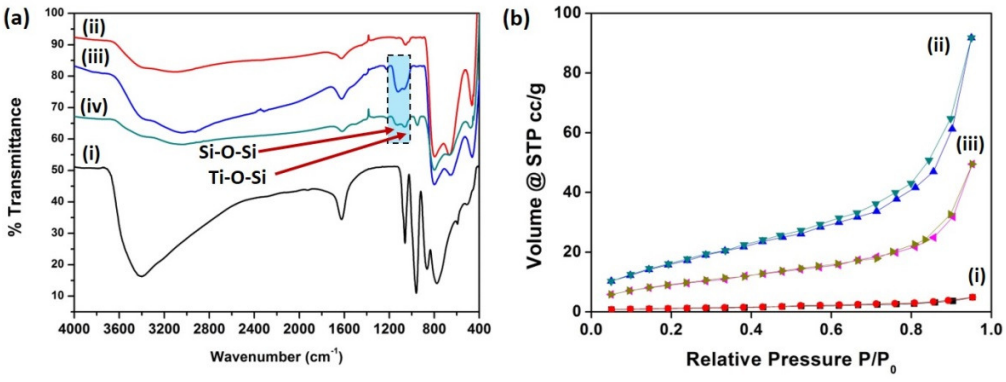

Figure 3.7 (a) FTIR spectra of (i) PVMA-2, (ii) TiO_2 NP, (iii) APTES modified TiO_2 NP and (iv) TiO_2-PVM. (b) N_2 adsorption/desorption isotherm of (i) PVMA-2, (ii) TiO_2 NP and (iii) TiO_2-PVM.

PVM^{5-} ions in the aqueous phase plays the role of assisting in the crystallization and stabilization process, while the aqueous and organic interface acts as a template for the formation of the plate-like morphology. Figure 3.6(a) shows the TEM images of TiO_2 NP and an inset of the SAED taken close to [100] zone axis showing the indexing of the diffraction pattern. In Figure 3.6(b), the nano-plate is highly crystalline with the lattice of the nano-plate clearly observable and labelled as the d_{200} plane. Figure 3.6 (c) shows TiO_2-PVM, with the surface of the TiO_2 NP now decorated with PVMA-2. At higher magnification in Figure 3.6(d), the modification can be seen in greater detail and the SAED pattern (inset) shows different crystalline phases present in the area analysed indicative of the presence of small regions of PVMA-2 crystalline phase.

Figure 3.7(a) shows the FTIR spectra of the as prepared samples. In Figure 3.7 (a)(ii), the usual broad peak typical of TiO_2 in the region of 700 – 400 cm^{-1} was not observed[173]. A strong band was observed at 799 cm^{-1}, which can be assigned to the presence of M-O-M bond stretching due to PVMA-2 adhered to the surface during the synthesis process. In Figure 3.7(a)(iii), characteristic bands at 1121 and 1061 cm^{-1} can be assigned to the Si-O-Si and Ti-O-Si bonds formed during surface modification with APTES. With the addition of PVMA-2 as a final modification, a band at 951 cm^{-1} characteristic of terminal Mo=O bond in PVMA-2 can be observed, providing evidence for the successful stepwise modification of the TiO_2 NP surface. Figure 3.7(b) shows the N_2 adsorption/desorption isotherm of the as prepared materials. The surface area of PVMA-2, TiO_2 NP and TiO_2-PVM are 4.2, 62.77, 33.9 $m^2\ g^{-1}$. The reduction in surface area of the TiO_2 NP indicates a successful modification of the NP surface with PVMA-2. A reduction in the pore volume of the TiO_2 NP from 0.086 cc g^{-1} to 0.043 cc g^{-1} in the PVMA-2 modified sample also indicates successful attachment of PVMA-2 within the pores.

3.3.3. Redox activity of TiO_2-PVM in lithium-ion battery

The electrochemical mechanistic studies of the as-prepared samples were evaluated using cyclic voltammetry (CV) to understand the electrochemical behaviours for the three different electrodes (i.e. TiO_2 NP, PVMA-2 and TiO_2-PVM) between 0.01 to 3.0 V at a

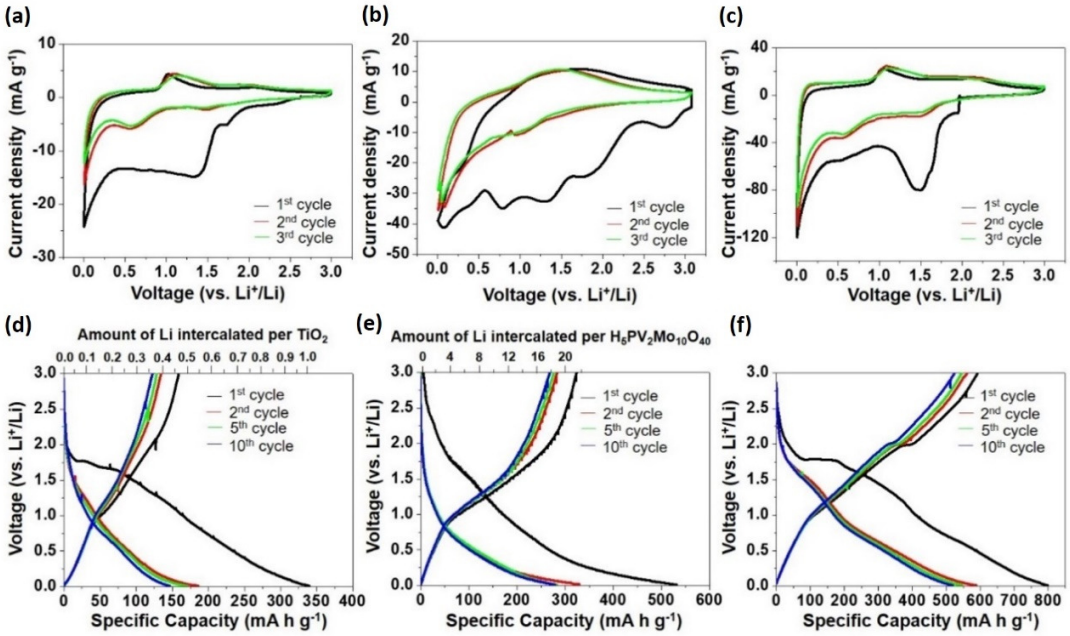

Figure 3.8 Cyclic voltammograms of (a) TiO_2, (b) PVM and (c) POM-TiO_2 electrodes at 0.01-3 V potential window and a scan rate of 0.2 mV s^{-1} for the first three cycles. Galvanostatic discharge-charge voltage profiles at 0.1 A g^{-1} for the 1st, 2nd, 5th and 10th cycle of (d) TiO_2, (e) POM and (f) POM-TiO_2 electrode.

scan rate of 0.2 mV s^{-1} (Figure 3.8(a-b)). It was found that the CV curves of the bare TiO_2 and TiO_2-PVM hybrids were almost identical (compare Figure3. 8(a) and (c)). This might be due to the low amount of PVM attached on the TiO_2, resulting in the latter active material dominates the CV curves. During the first scan for the three samples, a notable cathodic peak at ~0.5 V is attributed to the formation of solid electrolyte interface (SEI) as a consequence of organic electrolyte decomposition.[174,175] During the subsequent cycles, the cathodic and anodic peaks were shifted form the 1st cycle due to the formation of SEI layer induced overpotential polarization.[176] In particular, the cathodic peaks at the range of 1.38-1.90 V and the anodic peaks at 2.01-2.11 V, corresponding to the intercalation and extraction of Li^+ ions in TiO_2 crystal structure:

$$xLi^+ + xe^- + TiO_2 \leftrightarrow Li_xTiO_2 \qquad \text{where } 0 \le x \le 1.0^{177} \qquad \text{Eqn(3.1)}$$

To investigate the redox reactions of PVM, a CV measurement was performed on the PVM electrode. Four distinct cathodic peaks at 2.77, 1.77, 1.33 and 0.77 V are ascribed to the reduction of Mo^{6+} ions to Mo^{4+} ions and V^{5+} ions to V^{4+} ions.[178,179] On the other hand,

a broad anodic peak at a range of 0.82-2.33 V is ascribed to oxidation of the reduced species. These results indicate that Li^+ ions insertion/extraction in the POM cluster takes place via multistep processes. In the subsequent cycles, the peaks are less pronounced, and the CV curves resemble that of supercapacitor rather than a typical intercalation process. This capacitive behaviour is in accordance with some of the literatures, implying that the Li^+ ions do not undergo intercalation process but rather surface-induced capacitive process.[180,181] The surface-induced capacitive mechanism includes the adsorption of Li^+ ions on the surface of the material and over the PVM cluster.[182,183] The discharging-charging mechanism of PVM is proposed and described as:

$$xLi^+ + xe^- + [PV_2^{5+}Mo_{10}^{6+}O_{40}]^{5-} \leftrightarrow Li_x[PV_2^{4+}Mo_{10}^{4+}O_{40}]^{(5+x)-} \quad \text{Eqn (3.2)}$$

When x = 22 and range of x: $0 \leq x \leq 22.0$.

The reduction of V^{5+} to V^{4+} would accommodate 2 Li^+ ions per unit of $H_5PV_2Mo_{10}O_{40}$, while reduction of Mo^{6+} to Mo^{4+} would accommodate 20 Li^+ ions per unit of $H_5PV_2Mo_{10}O_{40}$. Therefore, the predicted theoretical amount of Li^+ ions that the as-prepared POM could hold is up to 22.

In the 1st discharge cycle at 0.1 A g^{-1}, the specific capacities of 340, 531 and 800 mAh g^{-1} corresponding to TiO_2, PVM and TiO_2-PVM electrodes were obtained, respectively (Figure 3.8(d-f)). These high values could be attributed to the formation of SEI layer due to decomposition of electrolyte as explained in the CV voltammogram above. In the following cycles, the discharging specific capacities of TiO_2, PVM and TiO_2-PVM electrodes stabilize on the 10th cycle and they are about 143, 276 and 516 mAh g^{-1}. The specific capacities of TiO_2 (143 mAh g^{-1}) and PVM (276 mAh g^{-1}) corresponding to 0.4 Li per TiO_2 and 17.9 Li per $H_5PV_2Mo_{10}O_{40}$. The theoretical specific capacity that TiO_2/$H_5PV_2Mo_{10}O_{40}$/ hybrid is the sum of TiO_2 (335 mAh g^{-1} for $Li_{1.0}TiO_2$) and $H_5PV_2Mo_{10}O_{40}$ (339 mAh g^{-1} for $Li_{22.0}H_5PV_2Mo_{10}O_{40}$), which is equal to 674 mAh g^{-1}. The as-prepared TiO_2-PVM electrode has a specific capacity lower than the theoretical value of hybrid, but it is much higher than the theoretical value of individual components.

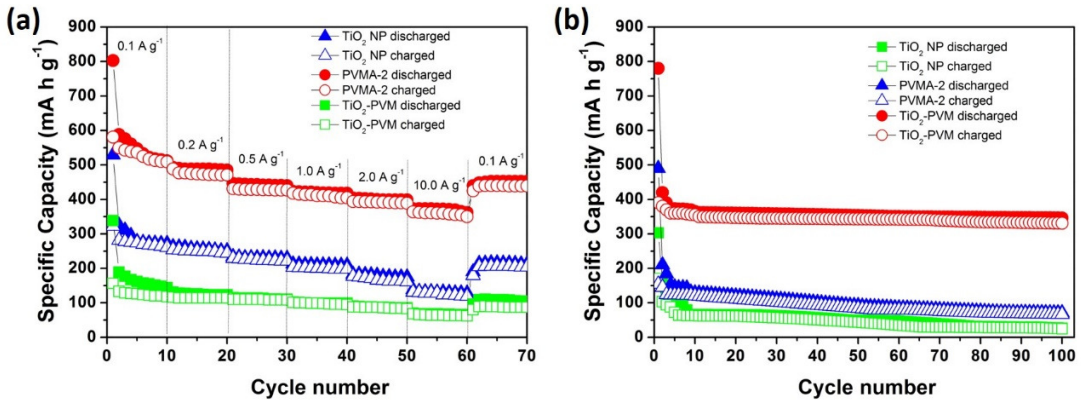

Figure 3.9 (a) Rate capability of the TiO_2, PVMA-2 and TiO_2-PVM electrodes at various current densities. (b) Cycling performance of the as-prepared samples at 10.0 A g^{-1}. All of the measurements were evaluated at potential range of 0.01-3 V.

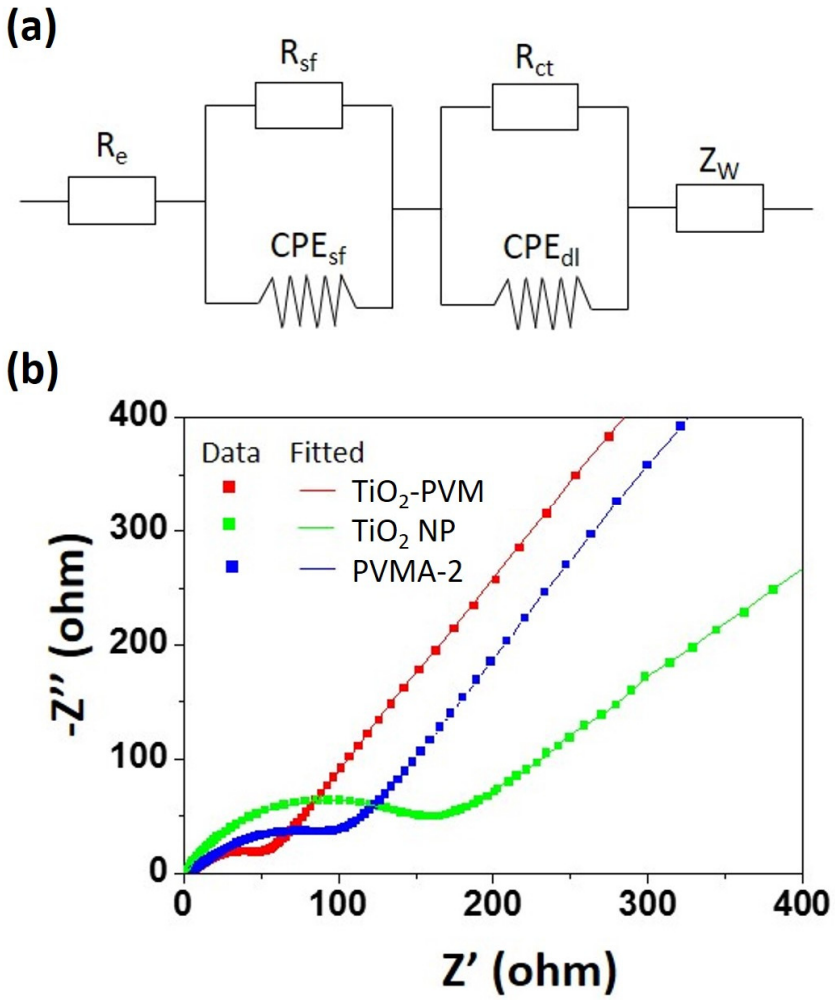

Figure 3.10 (a) Equivalent circuit for electrochemical system. (b) Nyquist plots of as-prepared samples.

The matching of the conduction band energy $H_5PV_2Mo_{10}O_{40}$ and TiO_2 materials allows an effective transference of charge from TiO_2 to $H_5PV_2Mo_{10}O_{40}$ as a charge reservoir[33]. The synergistic effect therefore leads to high specific capacity being obtained in the TiO_2-PVM electrode.

The rate performances of TiO_2, PVM and TiO_2-PVM electrodes were evaluated at different current densities of 0.1, 0.2, 0.5, 1.0, 2.0 and 10.0 A g^{-1} (Figure 3.9(a)). By increasing the current densities from 0.1 to 10.0 A g^{-1}, the specific capacities of TiO_2, POM and POM-TiO_2 electrodes decrease to 62, 123 and 361 mAh g^{-1}, which are corresponding to capacitive loss of 56%, 55% and 38%, respectively. This result implies that the TiO_2-PVM hybrid has a superior rate capability and can deliver high specific capacity of 361 mAh g^{-1} even cycled at high current density of 10.0 A g^{-1}. To examine the cycling performance of the electrodes, the TiO_2, PVM and TiO_2-PVM electrodes were cycled at 10.0 A g^{-1} for 100 cycles (Figure 3.9(b)). The capacity retentions for TiO_2, PVM

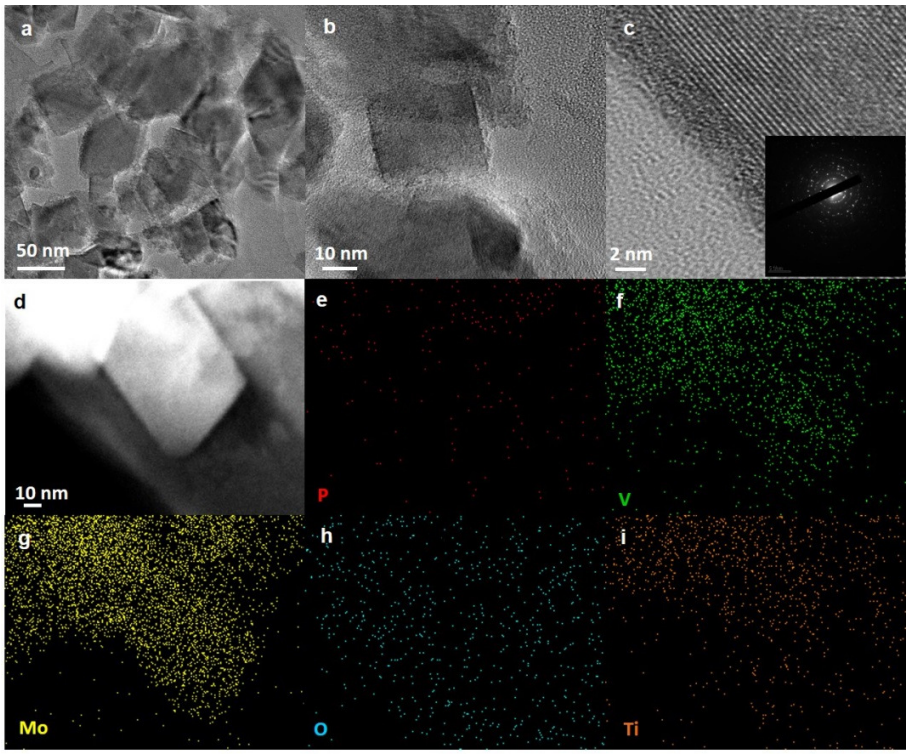

Figure 3.11 Characterizations of POM-TiO2 electrode after 100 cycles: (a-b) Low-magnification TEM images; (c) high-magnification TEM image with inset SAED pattern; (d) HAADF image and its corresponding elemental mapping images of (e) P, (f) V, (g) Mo, (h) O and (i) Ti elements.

and TiO_2-PVM electrodes after 100 cycles are estimated to be 35%, 56% and 95% of the 10^{th} cycle discharge capacity at 10 A g^{-1}, respectively. Among them, TiO_2-PVM electrodes exhibit outstanding cycling performance.

Figure 3.10(a) reveals the equivalent circuit for data fitting. The semicircle at high frequency can be ascribed to the electrolyte resistance and the surface of the film impedance (denoted as $R_e/R_{sf}/CPE_{sf}$), the semicircle at lower frequency can be ascribed to the lithium-insertion process (denoted as Rct/CPE_{dl}), and the linear curve represents the diffusion of Li^+ ion in the electrode material (denoted as Z_w) as shown in Figure 3.10(b). The TiO_2-PVM electrode has a smaller semicircle at 55.8 Ω compared to those other samples (PVM at 109 Ω and TiO2 at 180 Ω), indicating that TiO_2-PVM has a lower interface contact impedance and a lower charge transfer resistance for facile electron transportation within the material and easy insertion of Li^+ ions into the cavities, respectively. In addition, the Warburg line for PVM containing electrodes shows much steeper slope compared to that of TiO_2, implying that PVM facilitates rapid Li^+ ions diffusion from the bulk electrolyte to the surface of the electrode. This might be due to the redox characteristic of PVM which promotes fast Li^+ ions transportation.

To investigate the morphological, crystal structure and chemical stabilities of the TiO_2-PVM electrode, TEM, SAED, HAADF and STEM-EDX mapping analyses were conducted on the sample after 100 cycles (Figure 3.11). It was found that the original morphology was retained (Figure 3.11(a-b)). Therefore, we believed that the POM on the surface of the TiO_2 has adsorbed majority of the Li^+ ions, and thus restrict the drastic volume changes/structural deformation of TiO_2 upon lithiation/delithation processes. The amorphous layers found on the TiO_2 NP edges are believe to be the SEI layers (Figure 3.11(c)). In addition, the ring pattern diffraction spots in the SAED pattern, indicates that the material is polycrystalline, which might be due to crystal structural deformation of TiO_2 after long-term cycling. The HAADF image and its corresponding STEM-EDX mapping images show a uniform elemental distribution of P, V, Mo, O and Ti, suggesting that the POM clusters are still present on the TiO_2 NP after prolonged cycling (Figure 3.11(d-i)).

3.4. Conclusion

The syntheses of polyoxometalates and the formation of the Keggin ion structure play an important part in its various specific applications. More importantly, the Keggin structure enables materials to undergo extensive redox chemistry reaction, which is important in the aspect as a catalyst in lithium ion battery. In this chapter, the basic synthesis of polyoxometalates *via* acid condensation reaction followed by etherate extraction was described in detail. The use of the polyoxometalates of the $H_{(3+n)}[PV_nMo_{(12-n)}O_{40}]$ in the synthesis of surfactant encapsulated heteropolyanion was also described and will be further characterized in chapter 5. Its application as a wet air oxidation catalyst will also be exemplified. The immobilization of PVMA-2 on TiO_2 NP described in this chapter establishes foundation knowledge and understanding of such surface modification process. The synergistic effect derived from the combination of TiO_2 with PVMA-2 provided an attractive redox active material for lithium-ion battery with good cycling stability and electrochemical properties is highly encouraging in the research of such hybrid material. However, the low amounts of PVMA-2 immobilized on the surface of the TiO_2 NP likely due to insufficient surface amine groups and relatively low surface area of the TiO_2 NP could be reasons preventing the material from performing at optimum potential. While the objective was to use the TiO_2-NP prepared in chapter 3 as a photocatalyst, the deficiency of the material to act as a photocatalyst prevented the effective evaluation of the material in this aspect. Therefore, the redox activity of the material was investigated to evaluate the redox properties of $H_5PV_2Mo_{10}O_{40}$ when prepared as a composite *via* surface immobilization on TiO_2. This also allows better consideration of the parameters in the preparation of the nano-architecture in chapter 4 which can act as a photocatalyst with the effective immobilization and high surface area, where investigation will be done to optimize the surface modification using high surface area titanium oxide as solid support for effective immobilization of PVMA-2.

Chapter 4

Amine-functionalized titanate nanotubes for immobilization of heteropolyanion as visible-light responsive photocatalyst

An amine-functionalized titanate nanotube modified with di-vanadium-substituted molybdophosphoric acid (PVM) was prepared as a catalyst. The synthesis utilizes the high surface area of titanate nanotubes for immobilization of PVM, obtaining heterogeneity and high surface area in the as-prepared material for application as a photocatalyst. Amine-functionalization was attained by use of a coupling agent,3-aminopropyltriethoxysilane (APTES) and variation in percentage used during synthesis produced PVM-X%S-TNT (X = 2, 5, 10). Structural characteristics and physical properties of the as-prepared material was characterized by FTIR, XRD, TEM, SEM and XPS. PVM-5%S-TNT was found to be optimized for the photocatalytic degradation of MB with H_2O_2 added as an oxidant. The photocatalytic efficiency of the material was also tested against rhodamine B, methyl orange and acid orange 7. The results provided useful insights on the mechanism for photocatalytic degradation of organic dye by POMs.

4.1. Introduction

In this chapter, the objectives of study are as follows: (1) heterogenization of phosphodivanadodecamolybdate (PVM), (2) attainment of high surface area for improved photocatalytic activity and (3) study of parameters influencing photocatalytic degradation of methylene blue and its mechanism. Firstly, the heterogeneous catalyst design will be achieved through the surface modification of a support material with polyoxometalates. The modification of oxide support generally involves synthesis with high temperature[184,185], direct incorporation of heteropolyanion with support material can also result in low loading[98]. The use of sol-gel hydrothermal synthesis to directly incorporated heteropolyanion into TiO_2 lattice might not be facile for different kinds of heteropolyanion, as reaction conditions might affect the redox state and structure of heteropolyanion thus affecting the effective application of such POMs based material[18]. Similar to the example in chapter 3, 3-aminopropyltriethoxysilane (APTES) was selected as a coupling agent, which is known to improve loading[186] and stability[115] of POMs. The coupling agent silanizes the surface, providing cationic amine surface for immobilization of heteropolyanion. The link for immobilization here is electrostatic in nature, and the high anionic charge of heteropolyanions (PVM has an anionic charge of 5-) makes the immobilization process more robust. In Chapter 3, the loading of PVM was likely too low for it to be effectively used as a photocatalyst which also limited its effectiveness as a catalyst in lithium ion battery. The increase in surface bound PVM *via* surface immobilization here aims to improve the functionality and investigation of its potential application as a photocatalyst.

Titanate nanostructure prepared from TiO_2 under alkaline conditions[187] are known to be superior adsorbent for organic dyes and heavy metal ions[188-190]. The large specific surface area (399.7 $m^2\ g^{-1}$) of protonated titanate nanotubes provides sites for immobilization of PVM, allowing an augmentation of typically low surface area of bulk POMs (> 10 $m^2\ g^{-1}$). The increase in surface area of PVM will enhance its photocatalytic capabilities and the anionic nature of PVM should foster adsorption or pre-association for degradation of cationic dyes like methylene blue (MB). With the rational design of PVM immobilized on

P-TNT for attainment of heterogenization and high surface area, the effective application of the as-prepared material as a photocatalyst and parameters influencing the efficiency will be studied. The surface chemistry and mechanism for degradation will then be investigated. Methylene blue (MB) was selected as the model pollutant considering that dyes are extensively used in various industries and are one of the main contributors to water pollution[191].

4.2. Materials and methods

All chemicals used in this study were of reagent grade and were used without further purification. The chemicals used were titanium dioxide (TiO_2, Degussa), sodium hydroxide (NaOH, Schedelco), nitric acid (HNO_3, Honeywell), (3-aminopropyl) triethoxysilane ($H_2N(CH_2)_3Si(OC_2H_5)_3$, Sigma-Aldrich), anhydrous toluene (C_7H_8, Sigma-Aldrich) and hydrogen peroxide (H_2O_2, VRW). All dyes used (i.e. reactive black 5, methylene blue, rhodamine B, methyl orange and acid orange 7) were of reagent grade and used without further purification. 0.1 M HCl was used to adjust the pH of solutions. All solutions were prepared using MiliQ water (18.2 MΩ cm^{-1}).

4.2.1. Synthesis of P-TNT

2 g of Degussa P25 TiO_2 was slowly added to NaOH (10 M, 75 mL) with stirring. The mixture was charged into a 125 mL Teflon and sealed into a stainless-steel autoclave assembly. The mixture was placed in an oven at 130°C for 48 hours and allowed to cool to room temperature. The gel like mixture was washed with deionized water until it reaches pH 8. Proton-exchange reaction was then carried out using 0.1 M nitric acid three times to obtain protonated titanate nanotubes.

4.2.2. Synthesis of $H_5[PV_2Mo_{10}O_{40}]\cdot 32H_2O$

The synthesis of $H_5[PV_2Mo_{10}O_{40}]\cdot 32H_2O$ was prepared according to literature method[152] and as described in chapter 3.2.3.

4.2.3. Surface modification of P-TNT with (3-aminopropyl)triethoxysilane (S-TNT)

0.6 g of P-TNT was dispersed in 30 mL containing varying amounts of (3-aminopropyl) triethoxysilane (2%, 5% and 10% v/v%) was sonicated for 1 hour and then stirred for 24 h. The mixture was centrifuged and washed with 30 mL ethanol for 3 times. It is finally dried in a vacuum oven at 60°C for 24h before further modifications were made. The products are henceforth known as X%S-TNT (where X = 2, 5 and 10).

4.2.4. Modification of X%S-TNT with $H_5[PV_2Mo_{10}O_{40}]$

The as prepared X%S-TNT was added to 250 mL of deionized water and dispersed by sonication for 1 h. 0.3 g of $H_5[PV_2Mo_{10}O_{40}]$ was dissolved into deionized water and added to the X%S-TNT dispersion and sonicated for another 1 h. The mixture was then allowed to rest for 24 h, centrifuged and washed with copious amount of water to removed excess $H_5[PV_2Mo_{10}O_{40}]$ before being dried in a vacuum oven at 60°C for 24 h before it is used for further characterization and application studies. The PVMA-2 modified products are henceforth known as PVM-X%S-TNT (where X = 2, 5, 10).

4.2.5. Material Characterization

All the structures of the materials prepared in this study were characterized using an X-ray diffractometer, the morphology of the PVM-X%S-TNT was investigated using a field emission scanning electron microscope and the local structure of the material was investigated using a transmission electron microscope with specifications as mentioned in chapter 3.2.7. Fourier transform infrared spectroscopy (Perkin Elmer FTIR- Frontier) was used to characterize and verify the presence of $[PV_2Mo_{10}O_{40}]$ on the surface of the titanate nanotubes. Nitrogen adsorption/desorption isotherms were measured at 77 K with Quantachrome Quadrasorb SI. X-ray photoelectron spectroscopy (XPS) studies were conducted using a Kratos Axis Supra spectrophotometer with dual anode monochromatic $K\alpha$ source to determine the composition of the samples. All binding energy for elements of interest were corrected against an adventitious carbon C 1s core level at 284.8 eV. All

XPS peaks were fitted using Shirley background together with Gaussian-Lorentzian function using CASA XPS software. The diffuse-reflectance spectra of the as prepared material were measured using a UV-Vis spectrophotometer (Shidmadzu UV-2800) from 250 – 800 nm against a $BaSO_4$ standard.

4.2.6. Photocatalytic studies of PVM-x%s-TNT

In a typical study, a 50 mL solution of 5 g L^{-1} methylene blue (MB) with pH adjusted to pH 2 was placed in a beaker acting as the reactor. The solution was then added with H_2O_2 and a desired amount of catalyst. Thereafter, the visible light photo-Fenton oxidation experiment was performed using visible light (420 – 630 nm) using a solar simulator (Newport, 150 W Xenon arc lamp, 1 sun, polycarbonate filter for UV cut-off). 1.5 mL aliquots were drawn at regular interval and filtered using PTFE syringe filter (0.45 μm) before being analysed using a UV-Vis spectrophotometer (Shimadzu UV-1800). The concentration of the dye was determined using Beer-Lambert's Law.

$$A = \varepsilon\, l\, c$$

Where A is the absorbance, ε is the molar absorptivity coefficient, l is the path length of the light and c is the concentration. The supernatant was collected after reaction and analysed by inductively coupled plasma-optical emission spectroscopy (ICP-OES, Perkin Elmer Optima 2000DV) for dissolved metals.

4.3. Results and Discussion

4.3.1. Material Characterization

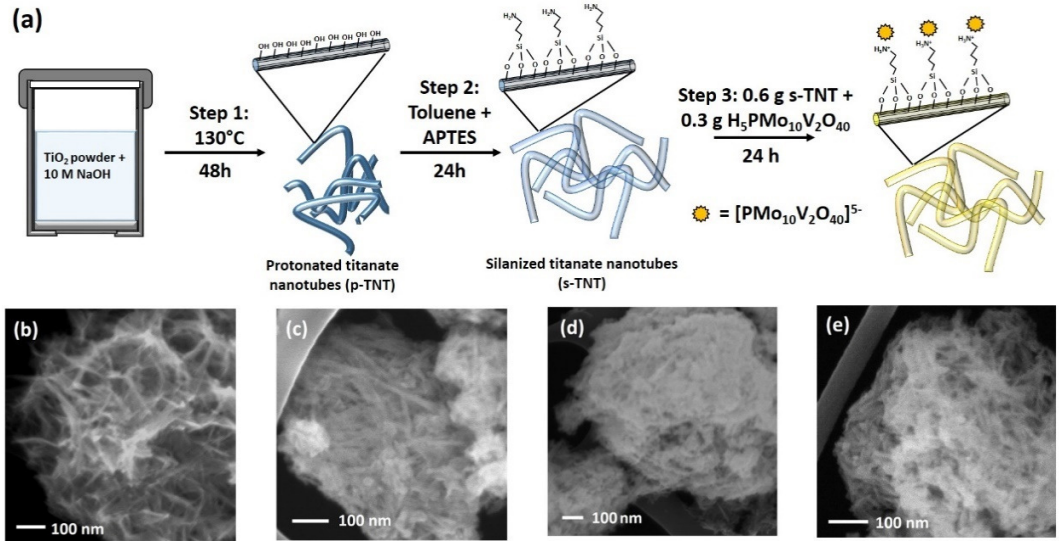

Figure 4.1 *(a) Schematic of P-TNT preparation and surface modification with POMs, SEM micrograph of (b) P-TNT, (c) PVM-2%S-TNT, (d) PVM-5%S-TNT and (e) PVM-10%S-TNT.*

Figure 4.1 (a) above shows the schematic for the preparation, surface modification and attachment of PVM on the as-prepared P-TNT. Synthesis of the P-TNT lays the foundation for this study as it is being employed as the base support for the polyoxometalates to be immobilised. The preparation of P-TNT with a high level of dispersion is therefore highly crucial for the steps to follow in order to obtain effective surface modification. The surface silanization to incorporate amine functional groups on the P-TNT was chosen as the modification approach since amines are able to form stronger ionic interaction and the organic nature of the linker will provide better resistance against loss of PVM by introducing a small degree of hydrophobicity. During the process of modification with PVM, it was observed that the intense colour of the PVM diminishes over time. Therefore, the influence of degree of surface amination towards the immobilization of PVM on the P-TNT surface was studied in greater detail within this chapter. After the immersion of the aminated P-TNT in PVM solution, the modified material was washed with copious amounts of water to remove excess polyoxometalates which are loosely attached.

Figure. 4.1(b), (c), (d) and (e) show the SEM micrograph of P-TNT, PVM-2%S-TNT, PVM-5%S-TNT and PVM-10%S-TNT. The unmodified P-TNT resembles thin threads loosely placed together, while the post modified material appears to be agglomerated. This is likely due to cross-linking between silanol groups during the APTES surface silanization process, which has been reportedly observed in silanized nanoparticles[192,193]. FTIR spectroscopy is thus used as a primary characterization technique to elucidate the successful modification of the P-TNT and the occurrence of the cross-linking process.

Figure. 4.2(a) shows the spectra of $H_5[PV_2Mo_{10}O_{40}]$, where the bands are 1060, 960, 863 and 776 cm^{-1} are characteristics of P–O stretching, terminal M=O stretching, $M–O_c–M$ stretching of corner-sharing and edge-sharing $M–O_e–M$ MO_6 octahedra respectively (where M = Mo or V). The spectra of P-TNT (Figure. 4.2(b)) does not show any distinctive feature in the region of 1200 – 700 cm^{-1}, therefore the FTIR spectra of the modified PVM-X%S-TNT in figure 4.2 (c-e) are indicative of the effective surface modification performed. For all the PVM-X%S-TNT prepared, a weak band observed at 1051 cm^{-1} indicates the successful formation of Ti-O-Si bond; while the band at *ca.* 1126 cm^{-1} likely arises due to the formation of cross-linking between silanol groups (*i.e.* formation of Si-O-Si bonds) during the silanization process. The Si-C bond stretching at *ca* 1226 cm^{-1} and N-H bending at *ca.* 1506 cm^{-1} provides further evidence of the surface modification by APTES. For both $M–O_c–M$ and $M–O_e–M$ in the PVM modified materials, the characteristic bands undergo a blue shift to 906 and 797 cm^{-1} which indicates the attachment of $[PV_2Mo_{10}O_{40}]^{5-}$ with the amine groups on the surface of the X%S-TNT.

The STEM dark field images of P-TNT and PVM-X%S-TNT are presented in figure 4.3. The images show that the as prepared P-TNT has a diameter of ~10 nm. It can be seen in figure 4.3(a) that the P-TNT prepared has a cylindrical shape with hollow cavity running through its length. This is an important feature which provides a large surface area for the surface silanization and functionalization with amine groups, assisting in the immobilization of the PVM thereafter. While the PVMs are not observable due its size, there are observable changes in the secondary structure of the material as seen in figure

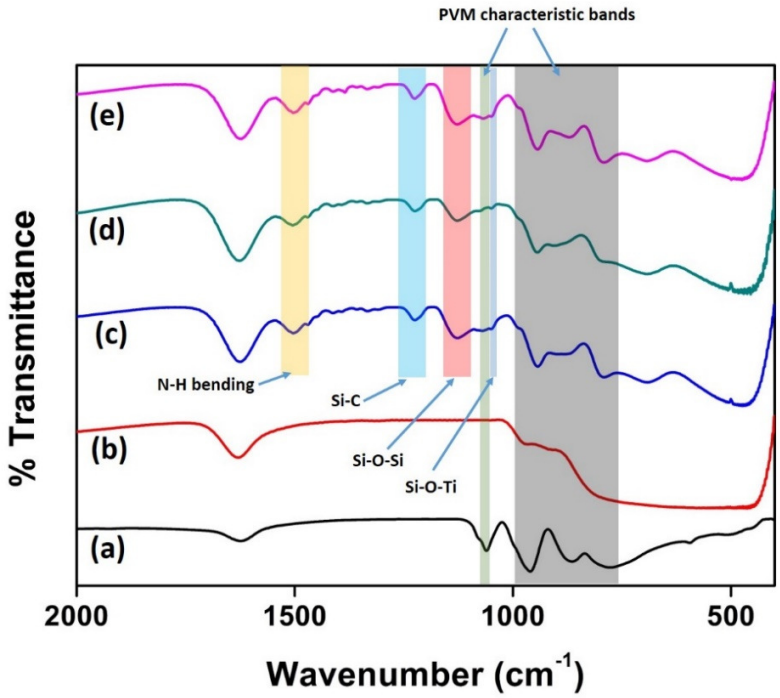

Figure 4.2 FTIR spectra of (a) $H_5[PV_2Mo_{10}O_{40}]$, (b) P-TNT, (c) PVM-2%S-TNT, (d) PVM-5%S-TNT and (e) PVM-10%S-TNT.

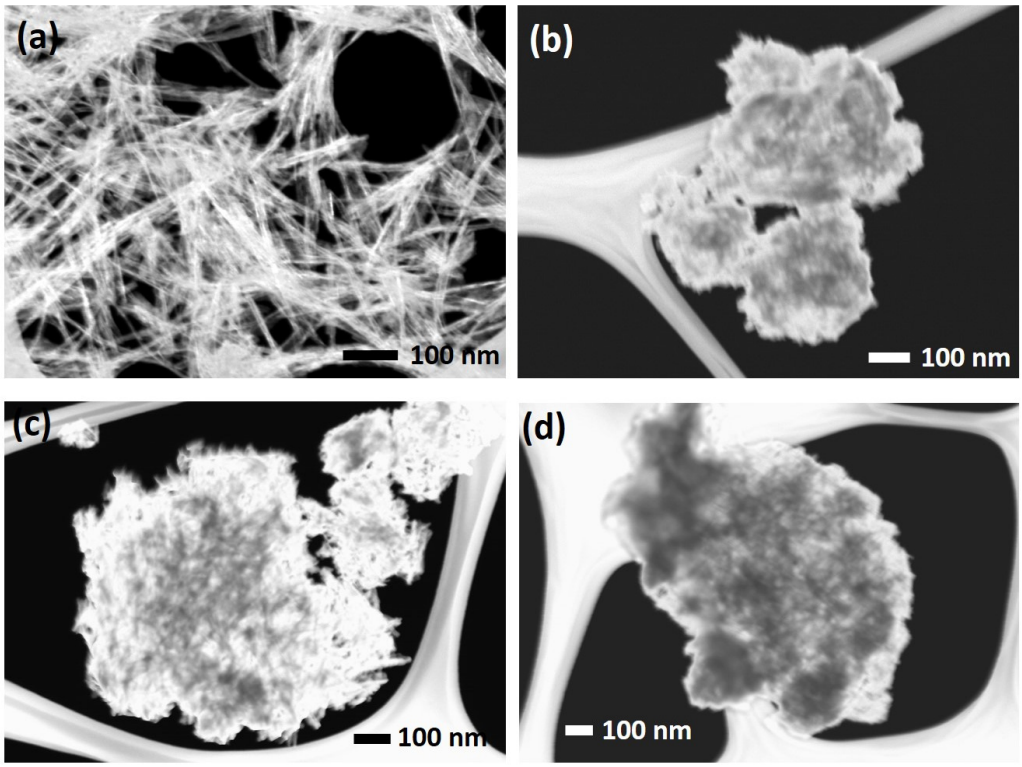

Figure 4.3 FESEM Dark Field micrograph of (a) P-TNT, (b) PVM-2%S-TNT, (c) PVM-5%S-TNT and (d) PVM-10%S-TNT.

4.3 (b) – (d). The primary reason for the formation of agglomerated secondary structure is most likely due to the cross-linking of surface silanol groups on the nanotubes. Since PVM has an anionic charge of 5-, it is also capable of formation of ionic interaction with (1) the amine groups on a single nanotube and (2) the amine groups between multiple nanotubes. Dark field images were taken to identify the presence of PVM phases growing on the surface of the P-TNT. The interaction of PVM is electrostatic due to transfer of proton to the amine sites on the surface modified P-TNT.

$$TiO_2\text{–}APTES + H_5[PV_2Mo_{10}O_{40}] \rightarrow (TiO_2\text{–}APTES^+)(H_4[PV_2Mo_{10}O_{40}]^-) \quad (4.1)$$

$$(TiO_2\text{–}APTES)_2 + H_5[PV_2Mo_{10}O_{40}] \rightarrow (TiO_2\text{–}APTES^+)_2(H_4[PV_2Mo_{10}O_{40}]^{2-}) \quad (4.2)$$

$$(TiO_2\text{–}APTES)_n + H_5[PV_2Mo_{10}O_{40}] \rightarrow (TiO_2\text{–}APTES^+)_n(H_{(5-n)}[PV_2Mo_{10}O_{40}]^{n-}) \quad (4.3)$$

From the comparison of figure 4.3(b), (c) and (d), it can be see that PVM-5%S-TNT has the PVM most evenly distributed on the surface as can be seen with the bright contrast on most areas of the surface. The poorer distribution of PVM in figure 4.3(b) could be due to lower coverage of surface amine groups on the titanate nanotube surface in PVM-2%S-TNT. In PVM-10%S-TNT, has only small regions on the surface with relatively higher PVM immobilization which is likely a drawback caused by the excessive use of APTES for surface amination.

To understand the composition of the material prepared, X-ray photoelectron spectroscopy (XPS) analysis was performed on the modified samples. From the values in Table 4.1, the composition of the material can be approximated, with calculations indicating approximately 25.1, 20.9 and 30.2% PVM loading by mass in the 2, 5, and 10%

Table 4.1 Elemental analysis data of PVM modified material by XPS

Catalyst	**Elemental analysis wt%**						
	Ti	Si	N	O	P	Mo	V
PVM-2%S-TNT	28.97	6.77	8.42	40.03	0.47	13.91	1.43
PVM-5%S-TNT	29.57	5.36	7.66	44.24	0.38	11.55	1.23
PVM-10%S-TNT	25.08	6.04	10.61	39.26	0.46	17.52	1.04

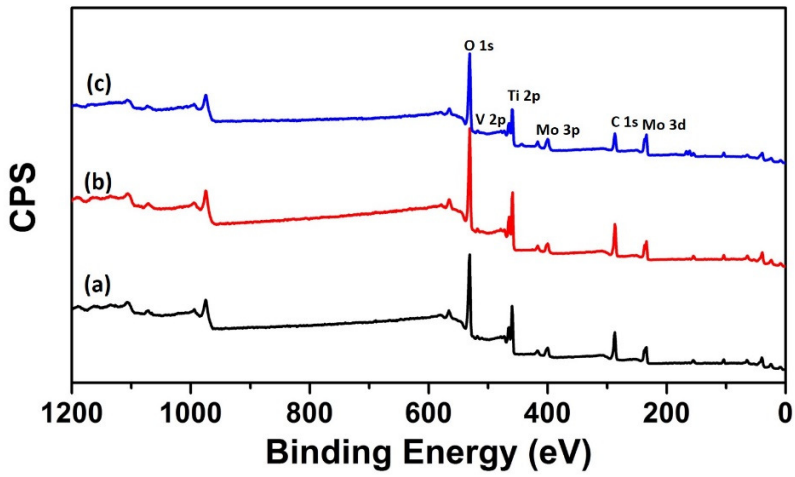

Figure 4.4 XPS spectra of (a) PVM-2%S-TNT, (b) PVM-5%S-TNT and (c) PVM-10%S-TNT.

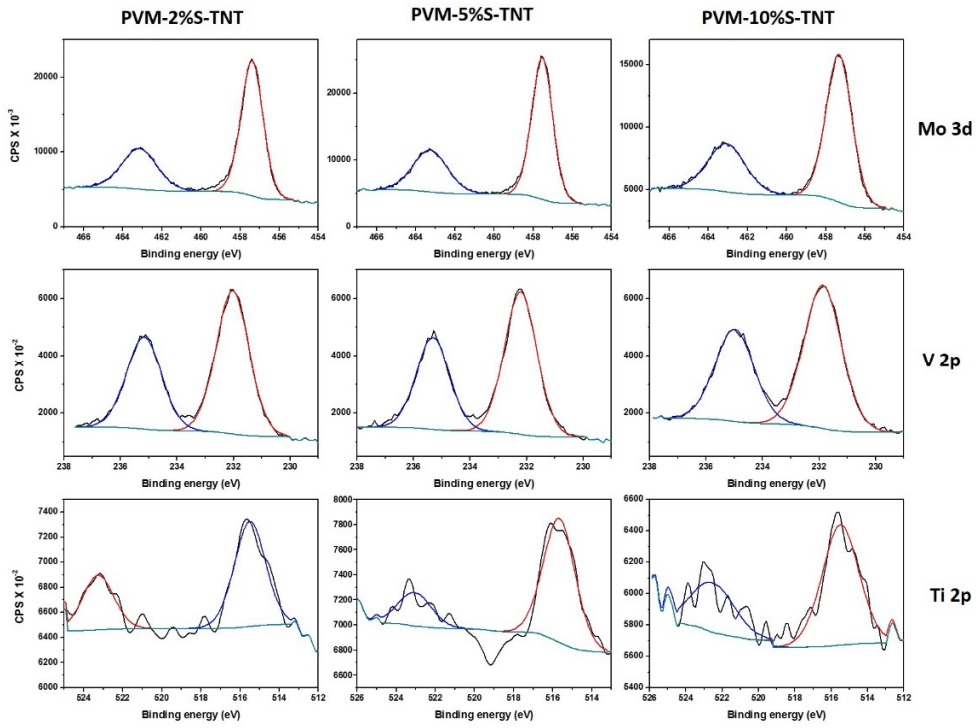

Figure 4.5 XPS spectra of Mo 3d5/2, V 2p and Ti 2p of PVM modified materials.

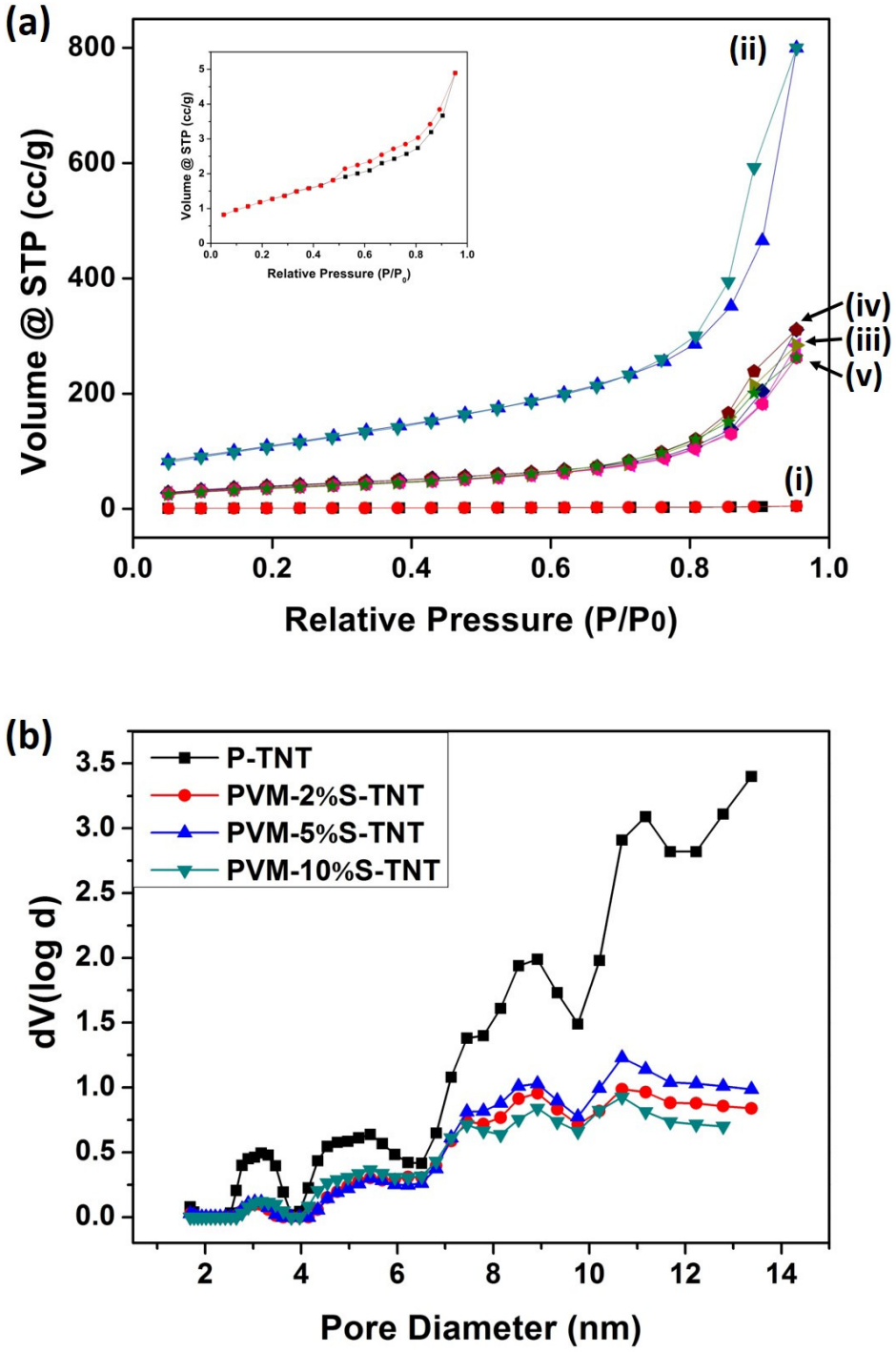

Figure 4.6 N_2 adsorption desorption isotherm of (a)(i) $H_5[PV_2Mo_{10}O_{40}]$, (ii) P-TNT, (iii) PVM-2%S-TNT, (iv) PVM-5%S-TNT and (v) PVM-10%S-TNT. (b) Pore size distribution of P-TNT and PVM-5%S-TNT.

samples respectively. The results here shows that the increase in amount of coupling agent used does not form a direct relation with the amount of PVM immobilized on the surface. This suggests that fine control in the degree of surface medication is required to obtain desired quantity of PVM immobilization. It can be seen from Figure 4.4 that the spectra of the 3 samples are largely similar, with the peaks of the main elements present labelled and Figure 4.5 shows the spectra of Mo 3d, V 2p and Ti 2p in the PVM modified materials. The peak position of Mo $3d_{5/2}$ for the modified samples are approximately 232.2 eV, which is a slight shift from literature value of 233.2 eV[194]. The fitting of the XPS peaks for all modified material shows the presence of mainly Mo^{6+} oxidation state. The fitting of peak for V 2p shows a single oxidation state V^{5+}, indicating that the oxidation state of vanadium is unaffected by the modification process. While peaks of TiO_2 shows a doublet signal of Ti 2p at 457.4 and 463.3 eV, which is a slight shift from literature values of 459.7 and 464.6 eV[195] and can be attributed to effects of surface modification on the TNT.

Figure 4.6 (a) shows the nitrogen adsorption/desorption isotherm of the PVM, P-TNT and PVM-X%S-TNT series. The low surface area and high solubility of the acid form of PVM are the main obstacles in application towards heterogeneous catalysis. The surface area of PVM is 4.2 m^2 g^{-1} and the nitrogen desorption isotherm (Figure 4.6(a)(i)) can be clearly seen in the inset within Figure 4.6(a). The P-TNT prepared shows a specific surface area of 399.7 m^2 g^{-1} (Figure 4.6(a)(ii)) with Type IV isotherm with a characteristic hysteresis loop associated with the occurrence of pore condensation. The decrease in specific surface area of the modified materials is an indicator of the successful modification performed. From the results, PVM-5%S-TNT has the highest specific surface area after the immobilization. This can be attributed to the fact the even though the surface was modified with 5% APTES mixture, only 20.9% mass of the material was contributed by PVM. The lower degree of immobilization therefore provided the material with higher specific surface area.

Table 4.2 Structural properties of P-TNT and PVM-X%S-TNT (X = 2, 5, 10) characterized by N_2 adsorption.

Material	S_{BET} (m^2 g^{-1})	S_{pore} (m^2 g^{-1})	V_{pore} (cc g^{-1})	D_{DFT} (nm)
P-TNT	399.7	292.7	0.84	13.4
PVM-2%S-TNT	133.6	99.4	0.31	10.7
PVM-5%S-TNT	143.4	105.0	0.34	10.7
PVM-10%S-TNT	128.6	96.5	0.28	10.7

Table 4.2 summarizes the BET specific surface area of P-TNT and PVM modified P-TNT. The immobilization of PVM on the P-TNT therefore increases the accessibility of PVM as active sites for catalysis by providing a tremendous increase in the surface area of the modified material. Even with the formation of the secondary structure due to agglomeration of the nanotubes as seen in the SEM micrographs presented above, the modified materials still possess relatively high surface area.

In order to understand the influence of the modification along the cylindrical pores of the nanotube, pore size distribution was calculated based on N_2 at 77 K on carbon (slit pores, Non-Local Density Functional Theory equilibrium model) calculation model, as the calculation results showed the best fit and correlation with the observation made[196,197]. Figure 4.6(b) shows the pore size distribution and the calculated results of specific pore surface area, specific pore volume and mode pore diameter are summarized in Table 2. From the calculations, the materials modified with PVM experience a 2.7 nm decrease in mode pore diameter and a significant decrease in specific pore surface area and specific pore volume. This change is in agreement with the physical dimensions of PVM anions which has a *ca.* 1.0 nm diameter and indicates that the pores have been successfully modified and immobilized with PVM.

X-ray diffraction was carried out to further characterize the crystal structure of the materials at the various stages of preparation. The reflection peaks of $H_5[PV_2Mo_{10}O_{40}]\cdot 36H_2O$ are in good agreement with the tetragonal crystal structure (PDF# 04-015-6856). Figure 5.7 (a) shows the most intense reflection peaks at $2\theta = 8.4°$

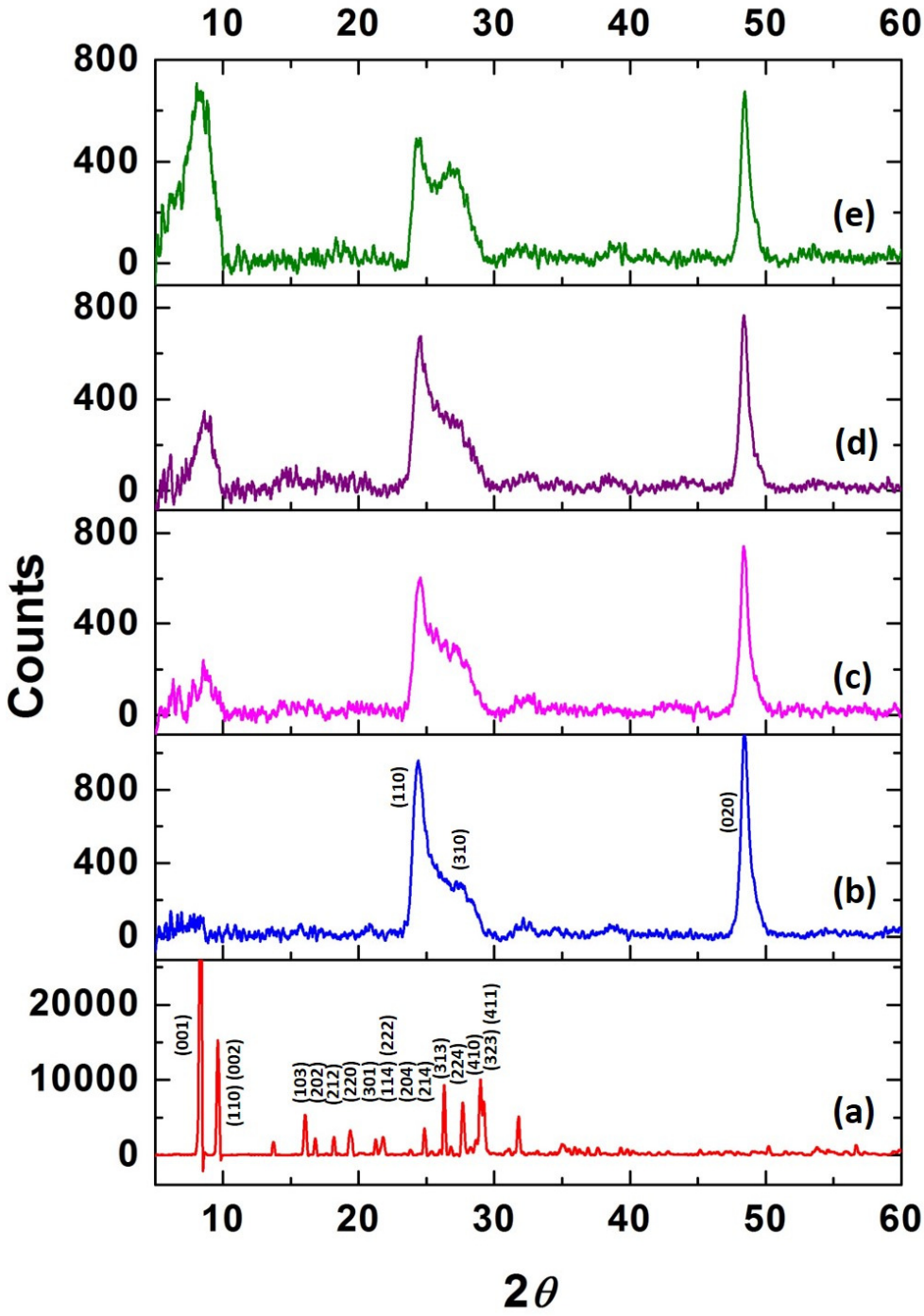

Figure 4.7 XRD diffractogram of (a) $H_5[PV_2Mo_{10}O_{40}]$, (b) P-TNT, (c) PVM-2%S-TNT, (d) PVM-5%S-TNT and (e) PVM-10%S-TNT.

and 9.6° corresponds to (101) and (002) (110) (note: doubly indexed reflection) are characteristics indicators of the secondary crystalline structure of the polyoxometalates,which arises from the presence of water of crystallization in its highly hydrated state. The peaks of medium intensity between 15 - 35° 2θ are characteristics of the Keggin anion (Figure 5.7 (a)). Broad peaks were observed for P-TNT corresponds with (110), (310) and (020) planes of orthorhombic $H_2Ti_2O_5 \cdot H_2O$ (PDF No. 00-047-0124) positioned at 2θ = 24.6°, 28.5° and 48.3° (Figure 4.7 (b)). The broadening of the reflection peaks is an indicator of the highly defined nano-tubular structure of the P-TNT prepared. To further probe the growth of PVM on the surface of P-TNT, the XRD of PVM-X%S-TNT (X = 2, 5, 10) were taken and presented in Figure 4.7 (c), (d) and (e). While the reflection peak of the nanotubes at 48.3° 2θ remains consistent throughout, an increase in the intensity of the peak at 28.5° 2θ indicates the presence of PVM due to the convolution of the characteristic medium intensity reflection peaks of the Keggin anion. This is accompanied by the appearance of the broad peak centred at ~9° 2θ which is a convoluted peak of (001), (010) and (100) planes of a triclinic PVM (PDF# 01-084-4215) due to the absence of most of the water of crystalisation. The peak intensity increases with higher degree of surface amination, which is perceived to be due to more extensive growth sites for the growth and support of the polyoxometalates on the P-TNT surface.

Figure 4.8 shows the TEM micrograph of P-TNT and the PVM-X%S-TNT. Figure 4.8 (a) shows that the P-TNT prepared have a uniform tubular morphology. Figure 4.8 (b) shows a high magnification image of the P-TNT where the (110) plane with *d*-spacing of 0.36 nm can be observed. In all the modified samples, we can see that the nanotubes are agglomerated forming cluster of randomly arranged tubes (Figure. 4.8 (c), (e) and (g)), while the high magnification images show particles *ca.* 1 nm in size which corresponds to the typical size of PVM, indicating the successful modification of the P-TNT surface.

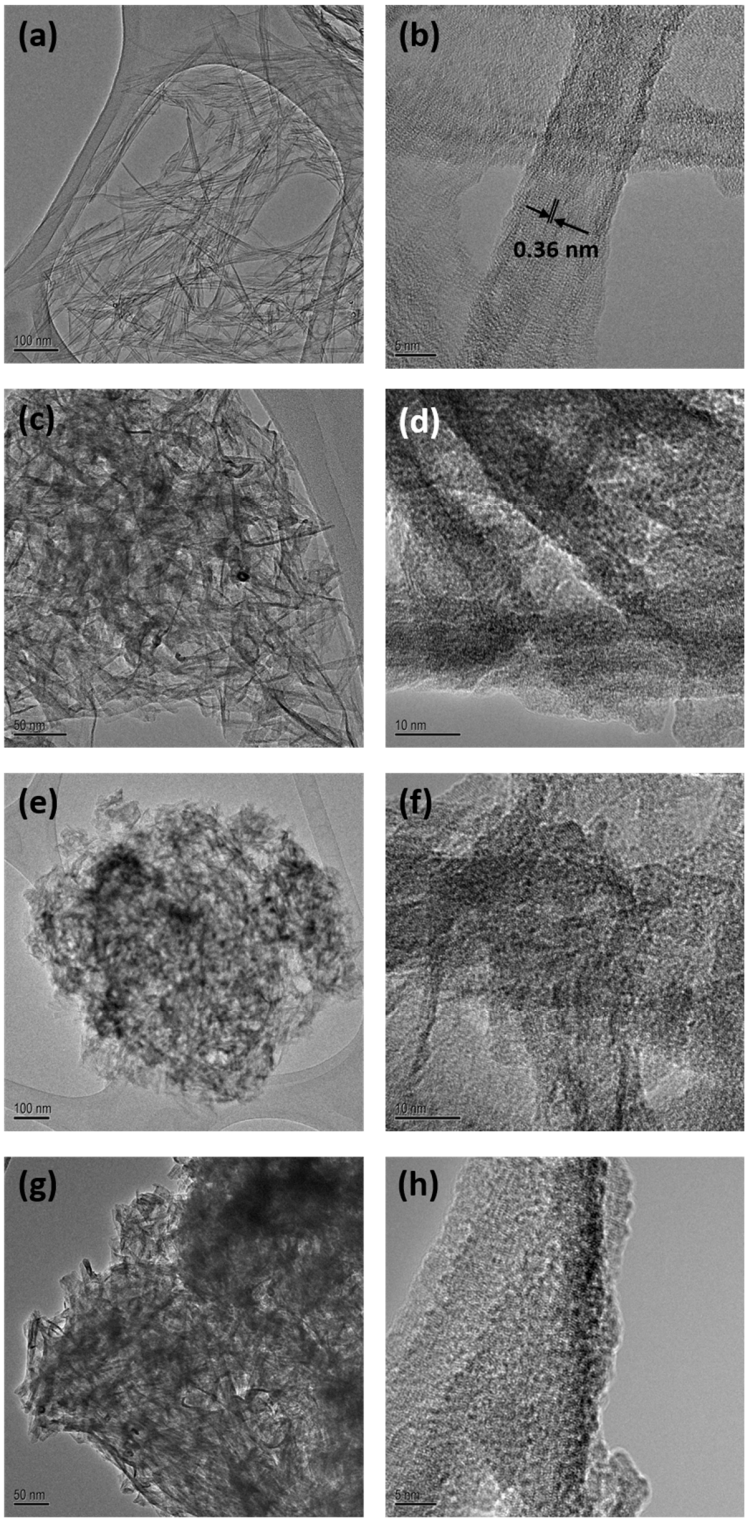

Figure 4.8 HRTEM micrograph showing the local structure of P-TNT (a) low magnification, (b) high magnification; PVM-2%S-TNT (c) low magnification, (d) high magnification; PVM-5%S-TNT (e) low magnification, (f) high magnification; PVM-10%S-TNT (g) low magnification, (h) high magnification.

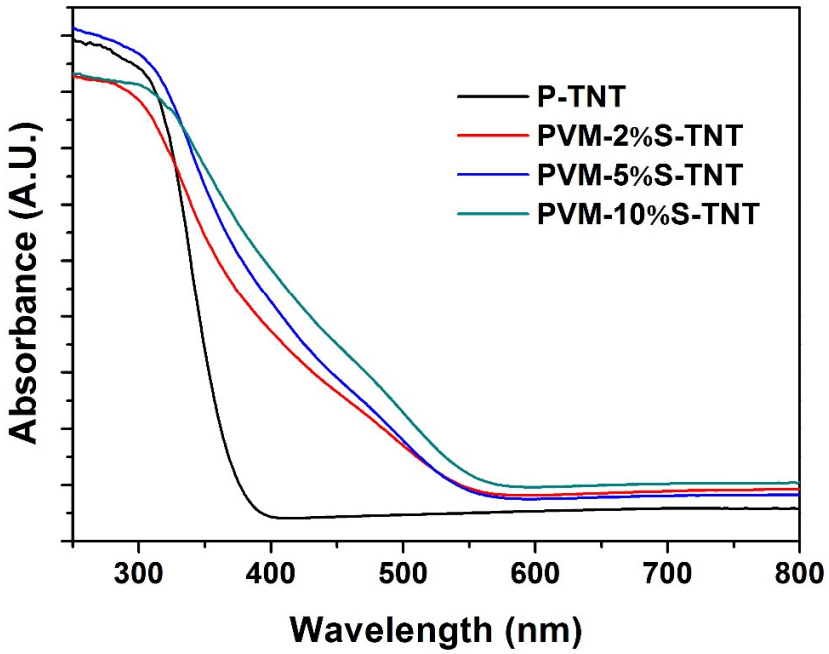

Figure 4.9 UV-Vis spectra of as prepared P-TNT and PVM-X%S-TNT (X= 2, 5, 10).

With the motivation to use the PVM immobilized materials as a photocatalyst, the photophysical properties was determined by UV-vis adsorption measurement of the powder samples as shown in Figure 4.9. The strong adsorption of P-TNT below 400 nm is mainly associated with the optical bandgap of titanate materials. The immobilization of PVM onto the surface of P-TNT therefore incorporates the photocatalytic capabilities of PVM allowing it to be used as a heterogeneous photocatalyst. It can be seen from Figure 4.9 that the adsorption capabilities of the as prepared materials have extended to the visible light region of the spectrum.

4.3.2. Photocatalytic degradation of organic dye by PVM-X%S-TNT

In this study, methylene blue was chosen as the organic waste target for primary study. The successful application of PVM-X%S-TNT is dependent on its ability synergistically adsorb and photocatalytically mineralize organic pollutants. In all studies performed, the pH of the solution was adjusted to ~pH 2, so as to avoid hydrolytic degradation of PVM [34]. To investigate the photocatalytic performance of the as-prepared material, MB solution with a specified dose of PVM-X%S-TNT was illuminated under simulated visible light. Figure. 4.10 (a) shows the photocatalytic removal of MB from the solution with PVM-X%S-TNT. The inset in figure 4.10(a) shows adsorption properties of the as prepared PVM-X%S-TNT (X = 2, 5, 10).

In this study, a starting concentration of 5 mg L^{-1} MB was used. In all three samples prepared, a steady state adsorption is achieved by approximately 30 min and PVM-5%S-TNT is shown to have better adsorption as compared to the others in the series. In a previous study by Tang et. al [198], it was shown that P-TNT based Ag-AgCl-TNT showed superior adsorption and photocatalytic degradation of 50 mg L^{-1} MB. However, due to the surface modification of the P-TNT which altered its highly adsorptive nature, the P- TNT is acting as a support material for the immobilization of PVM. Based on consideration of low initial MB concentration used in this study which does not detrimentally affect the transmittance of light source to the catalyst in the reactor, adsorption and photocatalytic degradation was carried out synergistically without prior achievement of adsorption equilibration.

It can be seen in figure 4.10 (a) that all the as-prepared materials show moderate removal of MB under visible light irradiation in the order of: PVM-10%S-TNT < PVM-2%S-TNT < PVM-5%S-TNT. Based on the above results, it is evident that a 5% v/v% of APTES in ethanol produces a surface which is optimal for the immobilization of PVM with the best performance. The surface optimization leads to a higher specific surface area in the final material which likely contributed to better performance during application. The modification provides improved removal and ease of recovering the material at the end of

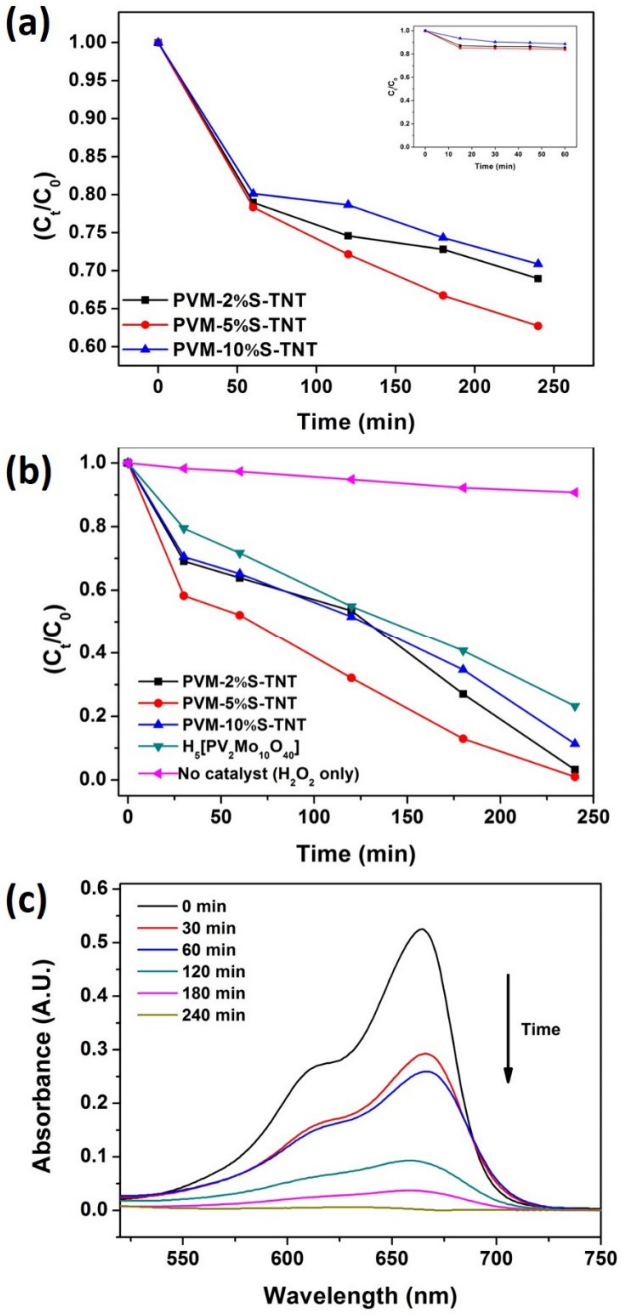

Figure 4.10 Photocatalytic activity of PVM-X%S-TNT (X= 2, 5, 10) under simulated visible light irradiation (Xe arc lamp 150 W, 420-630 nm, intensity 409 W m^{-2}). [MB] = 5 mg L^{-1}, catalyst dosage = 0.4 g L^{-1}, pH = 2 (inset shows adsorption of MB by the materials in 60 min) (b) Photocatalytic activity of PVM-X%S-TNT (X= 2, 5, 10) under simulated visible light irradiation. [MB] = 5 mg L^{-1}, catalyst dosage = 0.4 g L^{-1}, pH = 2, [H_2O_2] = 98 mM. (c) UV-vis spectroscopy of MB showing a decrease in concentration over time.

the reaction as compared with the degradation of MB with PVM under homogeneous condition where recovery of PVM from solution is difficult.

In order to further improve the performance of the material, H_2O_2 was introduced as an oxidant increase the rate of photo-oxidation[199]. The influence of H_2O_2 addition on the degradation of MB was studied and illustrated in figure 4.10 (b). The addition of H_2O_2 enhances the degradation efficiency of MB in all PVM-X%S-TNT materials. PVM-5%S-TNT exhibited the best performance with a 99 % removal of MB within the reaction time of 240 min while PVM only degraded 76.8 % MB under homogeneous conditions. This further insinuates that the 5% APTES modification yields excellent amine functionalization for the attachment of PVM. The role of H_2O_2 during the photocatalytic degradation process is to act as an electron acceptor from the conduction band of PVM to improve charge separation and the formation of $OH^{\bullet}$. The mechanism for generation of $OH^{\bullet}$ is as follows:

$$H_2O_2 + e^- \rightarrow OH^- + OH^{\cdot} \qquad (6.4)$$

Even though H_2O_2 is considered a powerful oxidizing agent, Figure 4.10 (b) shows that the photo-oxidation of MB with H_2O_2 under simulated visible light is limited to approximately 9.3 % over the reaction time studied. Therefore, MB degradation using the as-prepared material can be accelerated and the role of H_2O_2 in the photo-oxidation process can be established. With the establishment of PVM-5%S-TNT being the material with the best performance, further studies were performed to understand parameters influencing its photocatalytic activity. The effect of H_2O_2 concentration was further studied and shown in Figure 4.11 (a). With the usage of 147 mM and 98 mM of H_2O_2, 99 % removal of MB was attained in 240 min. Only 97.5 % removal was achieved when the H_2O_2 concentration was decreased to 48 mM, due to lower $OH^{\bullet}$ formation. When 147 mM of H_2O_2 was used, the initial degradation efficiency of MB was inhibited, this could be due to scavenging of $OH^{\bullet}$ by excess H_2O_2. Figure 4.11 (b) shows the effect of catalyst dosage on the degradation of MB. With the increase in amount of catalyst used, the

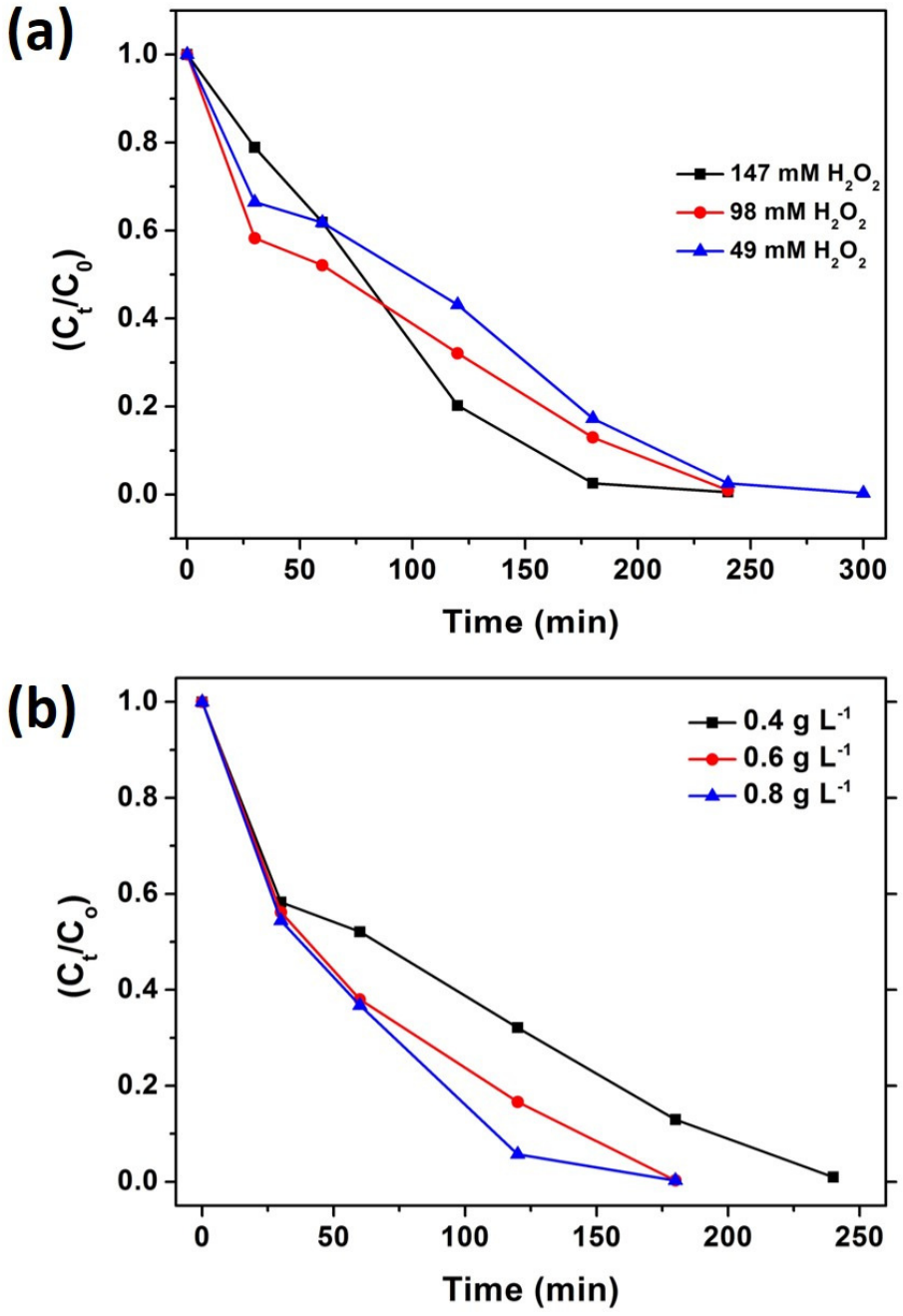

Figure 4.11 Effect of (a) different H_2O_2 concentration. [MB] = 5 mg L^{-1}, catalyst dosage = 0.4 g L^{-1}, pH = 2 and (b) different catalyst loading of PVM-5%S-TNT on the degradation of MB.

amount of active sites available also increases, thus the efficiency of degradation increases. This also allow for a better utilization of H_2O_2 in the reaction, which reduces the effect of H_2O_2 scavenging the $OH^{\bullet}$ formed.

Figure 4.12 (a) shows the influence of pH on the removal of MB. The results show that MB can be removed from the solution within 60 min of reaction time under visible light irradiation. However, the high removal efficiency observed here cannot be ascribed to a complete degradation of MB. In all studies performed at pH 2, the catalyst recovered at the end of the study reverted to the original yellowish colour, while in the case of the recovered catalyst for pH 5 and pH 7, the colour were purplish as seen in the inset in

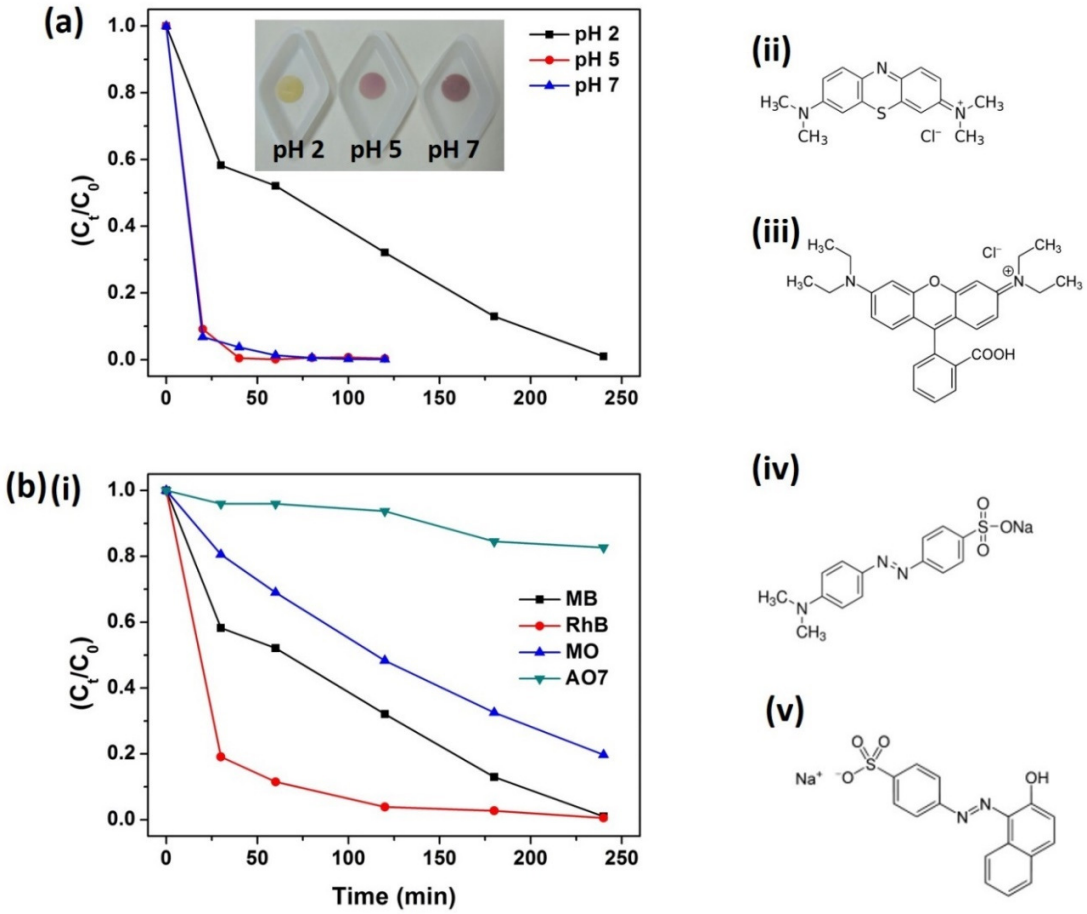

Figure 4.12 (a) Effect of pH on degradation of MB (inset shows colour of catalyst recovered), (b)(i) Degradation of different dye using PVM-5%S-TNT, structure of (ii) methylene blue, (iii) rhodamine B, (iv) methyl orange and (v) acid orange 7.

figure 4.12 (a), which indicates an adsorption of partially degraded MB on the surface of the catalyst and is detrimental to the reusability of the catalyst. Firstly, at higher pH, the lower stability of H_2O_2 leads to increase decomposition to H_2O and O_2, which reduces the $OH^{\bullet}$ formation and the degradation of MB. Secondly, the occurrence of such phenomenon can be due to the change in the surface chemistry of the material with an increase in pH, which increases the adsorption of MB blue, which is a cationic dye, onto the anionic surface formed by PVM on the catalyst surface. As seen in equation 4.3, acid sites on PVM may remain due to varying degree of attachment to the amine surface. The increases in pH causes the deprotonation of PVM on the catalyst surface leading to formation of negatively charged sites. The altered surface chemistry of the catalyst may encourage strong electrostatic attachment with the dye molecules, which prevents the effective degradation of MB. Moreover, the supernatant collected post reaction was tested using ICP-OES, which indicates 4.4 mg L^{-1} and 3.7 mg L^{-1} of vanadium in the solution. This is attributed to the instability of PVM, which under higher pH is hydrolysed and leachate into the solution[200]. Under the condition of pH 2, the leaching of vanadium into the supernatant is only 0.8 mg L^{-1}. The catalyst can be recovered by filtration and recycled by washing with deionized water and drying at 60°C for 3 hours before being reused. Results shows that the catalyst was reusable for at least 3 cycles with consistent removal rates of 99% under pH 2 conditions.

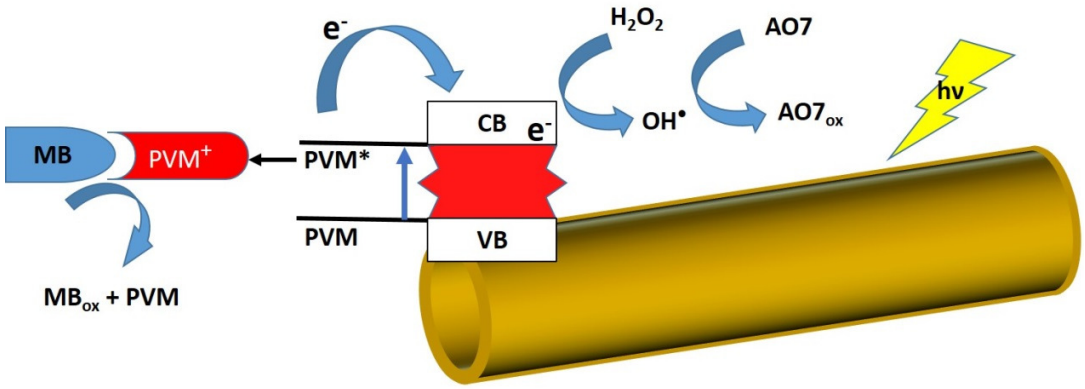

Figure 4.13 Suggested mechanism for photocatalytic activity of PVM-X%S-TNT under visible light irradiation.

Figure 4.12 (b) shows the photocatalytic degradation of methylene blue, rhodamine B, methyl orange and acid orange 7 with PVM-5%S-TNT as the catalyst. From the figure, MB and RhB can be effectively degraded by the catalyst in 240 min, while only 80.3 % removal was achieved for methyl orange. Furthermore, AO7 only underwent incipient degradation of 17.3 % under the same conditions. The above results primarily indicate that the catalyst is able to degrade cationic dyes efficiently, and has meagre effect in the degradation of an anionic dye like acid orange 7. Methyl orange while being anionic in its sodium salt form acquires cationic charge under low pH conditions, thus facilitating its removal under conditions used in this study. The above results led to the derivation of certain mechanistic insights on the photocatalytic degradation process as summarized in Figure 4.13.

The catalyst surface made up of PVM anions carries negative charge which attracts in the cationic dye molecules *via* electrostatic attraction allowing the reaction to take place through bulk type II catalysis. Crystalline phase of PVM on the surface of the TNT which are photo-excited can directly oxidize the dye by the hole (h^+). The photo-produced hole may also react with water, to produce $OH^\bullet$ which can attack the organic dye. The reduced PVM can then be oxidized by H_2O_2, leading to the formation of $OH^\bullet$ which can propagate to attack the dye molecules for further degradation reaction. PVM has a lower conduction band and a higher valence band than TiO_2, which does not allow TiO_2 to participate in the electron hole pair separation process [33]. In the case of anionic dye like AO7, the pre-association step is not favoured due to charge repulsion with the catalyst surface. The limited removal of AO7 observed in figure 4.12(b)(i) could be due to $OH^\bullet$ formation largely bound to the "surface" of the catalyst. The radical formed here is unlikely to escape to the bulk solution due to the short lifetime of $OH^\bullet$, thus limiting the degradation of AO7 through this pathway.

4.4. Conclusion

In this chapter, PVM immobilized on TNT surface was characterized and the catalytic properties was studied. The degree of surface modification with APTES was established

as a factor influencing the effectiveness of the material as a photocatalyst. The process provided surface amine groups on the TNT for immobilization of PVM. This increases the specific surface area of PVM as compared to the bulk crystal and also heterogenised PVM for ease of recovery after catalytic application. The design and engineering of the material allow the study of the photocatalytic properties and parameters independently, since TNT theoretically plays the role of an inert support during photocatalysis using visible light. Strategies to improve the visible light adsorption properties via the incorporation of plasmonic metal nanoparticles should be considered in future work. This will provide improve efficiency and reduce the use of H_2O_2 with the use of the catalyst.

Chapter 5

Phosphovanadomolybdate-based surfactant encapsulated heteropolyanion with multi-lamellar nano-structure for catalytic wet air oxidation of organic pollutant under ambient conditions

A series of surfactant encapsulated heteropolyanion (SEH-n) based on $H_{(3+n)}[PV_nMo_{(12-n)}O_{40}]$ (PVMAs) was prepared. The morphological optimisation of the SEHs was studied by the control of solvent polarity and PVMA to surfactant ratio used. Investigation by TEM revealed the formation of particles with multi-lamellar nano-structure in the SEHs. Characterization of the SEHs by XRD, TGA and FTIR indicated the successful encapsulation of the $[PV_nMo_{(12-n)}O_{40}]^{(3+n)-}$ with the surfactant. The performance of SEHs as catalysts for the removal of bisphenol–A under ambient conditions was evaluated. Factors influencing the performance of the SEH–n are the relative stability of the Keggin structure and electron accepting property. The dissolved oxygen plays a crucial role in improving the BPA removal efficiency. The hydrophobic property of the nano–sized SEHs provides good aqueous stability and allows excellent recoverability of the catalyst from the aqueous solution after treatment.

5.1. Introduction

The design and development of advanced functional materials is an area of growing interest in the last few decades. Such research will bring the advancement to the applications of these materials in material science and catalysis.[26] One of the key steps towards the realization of this development is the controlled self-assembly of nano-building blocks into functional assemblies which is technically challenging.[130] Polyoxometalates (POMs) is a type of molecular transition metal oxide gaining research interest in the preparation of advanced functional assemblies. They are oxoanionic cluster made up of early transition metals in their highest oxidation state i.e. tungsten, molybdenum and vanadium. POMs have attracted much research interest and have been applied in areas such as materials, catalysis, biomedicine, energy and environmental studies.[24,84,201-203] Amongst the chemical and physical properties of POMs, the redox and semiconductor like properties[33] are some of the main driving forces for the active research on this material. The use of POM in both aqueous and organic media under homogeneous condition for fine organic synthesis[22,57,204] and their potential in the mineralization of organic compounds are well-documented.[38,205,206] However, homogeneous catalysis using POM is an obstacle to effective application difficulty due to difficulty in catalyst recovery.

The most commonly studied POM is the heteropolyacid (HPA) best represented by the Keggin structure. HPA typically have low surface area and high solubility in water which hinders the recoverability and effective use as catalytic materials in aqueous media.[3] In chapter 4, a nano-architectural design by amine-functionalization of titanate nanotubes followed by immobilization of the HPA was used as a strategy to achieve heterogeneity of the HPAs and facilitate their recoverability from aqueous solution. Another method employs organic cations to form organic–inorganic hybrids presents a solution to obtain interesting functional nano-structures of POM. This chapter presents a facile method of synthesis to improve catalyst recoverability and reusability by surfactant encapsulation. Surfactant encapsulation is an emerging methodology to synthesize self-assembled POMs nano-architectures. The use of quaternary ammonium surfactants like

dimethyldioctadecylammonium (DMDOA) with good stability and twin alkyl chains can provide platform for morphological control.

To date, several examples of surfactant encapsulated POMs with various architectures such as disk, cone, and flower have been reported.[129,207] While much work and development has been achieved on the aspects of structural and morphological studies,[208,209] works reporting the application of POMs architectures in advanced oxidation processes are limited. The synthesis of POMs with nano–architectures remains a daunting task due to the high crystalline energy and hydrophilic nature of POMs clusters.[26] This makes self-assembly nano-architecture of POMs a field of research worth exploring. Among the various structural variations of POMs, the Keggin structure is one of the most investigated as compared to the other members of the HPA family. The $H_{3+n}[PMo_{12-n}V_nO_{40}]$ series of mixed addenda Keggin type heteropolyanion has found wide applications in the selective oxidation for organic synthesis and other areas.[96,210-212] The preference can be mainly associated to their high redox reversibility in which re-oxidation can be achieved with molecular oxygen as a benign oxidant,[210] making them attractive oxidation catalysts and thus their viability to be developed as advanced functional materials.

In this chapter, HPA of the series $H_{n+3}[PMo_{(12-n)}V_nO_{40}]$ (n = 1, 2, 3), herein denoted as PVMA–1, PVMA–2 and PVMAA–3 were prepared. The PVMAs were then modified by a simple cationic exchange reaction with a quaternary ammonium surfactant, dimethyldioctadecylammonium bromide (DMDOA·Br), to give a series of surfactant encapsulated heteropolyanions (SEH–n) The as-prepared SEH–n are self-assembled inorganic-organic hybrid material with defined spherical morphology and multi-lamellar nano-structure (MLNS), the tunable nature of the anions allows the optimisation of the catalyst for catalytic wet air oxidation of organic pollutant under ambient conditions. The research and translation of HPA into effective catalyst for application in environmental remediation is crucial in the development as an effective molecular catalyst. Contrary to typical catalytic wet air oxidation (CWAO) process which requires high temperature and pressure[213], CWAO using these SEHs demonstrating MLNS were capable of the removal

of a recalcitrant organic pollutant, bisphenol A (BPA) from water under ambient conditions. The current work is essential in the understanding of (i) the formation and structural characteristics of the amphiphilic catalyst, and (ii) the feasibility of their application towards environmental remediation which requires less energy and chemical usage in water treatment processes.

5.2. Experimental

5.2.1. Chemicals

Na_2HPO_4, $NaVO_3$, $Na_2MoO_4 \cdot 2H_2O$, $(C_{18}H_{37})_2(CH_3)_2NBr$, bisphenol A (BPA) and $CHCl_3$ were purchased from Sigma-Aldrich and used without further purification. Sulfuric acid (95 – 97%) and diethyl ether were purchased from Honeywell and Fischer Scientific respectively. All solutions were prepared using MilliQ (MQ) water (18.2 MΩ cm^{-1}) unless otherwise stated. Phosphovanadomolybdic acid (PVMA-n) of the series $H_{3+n}(PMo_{12-n}V_nO_{40})$ (n = 1, 2, 3) were prepared as described in chapter 3.

5.2.2. Synthesis of material

The synthesis of the surfactant encapsulated heteropolyanions (SEHs) uses a single phase approach[170] and is prepared as mentioned in chapter 3.2.5.

5.2.3. Material Characterization

The morphological transformation of the PVMA to SEH was examined using a field emission scanning electron microscope, the local structure of the SEHs was studied using high resolution transmission electron microscope (HRTEM). Powder samples were loaded onto a PMMA sample holder and X-ray diffraction (XRD) patterns were obtained by Bruker D8 Advance X-ray diffractometer. The Brunauer-Emmett-Teller (BET) surface area was determined using N_2 adsorption-desorption isotherm analysis at 77 K. The Fourier transform infrared (FTIR) spectroscopy of the samples was performed using

Perkin Elmer GX over the range of 4000 – 400 cm^{-1}. Thermo-gravimetric analysis of the materials was carried out using TA Instruments Q500 under nitrogen flow of 40 mL min^{-1} and a heating rate of 10°C min^{-1}. All characterization were performed using the same specifications as mentioned in chapter 3.2.7. unless otherwise specified.

5.2.4. Catalytic Performance Studies

In the catalytic oxidation experiment using the SEHs, 1.0 g L^{-1} loading of SEH–n was added into an aqueous solution of bisphenol-A (BPA) (20 mg L^{-1}, 50 mL) at the natural pH of the solution under ambient conditions. The reaction vessel was covered during the oxidation experiment to preclude any interaction with light and reduce the loss of water. The reaction was deemed to have started upon the addition of the SEHs, which excludes any time for the attainment of adsorption–desorption equilibrium. Air was bubbled through the solution at a rate of 3.5 L min^{-1} through the solution for provision of dissolved oxygen as the oxidant for the catalytic wet air oxidation. Samples were drawn from the reactor at fixed time intervals and tested for BPA concentration in the solution using a Hypersil Gold reversed phase column (Thermo Scientific) with mobile phase composition of 60% acetonitrile and 40% deionized water at a flow rate of 1 mL min^{-1} on a Perkin Elmer HPLC system equipped with a UV-vis detector operating at 220 nm. The solutions were analysed after reaction with inductive coupled plasma–optical emission spectrometer for dissolved metals (ICP-OES, Perkin Elmer Optima 2000DV). XPS analysis was performed using JPS-9030 Photoelectron Spectrometer (JEOL, Japan) using non-monochromatic Mg K_α X-ray source with pass energy of 50 eV and analysis area of ~3 mmφ.

5.3. Results and Discussion

5.3.1. Material Characterization

Figure 5.1(a) shows the FESEM micrograph of PVMA–2. The PVMAs are generally water-soluble crystalline solids preventing their effective recovery from aqueous system.

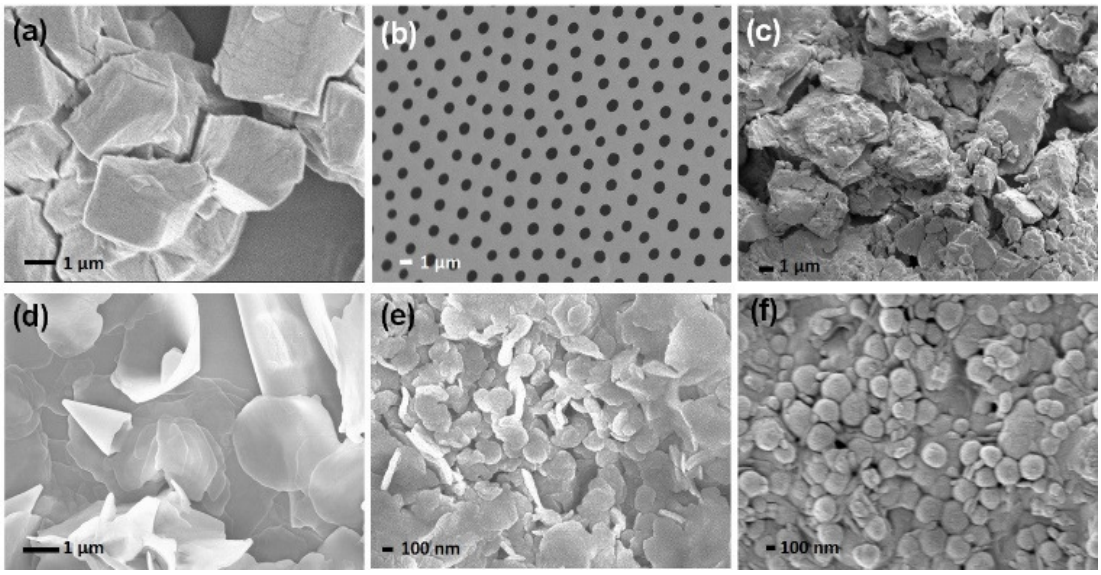

Figure. 5.1 SEM micrograph of (a) PVMA–2, (b) casted film of SEH, (c) bulk powder of SEH, (d) PVMA-2: DMDOA in ~1:2 ratio, (e) PVMA-2:DMDOA in ~1:3 ratio and (f) SEH from mixed solvent of chloroform : n-butanol in 3:1 ratio.

In this regards, the heterogeneity was introduced by replacing the exterior protons of PVM with DMDOA. The DMDOA was introduced via a simple cation modification method. After modification, the PVMs encapsulated in the SEHs are active sites supported with a surfactant matrix allow them to be effectively stabilised and used as a catalyst. The morphological transformation effect of the surfactant to PVM ratio on the series of Keggin HPA is studied using FESEM by following the transformation of the SEH from the HPA precursor at different surfactant to PVM ratios.

The preparation of SEHs with pure chloroform as the solvent via synthesis route 1 (Figure. 5.2) leads to the formation of a porous membrane-like structure with pores of 1 µm in diameter (Figure. 5.1(b)). Bulk SEH pulverized into fine powdered material does not allow us to obtain small particles with any controllable morphology as can be seen in Figure. 5.1(c). Therefore, the introduction of a co-solvent such as *n*-butanol is required to adjust the solvent polarity for morphological control of the SEHs. Since all PVM have similar diameter of *ca.* 1 nm, the directing force for controlled morphology will come from (i) solvent polarity control and (ii) stoichiometry control of the surfactant used. The formation of SEH particles with narrower size distribution is obtained by adding *n*-

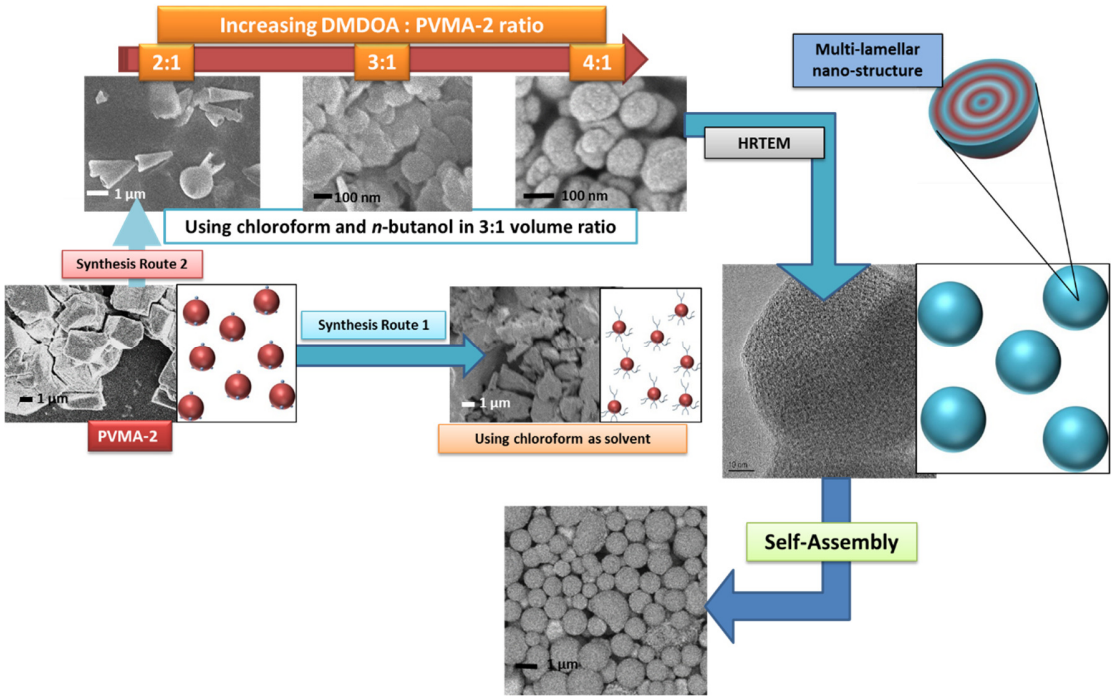

Figure. 5.2 Schematic illustration for synthesis and formation of SEH-2 from PVMA-2 and influence of DMDOA:HPA ratio.

butanol as a stabilizer during SEH synthesis[129] and solvent evaporation under ambient conditions can be achieved. With the addition of n-butanol to chloroform at volume ratio of 1:3 in synthesis route 2 (Figure. 5.2), we explore the effect of DMDOA to PVMA at different ratios on the SEH synthesis. Figure. 5.1(d) shows that with a ratio of approximately 2 DMDOA: 1 PVMA, mixed morphologies of nano-disk and nano-cone are obtained. Figure. 5.1(e) shows that the addition of DMDOA up to a ratio of 3:1 leads to the evolution of spherical particles with 150–200 nm in diameter. When stoichiometric amounts of DMDOA is added to the respective PVMA (i.e. PVMA–1: 4:1, PVMA–2: 5:1 and PVMA–3: 6:1) to replace all the protons, spherical particles starts to evolve as evidently shown in Figure 5.1(f). Considering that the Keggin-type POMs has a radius of 0.52 nm,[214] the surface area of a single PVM anion is estimated to be around 3.42 nm^2. The lateral area (0.567 nm^2) per DMDOA[215] therefore fully occupy the surface of PVMA–3, restricting the freedom of spatial arrangement with increase of DMDOA on the series of PVMA. As such, the complete substitution of the protons by DMDOA with the control of the solvent polarity exclusively leads to the formation of

spherical particles. Therefore, the increment of anionic charge on the PVMAs from −4 to −6 has no significant influence on the morphology. A mixed solvent system consisting of $CHCl_3$ and *n*-butanol (as the co-solvent) at the ratio of 1:3 was thus employed as the optimum synthesis condition to obtain spherical SEHs. In order to establish an equal platform for the catalytic studies, with primary focus on the activity of PVM (i.e. based on the degree of vanadium substitution), it is preferable that all the SEHs have a similar morphology.

We propose that formation of the primary building blocks (i.e. $(DMDOA_4(PMo_{11}VO_{40}))$ by the complete replacement of the H^+ in the PVMAs with the DMDOA surfactant is essential for the formation of spherical architecture. This is shown by the changes in the morphology of the SEH with increase in surfactant added as shown in Figure. 5.2. Only with the formation of the required primary building blocks, the self-assembly process to form a secondary spherical architecture with MLNS can be attained.

As shown by the HRTEM micrographs in Figure. 5.3, all the SEHs have spherical architecture with nano-dimensional MLNS. Due to the presence of molybdenum which reduces the transmission of electrons through the specimen, the MLNS is generally obscured in SEHs of larger sizes. Identifying a smaller particle in the micrograph of SEH–3 (Figure. 5.3(c)) allows us to effectively observe the presence of the MLNS with an interlayer distance of approximately 1.5 nm. This cluster self-assembly is typical of twin alkyl chain surfactants which forms vesicles with MLNS in solutions. While the lighter region consists of the surfactants, the darker regions consisting of nano-sized cluster *ca.* 1 nm in size (Figure. 5.3(d)) which shows the presence of Keggin anions within the SEH. The structural integrity of the Keggin anions is deemed to be retained throughout the modification process and is effectively stabilized within the surfactant encapsulation.

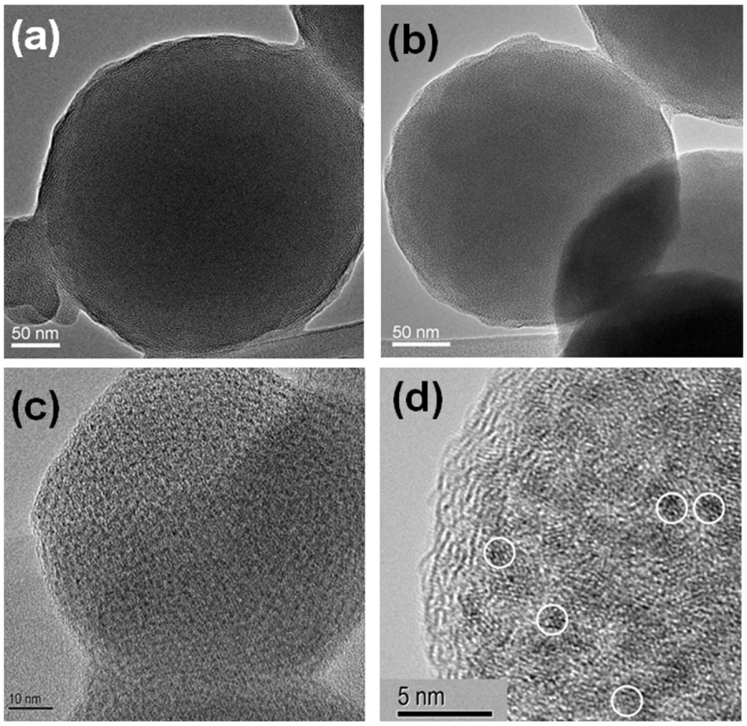

Figure. 5.3. High-resolution TEM micrograph of (a) SEH–1, (b) SEH–2, (c) SEH–3 and (d) SEH–2 at showing lattice fringes about 0.2 nm d-spacing inside each Keggin cluster with a diameter of ca. 1 nm (white circles).

Figure. 5.4 shows the XRD patterns of PVMA–1, DMDOA·Br and SEHs. The series of PVMAs prepared has a tetragonal crystal structure with space-group P4/mnc. As the increment in the substitution of Mo by V has little effect on the crystallographic arrangement of the material, XRD pattern of PVMA–1 presented here is representative of the PVMAs prepared. The EDX analysis performed on the PVMAs shows that the atomic percentage of phosphorus, molybdenum and vanadium estimated from the analysis matches the theoretical percentage (Table 5.1). All the reflections can be indexed to be coming from the single phase $H_4PMo_{11}VO_{40} \cdot 32\ H_2O$ (PDF#00-045-0611), which shows the PVMAs are prepared successfully.

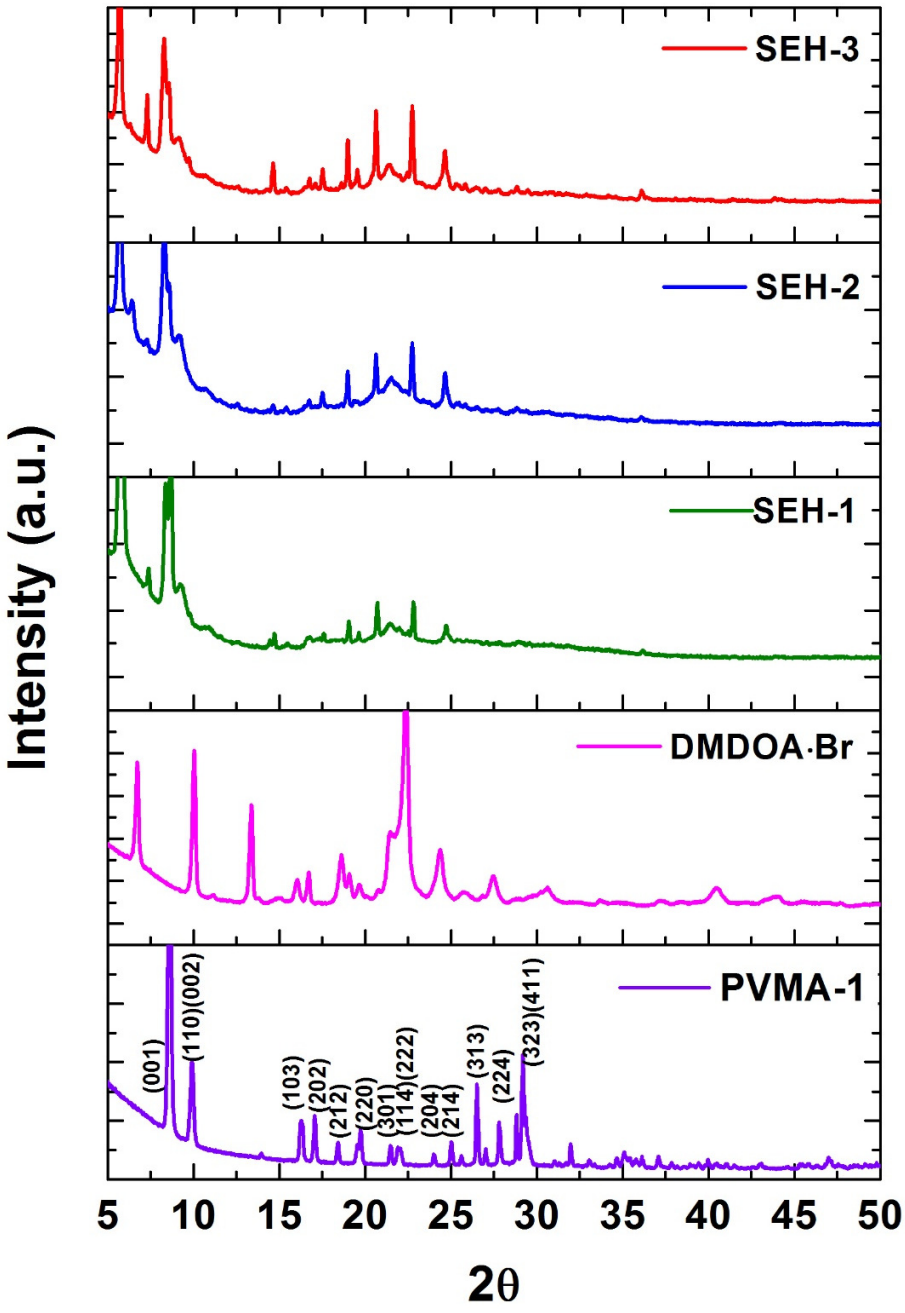

Figure 5.4. XRD patterns of PVMA-1, DMDOA·Br, SEH-1, SEH-2 and SEH-3. The peaks of PVMA-1 is indexed to single phase $H_4PVMo_{11}O_{40}$. Peaks in all SEHs between 15-25° indicates the presence of MLNS.

After modification with DMDOA, the typical reflection peaks of PVMA crystalline structure is no longer observed. The replacement of the protons by DMDOA and the loss of water of crystallization transformed the structure of the resulting SEHs. This leads to the transition from a crystalline solid to an amorphous material with MLNS. The observed reflections at *ca.* 5.7° and 8.3° are higher order reflections from the basal layer spacing in the MLNS. The Bragg reflection at 5.7° corresponds to the spacing of 1.6 nm which is in close agreement with the observed lamellar spacing in the HRTEM micrograph. The observed spacing suggests that the alkyl chains of the DMDOA are almost fully interdigitated which confines them to a tight and rigid structure. This results in the XRD peaks in typical Keggin anions in the range of 15–30° to be convoluted after modification with DMDOA. The new Bragg reflections arising between 15–25° are indicators of the rigid structure formed by the alkyl chains of DMDOA in the lamellar nano-structure as it becomes the determining factor in morphological control and the structure of the SEHs.

Table 5.5 EDX analysis providing semi-quantitative results of phosphorus, molybdenum and vanadium in PVMAs and SEHs normalized to 100% and BET surface area of PVMAs and SEHs. Phosphorus is not detectable by EDX in all SEH.

	Atomic % P	**Atomic % Mo**	**Atomic % V**	
	Experimental (theoretical)	**Experimental (theoretical)**	**Experimental (theoretical)**	**BET surface area/ $m^2 g^{-1}$**
PVMA–1	7.5 (7.7)	83.0 (84.6)	9.4 (7.7)	12.1
PVMA–2	7.6 (7.7)	75.0 (76.9)	17.3 (15.4)	4.4
PVMA–3	7.3 (7.7)	69.5 (69.2)	23.2 (23.1)	5.2
SEH–1	-	90.1 (91.7)	9.9 (8.3)	4.3
SEH–2	-	85.1 (83.3)	14.9 (16.7)	1.5
SEH–3	-	74.6 (75.0)	25.4 (25.0)	6.9

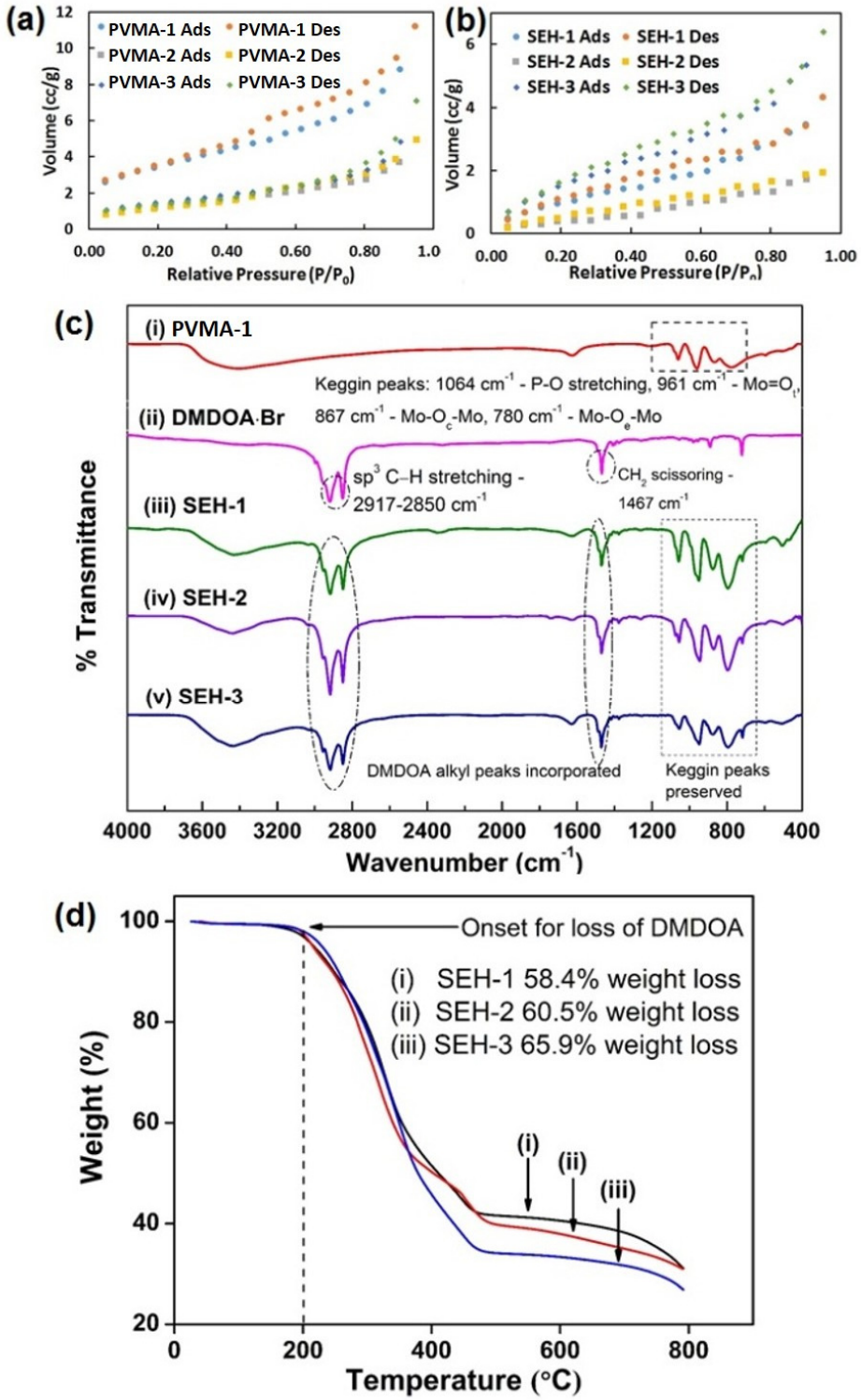

Figure. 5.5. BET sorption isotherm of (a) PVMAs and (b) SEHs. (c) FTIR of (i) $H_4[PMo_{11}VO_{40}]$, (ii) dimethyldioctadecylammonium bromide (iii) SEH–1, (iv) SEH–2 (v) SEH–3. (d)Thermo-gravimetric analysis weight loss profile of (i) SEH–1 (ii) SEH–2 (iii) SEH–3.

The EDX analysis performed on the SEHs shows that while phosphorus is undetectable due to the encapsulating matrix, the molybdenum to vanadium ratio estimated from analysis is in good agreement with theoretical percentage (Table 5.1). Figure 5.5(a) and (b) shows the BET sorption isotherm of the PVMAs and SEHs with their associated values as summarised in Table 5.1. While the surfactant modifies the SEH into a heterogeneous catalyst, it is interesting to note that the specific surface was not enhanced as a result of the modification. The SEH has a closely-packed MLNS, which results in low pore volume and porosity. Therefore, the surface area is largely limited to the external surface, leading to the SEHs having low specific surface area.

Figure. 5.5(c) shows the FTIR spectra. Characteristic peaks of the Keggin anion structure at 1064, 961, 867 and 780 cm^{-1} (Figure. 5.5(i)) corresponding to P–O stretching, Mo=O_t stretching of terminal oxygen, Mo–O_c–Mo stretching of corner-sharing MoO_6 octahedra and the edge sharing MoO_6 octahedra of Mo–O_e-Mo respectively is observed in PVMA–1. In the SEHs, the peaks are slightly shifted, i.e. in SEH–1, the characteristic peaks of Keggin anions are now at ~1060 cm^{-1}, 953 cm^{-1}, 877 cm^{-1} and 796 cm^{-1}. Additional bands are also observed for all the SEHs at 2917–2850 cm^{-1} and 1467 cm^{-1} attributed to the alkyl chain sp^3 C–H stretching and CH_2 scissoring of the quaternary amine surfactant DMDOA (Figure 5.5(c) (iii – v)). From the results, shifts in the characteristic Keggin peaks indicate the strong interaction between the PVM with DMDOA and the intactness of the Keggin structure. The resulting FTIR spectrum confirms that the ionic exchange reaction used in the formation of SEHs has no detrimental influence on the structure of the components.

The components of the as-prepared SEHs were determined using the thermo-gravimetric analysis. Minor weight loss below 100°C was observed due to the evaporation of water present within the interstitial of MLNS. As indicated in Fig. 5.5(d), the weight loss of the SEH–1, SEH–2 and SEH–3 are 58.4, 60.5 and 65.9% respectively. This indicates that the quaternary ammonium cations of DMDOA have fully replaced the protons of the HPA during the encapsulation process. The material is stable up to 200°C, after which the weight loss can be ascribed to the thermal decomposition of DMDOA ions. The good

stability of DMDOA and the electrostatic based interaction with the PVM gives the SEHs increased stability as compared to POMs grafted with organic components.

5.3.2. Catalytic wet air oxidation performance evaluation

Fig. 5.6(a) shows the catalytic degradation of BPA with PVMA–2, SEH–1, SEH–2 and SEH–3 as the catalyst. Studies are carried out to understand the observed difference in catalytic activity, the possible mechanism and the stability of the SEHs. The deliberate design of the catalyst with hydrophobic properties inherited from the use of DMDOA acts as a molecular trap for the BPA molecules; this facilitates the redox interaction of the BPA with the catalytic PVM centre. During the catalytic reaction, the vanadium sites are the active sites for catalytic redox process.[216] The V^{5+} is reduced to V^{4+}, then re-oxidation of the V^{4+} site to V^{5+} is facilitated by the dissolved molecular oxygen species.[210,217] The removal of BPA is higher in SEH–2 and SEH–3 as compared to SEH–1 over 180 min, primarily due to the higher degree of substitution of Mo by V.

Fig 5.6(b) shows the enhanced BPA removal under catalytic wet air oxidation. The concentration of dissolved oxygen species is maintained via interfacial reaeration, leading to an overall improvement in the removal of BPA. Since BPA is relatively non-volatile compound, aeration alone will be ineffective on its removal. The enhancement in removal of BPA by SEH–1, SEH–2 and SEH–3 after the introduction of aeration is prominent. PVM–2 and PVM–3 incorporated into the SEHs are catalytic centres with capability to accept at least 2 electrons. This is due to the presence of at least 2 V^{5+} in the PVMAs incorporated, making re-oxidation by oxygen more favourable. As oxygen is a poor one-electron acceptor, this results in relatively unfavourable re-oxidation of the catalytic centres in SEH–1 (i.e. PVM–1) by oxygen due to the catalytic centre being a one-electron reduced species. While SEH–3 with 3 V^{5+} per active site should have higher catalytic performance than that of SEH–2, the inherent structural instability caused by the

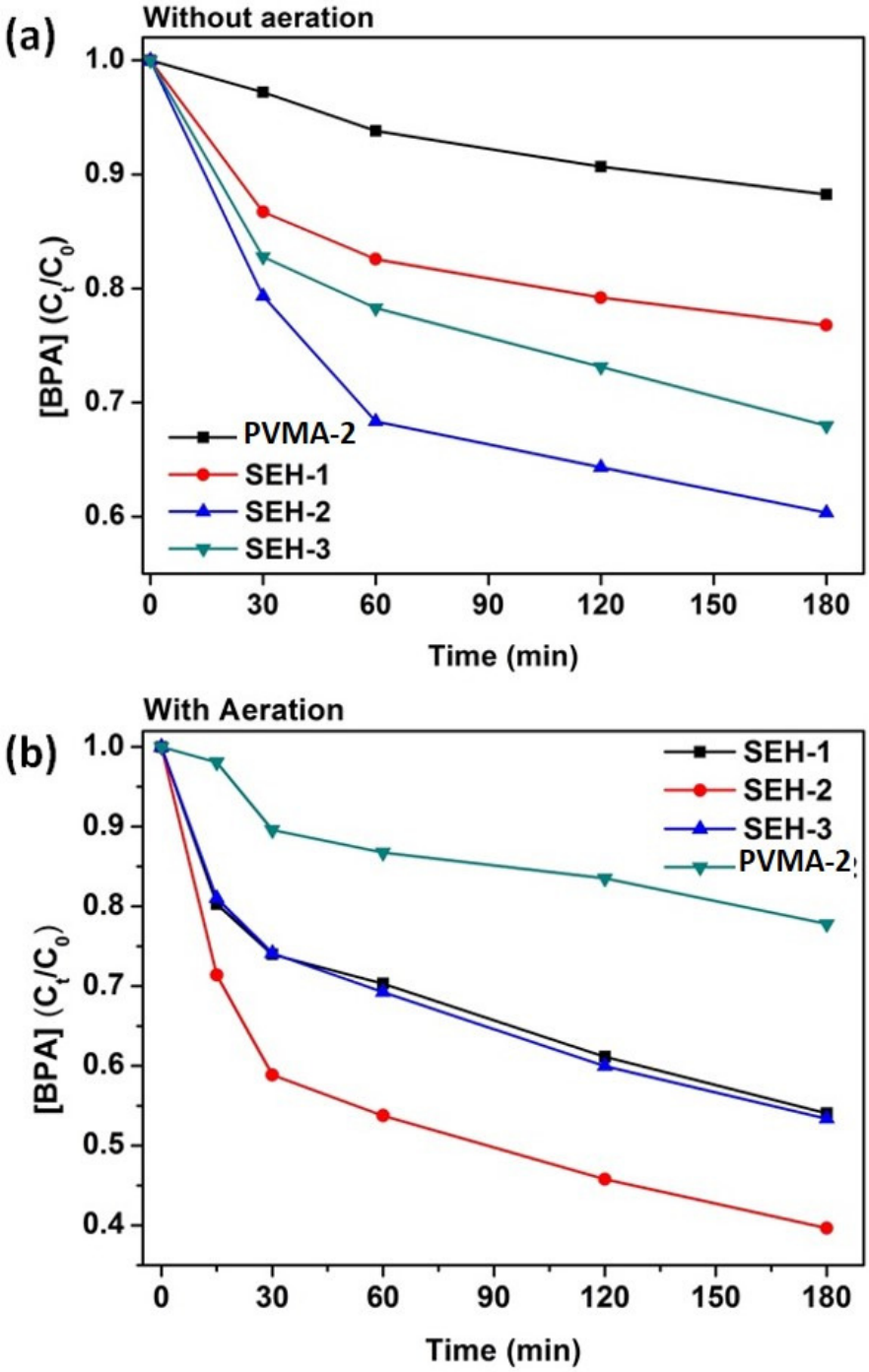

Figure 5.6 (a) Removal efficiency of BPA using SEHs and PVMA–2 without aeration. (b) Removal efficiency of BPA using SEHs and PVMA–2 with aeration.

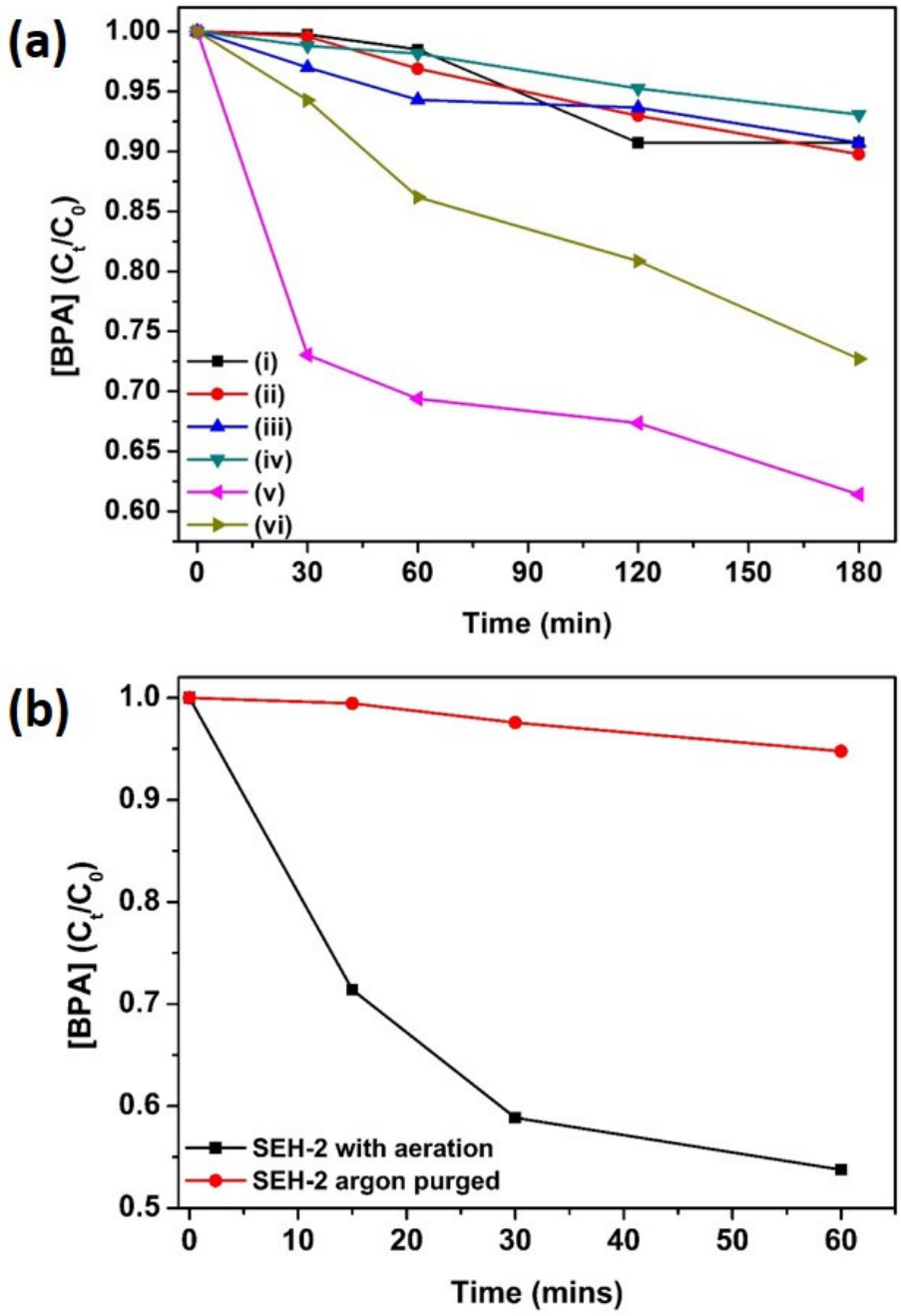

Figure 5.7 (a) BPA removal without aeration by (i) DMDOA:MVPA-2 2:1, (ii) DMDOA:MVPA-2 3:1 prepared with chloroform : *n*-butanol in 3:1 ratio; and (iii) DMDOA:MVPA-2 5:1 in pure chloroform. BPA removal with aeration by (iv) DMDOA:MVPA-2 2:1, (v) DMDOA:MVPA-2 3:1 prepared with chloroform : *n*-butanol in 3:1 ratio; and (vi) DMDOA:MVPA-2 5:1 in pure chloroform. (b) BPA removal using SEH–2 with aeration and in argon purged solution, showing limited adsorption effects in the absence of oxygen.

greater degree of substitution of molybdenum by vanadium[218] lead to SEH–2 out-performing SEH–3.

Moreover, with the steric crowding of the surfactant around the catalytic site in SEH–3, it can also lead to reduced mass transport of BPA and radical species to and fro the active site and thus hinders the catalytic performance. Despite the specific surface area of SEH–2 being the lowest (1.46 m^2 g^{-1}) of the 3 SEHs prepared, it is shown that stability in combination with the nano-structure are important for the effective utilization of the material. The concentration of Mo^{6+} in solution is found to be approximately 0.002 % for all SEHs and severe leaching of 1.75% and 0.98% of V^{5+} was found for SEH–1 and SEH–3. The SEH–2 shows exceptional stability with V^{5+} approximately 0.013% of leaching detected, which shows that the more efficient performance of SEH–2 was not due to effects of the active ions leaching into the solution. The influence of DMDOA to PVMA–2 ratio and solvent polarity on the catalytic activity of the materials prepared has also been studied (Fig. 5.7(a)) showing that increase in surfactant stabilises and enhances the properties of PVM–2 to be a more effective catalyst. While the poorer activity of the SEH–2 building blocks without solvent polarity control can be attributed to the lack of regularly formed MLNS within the material. The increase in surfactant ratio also stabilizes PVMA–2 within the surfactant matrix, with vanadium leaching at 0.8% (i.e. when DMDOA : PVMA–2 is 2:1) to 0.1% in the building blocks (i.e. when DMDOA : PVMA–2 is 5:1).

To demonstrate that SEHs are superior to their unmodified counterpart, PVMA–2 corresponding to the mass fraction in SEH–2 (i.e. as determined from TGA) was used as a homogeneous catalyst for the removal of BPA. It can be seen from Fig. 5.6(a) and Fig. 5.6(b) that PVMA–2 is unable to effectively remove BPA as its use as a homogeneous catalyst requires careful control at pH 2 in order to prevent the hydrolysis of the Keggin anion at higher pH. Comparing this result with that obtained using SEH–2 shows that the surfactant modification has provided the desired enhancement in stability, efficiency and heterogeneity.

As the DMDOA surfactants make up a large percentage of SEHs composition as shown by TGA analysis, the plausibility of the BPA adsorption by SEHs must be investigated. A control study with SEH–2 was employed for further investigation. The BPA solution was purged with argon for 30 min prior to catalytic testing. Fig. 5.7(b) shows the difference when oxygen is precluded from the solution. No significant contribution by adsorption is observed and only a slight drop in BPA concentration is detected after one hour, which is likely caused by small fraction of oxidation by the catalyst. The oxidative catalytic process was hindered due to lack of oxygen as a co-factor to interact with the catalytic centre for regeneration of active sites. Therefore, the effectiveness of the wet air oxidation process is dependent on the presence of dissolved oxygen.

Typical wet air oxidation processes operate through a free radical mechanism[219] which can be described by the following equations:

$$SEH + n\,RH \rightarrow SEH^{Red} + n\,R\cdot + n\,H^{+} \quad \text{Eqn (5.1)}$$

$$R\cdot + O_2 \rightarrow RO_2\cdot \quad \text{Eqn (5.2)}$$

$$RO_2\cdot + RH \rightarrow ROOH + R\cdot \quad \text{Eqn (5.3)}$$

$$ROOH \rightarrow RO\cdot + \cdot OH \quad \text{Eqn (5.4)}$$

where RH is the organic species and SEH^{Red} is the reduced SEH species; and the degradation of BPA via direct redox reaction centred on the SEH can be delineated by the following equations[46]:

$$SEH + Red \rightarrow SEH^{Red} + Ox \quad \text{Eqn (5.5)}$$

$$SEH^{Red} + \frac{n}{4}O_2 + nH^{+} \rightarrow SEH + \frac{n}{2}H_2O \quad \text{Eqn (5.6)}$$

where Red is the BPA and Ox is the oxidised BPA.

The PVM in SEH becomes reduced when mixed with the solution containing the organic pollutant as shown in Eqn. (5.1). At pH 3 as shown in Fig. 5.8(a), the degradation of BPA

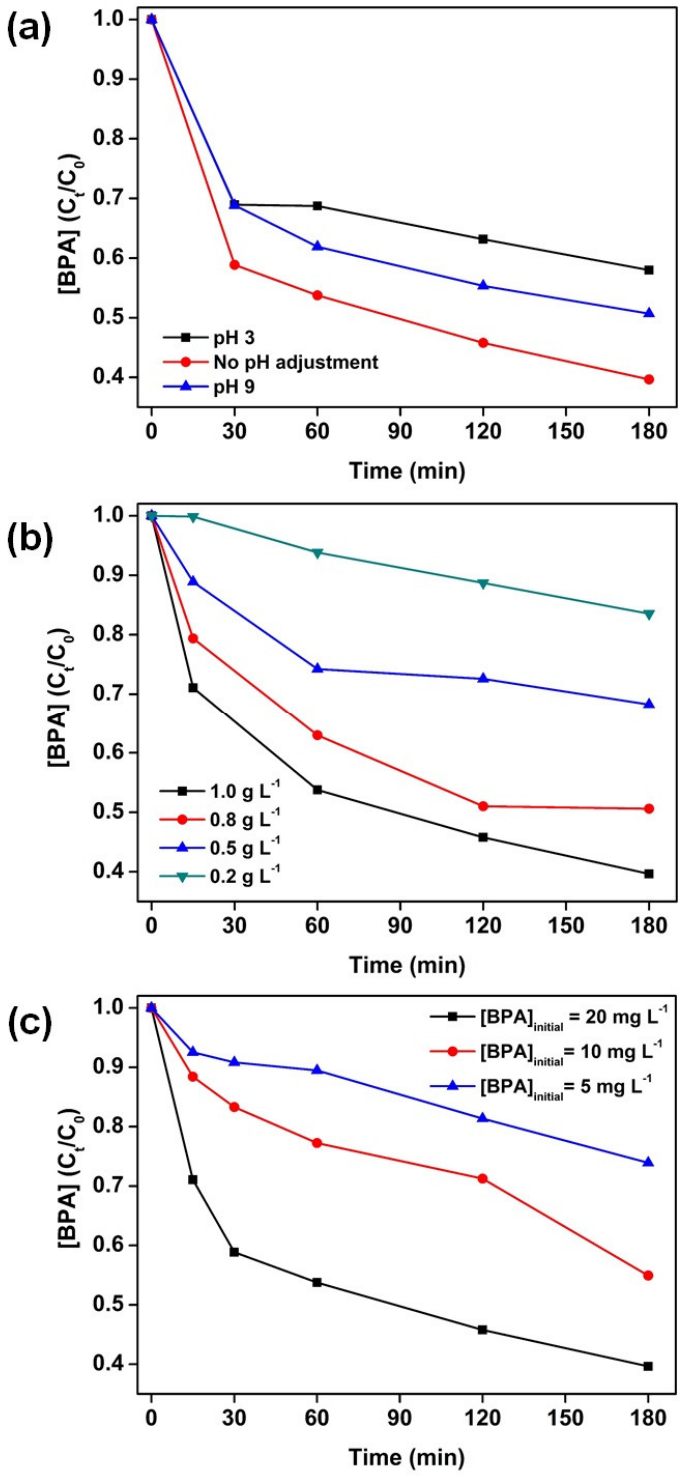

Figure 5.8. BPA removal efficiency (a) at pH3, pH9 and without pH adjustment; (b) at different SEH loading of 1.0, 0.8, 0.5, 0.2 g L^{-1} and (c) at initial BPA concentration of 20, 10, 5 mg L^{-1}.

is reduced as compared to natural pH conditions. The lower pH might reduce the formation of R- by impeding the formation of R· in Eqn. (5.1). At pH 9, the formation of R- is more favourable, encouraging the propagation towards the generation of ·OH radical via free radical chain auto-oxidation process. This leads to an increase in the removal of BPA. However, we find that under natural pH condition (i.e. pH≈6.2), the removal of BPA is higher. The higher pH increases the formation of radical species; it may also counteract and adversely affect the re-oxidation of SEH in Eqn. (5.6). Therefore, natural pH condition proves to be more favourable for the removal of BPA.

Eqn (5.2) and (5.3) are key processes in the production of ·OH radical. Therefore, the regeneration of active sites on the SEH with aeration (Eqn. (5.2)) to the solution can

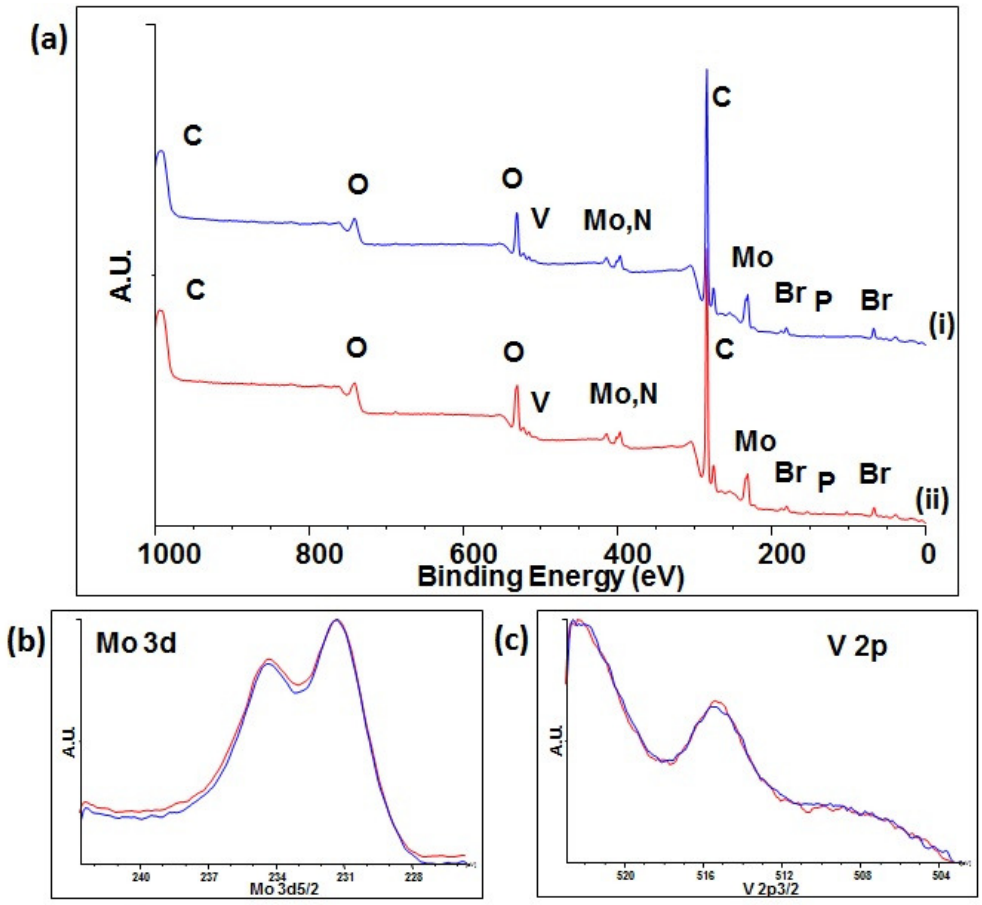

Figure 5.9 XPS analysis results of SEH-2 (a) (i) before catalytic experiment and ii) after catalytic experiment. XPS spectra of (b) Mo and (c) V (blue = before catalytic experiment, red = after catalytic experiment).

expedite the generation of ·OH (Eqn. (5.4)) via autocatalytic decomposition and provide enhancement in the degradation efficiency of BPA. The lipophilic portion of the SEH will allow Red accompanied by oxygen to come into proximity with the active site of more easily. The consequent reduction of the PVM active site within the SEH is accompanied by the electron donor (i.e. BPA) being oxidised as outlined in Eqn. (5.5). Oxygen is then responsible for oxidising the reduced POM site in SEH^{Red} in Eqn. (5.6), mediating the redox process between V^{5+} and V^{4+} under mild conditions. This is evident from Fig. 5.6 where the removal of BPA is improved with the introduction of aeration to the system. The aeration also improves the re-oxidation of the SEH in Eqn. 5.6, thereby giving enhancement in performance.

Fig. 5.8(b) presents the effects of SEH–2 loading on the removal of BPA. The removal of BPA was found to improve with the increase in SEH–2 loading. The increase in catalytic sites improves the reaction rate in Eqn. (5.1) and (5.5) giving improvement in removal. Fig. 5.8(c) illustrates the influence of initial BPA concentration on the removal of BPA. The lower BPA concentration results in lower availability of BPA for the formation of R·. There is a lower production of ·OH which reduces the removal of BPA as a result.

In addition, XPS analysis was carried out on SEH–2 for evaluation of the practicality of regeneration of the catalyst (Fig. 5.9). Results from the analysis indicates that the catalyst structure is unaffected after use as there is no shift in the bonding energies of Mo 3d (Fig. 9(b)) and V 2p (Fig. 5.9(c)) after the reaction. The bromine found in the catalyst could be trapped within the MLNS during catalyst preparation and could have reduced the catalytic efficiencies of the SEHs as a radical scavenger. Fig. 5.10(a) shows the comparison of the FTIR spectrum of SEH–2 before and after catalytic application, we can see that the main difference is the loss of the broad OH stretching at ~3500 cm^{-1}. This is attributed to water trapped within the fresh catalyst during synthesis; while the catalyst was dried extensively post catalytic testing, leading to loss of the OH stretching peak. Moreover, we note that that characteristic peaks of PVM–2 and the surfactant component remains consistent between the two spectrum, indicating the stability of the catalyst and that BPA was not adsorbed on the SEH.

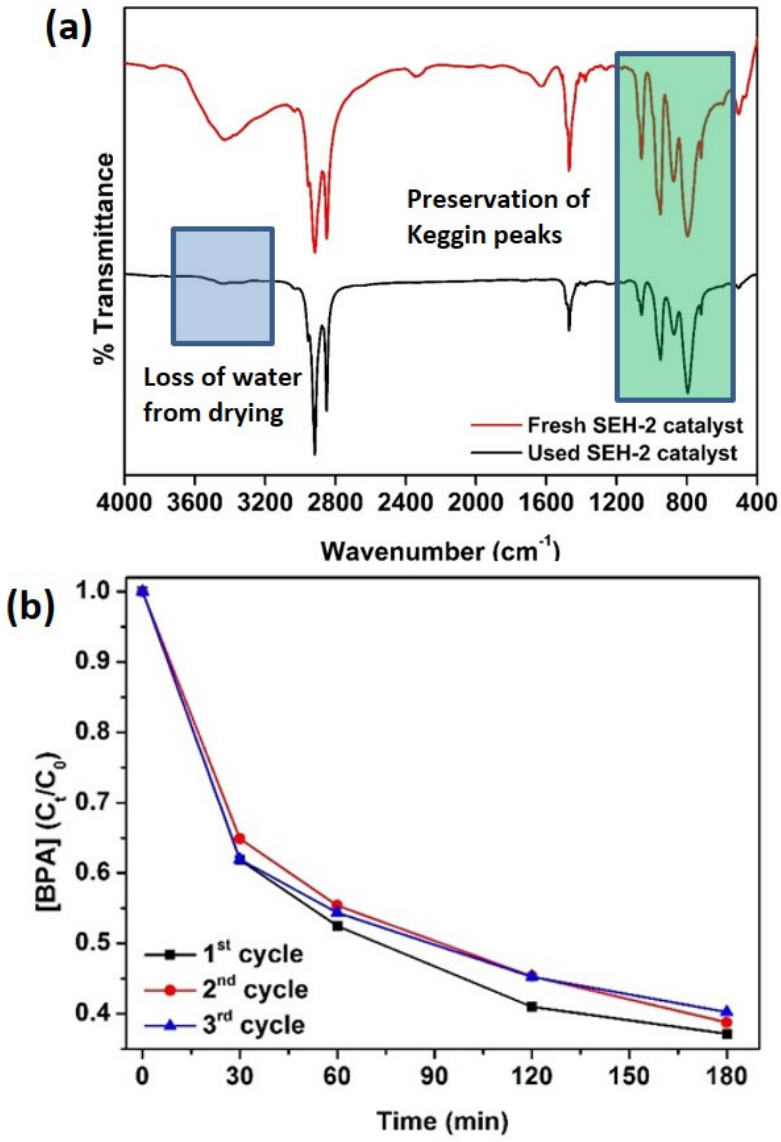

Figure 5.10 (a) FTIR spectrum of fresh SEH–2 and used SEH–2. Fresh catalyst exhibits characteristic peaks of water, while the used catalyst shows no presence of water after drying post usage. The Characteristic peaks of PVM–2 and DMDOA are consistent before and after catalytic procedure. (b) BPA removal by SEH-2 over 3 consecutive cycles,

In comparison with previous work preparing amphiphiles comprising of POMs and surfactant which forms micellar catalyst within the solution,[147] the employment of a di-alkyl surfactant provides controllability in the formation of SEHs with MLNS. The encapsulation by surfactant allows the PVMs to be stabilised in a heterogeneous form within the SEH with 0.013% leaching of active vanadium species. This also provides a better platform for understanding of molecular ion catalysis in aqueous solutions. The SEHs being heterogeneous in an aqueous environment is another advantage of this material, as they could be recovered by simple filtration or centrifugation at the end of a catalytic process. Fig. 5.10(b) shows the recycling performance of SEH–2 over 3 cycles. SEH–2 is able to retain consistent level of BPA removal without a significant drop in performance (< 5%). This shows that the catalyst is relatively stable and can be effectively recycled after each catalytic reaction.

5.4. Conclusion

Nano-spherical surfactant encapsulated heteropolyanion for catalytic application were prepared with amphiphilic surfactant of DMDOA·Br and phosphovanadomolybdic acids as precursors for modification. The increment of anionic charge on the PVMAs has no significant influence on the morphology of the SEHs due to lower freedom of surfactant orientation around the PVMA. The selection of mixed solvent system of chloroform and *n*-butanol stabilises the particle size of the primary building blocks to be reduced towards the nano-sized dimension and isolated in stabilised dried state with controlled morphology. The current study has shown the promising potential of SEHs as an advanced functional material for catalytic wet air oxidation of organic pollutant under mild condition which is desirable as this reduces the related energy used and treatment cost. Although the surfactant increases the interaction probability of the target organic pollutant with the PVM catalytic centres, the catalytic efficiency of the system might also be reduced due to hindrance to mass transport of radical species for the propagation of degradation reaction throughout the system. While maintaining the advantages of stability and use of mild conditions in current system, future research will look into (i) use of ionic-liquids with

functionalised hydrophobic structure for added functionalities and (ii) strategies to improve the performance of the system by structural and morphological controls.

Chapter 6

Conclusions and recommendations

In this dissertation, the studies revolving around the preparation and application of polyoxometalates based nano-architecture were presented. The preparation based on immobilization of PVMA on TiO_2 and surfactant encapsulation are concluded and reflected. The insights from the studies performed were summarized and opportunities for future studies are recommended herein.

6.1. Conclusions

The synthesis and design of polyoxometalates-based heterogeneous catalyst was studied by immobilization and surfactant encapsulation strategies in this dissertation. The choice of polyoxometalates used throughout the study is the Keggin type heteropolyacid, phosphovanadomolybdic acid. The choice of polyoxometalates was made due to their stability and high redox reversibility. In chapter 3, the polyoxometalates were prepared and made into nano-architectures. The immobilization of PVMA-2 on TiO_2 NP described in chapter 3 establishes foundation knowledge and understanding of such surface modification process in the preparation of the nano-architecture. The synergistic effect derived from the combination of the two materials providing highly redox active material for lithium-ion battery with good cycling stability and electrochemical properties is highly encouraging in the research of such hybrid material. However, the low amounts of PVMA-2 immobilized on the surface of the TiO_2 NP likely due to insufficient surface amine groups and relatively low surface area of the TiO_2 NP could be reasons preventing the material from performing at its optimum potential.

Titanate nanotubes (TNTs) with high surface area was used as a solid support for PVMA-2 in chapter 4. With a higher surface area of the support, PVMA-2 immobilization on amine-functionalized support forms crystalline phase as evident from the XRD diffractogram. This increases the specific surface area of PVM as compared to the bulk crystal and also heterogenised PVM for ease of recovery after catalytic application. The presence of the crystalline phase enables the prepared material to be effectively used as a bulk type II polyoxometalate heterogeneous catalyst. The design and engineering of the material allow the study of the photocatalytic properties and parameters PVMA-2, since TNT theoretically plays the role of an inert support during photocatalysis using visible light.

In Chapter 5, vanadium substituted phosphomolybdic acid ($H_{(3+n)}[PV_nMo_{(12-n)}O_{40}]$) was heterogenised by strategically encapsulating with a cationic surfactant of DMDOA, forming MLNS. This provided a material with exceptional stability and opens up its

application as a catalytic wet air oxidation catalyst under ambient conditions. Such material circumvents the need for high energy in wastewater remediation and thus further development may open up its potential application. In Chapter 5, even though the SEHs have low surface area, enhanced catalytic activity is achieved due to adsorption enhancement provided by the surfactant encapsulation. This also circumvents the problems of high solubility of HPA, allowing the effective recovery after catalytic reaction, increasing the environmental friendliness of its use. The increment of anionic charge on the PVMAs was found to have no significant influence on the morphology of the SEHs due to lower freedom of surfactant orientation around the POM. The selection of mixed solvent system of chloroform and *n*-butanol stabilises the particle size of the primary building blocks to be reduced towards the nano-sized dimension and isolated in stabilised dried state with controlled morphology.

The studies performed in this dissertation have provided several insights for the design of polyoxometalates based nano-architecture.

1. Immobilization of polyoxometalates within TiO_2 cannot be effectively achieved with morphological control when TiO_2 precursor and PVMA-2 are present in different phases.
2. Nano-architecture design based on surface modification of TiO_2 with PVMA-2 allows the effective exploitation of high redox-active properties of polyoxometalates.
3. High specific surface area is likely required for solid support used for immobilization of polyoxometalates (i.e. PVMA-2) for the material to act effectively as a photocatalyst. This can be seen from results derived from chapter 4 where formation of crystalline PVMA-2 phase in addition to high specific surface area contribute to the effective use of the prepared material in the degradation of methylene blue.
4. Nano-architecture prepared by surfactant encapsulation by DMDOA·Br has morphological restriction due to limitation in free of orientation as number of surfactant increases. Under conditions where degree of freedom for reorientation of surfactant is possible, morphology can be influenced by solvent polarity and surfactant ratio.

5. Surfactant encapsulation provides exceptional stability for PVMAs enabling their application as wet air oxidation catalyst at circumneutral pH. Effective mass transport to active catalytic site is likely required for further enhancement of efficiency.

In conclusion, the novel nano-architecture of POMs on TiO_2 NP lead to a synergistic combination where the highly redox active property of POMs can be effectively exploited. This also led to the eventual successful design of POMs immobilized TNT where the nano-architectural design gives a visible-light responsive photocatalyst. The preparation of SEHs with MLNS as a novel material for CWAO provides a catalyst with high stability operating at circumneutral pH and ambient conditions. This reduces the additional chemicals and energy need when such materials can effectively treat wastewater.

6.2. Recommendations

1. In chapter 4, titanate nanotubes (TNTs) were surface functionalized and immobilized with PVM. However, the TNTs was a non-photoactive support which limited the photocatalytic activity of the prepared materials to be restricted to the PVMs.
   a. More studies can be performed to understand the kinetics and the degradation pathway of the organic dyes.
   b. The intrinsic electronic properties of the prepared material can be further investigated by Mott-Schottky measurements[220] done in combination with impedance techniques.
   c. Studies with radical scavengers to determine if degradation process is dominated by production of radicals or by photoredox activity of polyoxometalates.
   d. Studies to investigate the degradation of more diverse range of organic molecules present as micro-pollutants in water matrix.
   e. Metal nanoparticles can be added to the surface of the material to improve the visible light harvesting for photocatalysis.
   i. The anti-bacterial activity of the silver nanoparticles modified material can be studied.

f. The TNTs can be calcined to make them photoactive before further surface modification with PVMs. The preparation process is considered as such due to likelihood that PVMs typically have thermal stability up to 350°C only.
g. Modification of PVM with counter-cations which can extend its stability in more alkaline pH should be explored to improve the practicality of usage.
h. Incorporation of other types of transition metal substituted polyoxometalates.
   i. Use of iron substituted polyoxometalates for photo-Fenton degradation of pollutants
   ii. Use of cobalt substituted polyoxometalates as a peroxymonosulfate activator.
   iii. The nano-architecture prepared from TNTs and PVM can be fabricated into ceramic membranes for easier incorporation into a continuous flow system.

2. The high surface area of TNT used in chapter 4 is likely the key contributing factor to allow effective usage of the PVM immobilized TNT as a photocatalyst. Therefore, the use of supports with high specific surface area can be explored to improve the functionality of the material as a photocatalyst.
   a. The use of graphene or carbon nanotubes for modification with polyoxometalates has been generally focused on energy based application[84]. It is an opportunity to translate the application towards environmental remediation applications as shown in this dissertation from chapter 3 to chapter 4. While TNTs have surface covered with hydroxyl groups which makes it easy for functionalization, the similar approach will require to preparation of graphene/CNTs with sufficient defect sites to provide an effective support of polyoxometalates on its surface.
   b. The immobilization of polyoxometalates can also be performed on zeolites[221] and studies should be done to explore the influence of nano-environment on the degradation of organic pollutant molecules.
   c. Use of layered double hydroxide as a solid support for polyoxometalates[222]. Layered double hydroxide have high surface area, however much of the studies performed in this area are directed towards organic transformations[223-226]. Studies should be extended towards the use of polyoxometalates intercalated in layered double hydroxide for advanced oxidation processes.

3. Studies on the use of surfactant encapsulation for heterogenization of polyoxometalates typically revolve around their use as phase transfer catalyst[82] or for the purpose of oxidative desulfurization[148,227]. The formation of nano-architecture for the formation of organic-inorganic hybrids represents a field that has potential for further exploration.
   a. Studies can be done on a wider range of organic pollutants to better understand the mechanism and kinetics of degradation.
   b. The use of gemini surfactant represents an attractive area for the studies of possible nano-architectural design. However, such hybrid assemblies prepared in studies have no distinctive morphology[228]. This provides attractive research opportunities for studies to determine factors like surfactant hydrophilic lipophilic balance and solvent control can influence the formation of nano-architectures. Further research can delve into their application as heterogeneous catalysts for advanced oxidation processes.
   c. Ionic-liquids also provide an attractive strategy for heterogenization of poloyoxometalates[95,229]. With the potential functionality that can be incorporated with the organic moiety, the preparation of ionic liquid based polyoxometalates will enable the preparation of advanced multi-functional materials.

References

1 Pache, A. *Polyoxometalates, the other discovery by D'Elhuyar brothers*, <http://mappingignorance.org/2015/04/01/polyoxometalates-the-other-discovery-by-delhuyar-brothers/#note-2315-7> (2015).

2 Okuhara, T., Mizuno, N. & Misono, M. in *Advances in Catalysis* Vol. Volume 41 (eds Werner O. Haag D.D. Eley & Gates Bruce) 113-252 (Academic Press, 1996).

3 Misono, M. Unique acid catalysis of heteropoly compounds (heteropolyoxometalates) in the solid state. *Chemical Communications*, 1141-1152, doi:10.1039/B102573M (2001).

4 Nisar, A., Lu, Y. & Wang, X. Assembling Polyoxometalate Clusters into Advanced Nanoarchitectures. *Chemistry of Materials* **22**, 3511-3518, doi:10.1021/cm100691a (2010).

5 Zhou, Y., Chen, G., Long, Z. & Wang, J. Recent advances in polyoxometalate-based heterogeneous catalytic materials for liquid-phase organic transformations. *RSC Advances* **4**, 42092-42113, doi:10.1039/C4RA05175K (2014).

6 Xie, Y. B. Photoelectrochemical reactivity of polyoxophosphotungstates embedded in titania tubules. *Nanotechnology* **17**, 3340-3346, doi:10.1088/0957-4484/17/14/002 (2006).

7 Efremenko, I. & Neumann, R. Protonation of Phosphovanadomolybdates H3+xPVxMo12–xO40: Computational Insight Into Reactivity. *The Journal of Physical Chemistry A* **115**, 4811-4826, doi:10.1021/jp201420z (2011).

8 Tessonnier, J.-P., Goubert-Renaudin, S., Alia, S., Yan, Y. & Barteau, M. A. Structure, Stability, and Electronic Interactions of Polyoxometalates on Functionalized Graphene Sheets. *Langmuir* **29**, 393-402, doi:10.1021/la303408j (2013).

9 He, J. *et al.* Novel polyoxometalate@g-C3N4 hybrid photocatalysts for degradation of dyes and phenolics. *Journal of Colloid and Interface Science* **456**, 15-21, doi:10.1016/j.jcis.2015.06.003 (2015).

10 Pettersson, L., Andersson, I. & Oehman, L. O. Multicomponent polyanions. 39. Speciation in the aqueous hydrogen ion-molybdate(MoO42-)-hydrogenphosphate(HPO42-) system as deduced from a combined Emf-phosphorus-31 NMR study. *Inorganic Chemistry* **25**, 4726-4733, doi:10.1021/ic00246a028 (1986).

11 Huang, L., Hu, J., Ji, Y., Streb, C. & Song, Y.-F. Pyrene-Anderson-Modified CNTs as Anode Materials for Lithium-Ion Batteries. *Chemistry – A European Journal* **21**, 18799-18804, doi:10.1002/chem.201501907 (2015).

12 Pope, M. T. & Müller, A. Polyoxometalate Chemistry: An Old Field with New Dimensions in Several Disciplines. *Angewandte Chemie International Edition in English* **30**, 34-48, doi:10.1002/anie.199100341 (1991).

13 Nisar, A., Lu, Y., Zhuang, J. & Wang, X. Polyoxometalate Nanocone Nanoreactors: Magnetic Manipulation and Enhanced Catalytic Performance. *Angewandte Chemie International Edition* **50**, 3187-3192, doi:10.1002/anie.201006155 (2011).

14 Wang, H. *et al.* In Operando X-ray Absorption Fine Structure Studies of Polyoxometalate Molecular Cluster Batteries: Polyoxometalates as Electron Sponges. *Journal of the American Chemical Society* **134**, 4918-4924, doi:10.1021/ja2117206 (2012).

15 Mo, J., Zhang, Y., Xu, Q., Lamson, J. J. & Zhao, R. Photocatalytic purification of volatile organic compounds in indoor air: A literature review. *Atmospheric Environment* **43**, 2229-2246, doi:http://dx.doi.org/10.1016/j.atmosenv.2009.01.034 (2009).

16 Finke, R. G., Droege, M., Hutchinson, J. R. & Gansow, O. Trivacant heteropolytungstate derivatives: the rational synthesis, characterization, and tungsten-183 NMR spectra of P2W18M4(H2O)2O6810- (M = cobalt,copper,zinc). *Journal of the American Chemical Society* **103**, 1587-1589, doi:10.1021/ja00396a062 (1981).

17 Lu, L. *et al.* Preparation, characterization, and photocatalytic activity of three-dimensionally ordered macroporous hybrid monosubstituted polyoxometalate K5[Co(H2O)PW11O39] amine functionalized titanium catalysts. *Journal of Molecular Catalysis A: Chemical* **394**, 283-294, doi:http://dx.doi.org/10.1016/j.molcata.2014.06.037 (2014).

18 Yang, Y., Wu, Q., Guo, Y., Hu, C. & Wang, E. Efficient degradation of dye pollutants on nanoporous polyoxotungstate–anatase composite under visible-light irradiation. *Journal of Molecular Catalysis A: Chemical* **225**, 203-212, doi:http://dx.doi.org/10.1016/j.molcata.2004.08.031 (2005).

19 Walsh, J. J., Bond, A. M., Forster, R. J. & Keyes, T. E. Hybrid polyoxometalate materials for photo(electro-) chemical applications. *Coordination Chemistry Reviews* **306, Part 1**, 217-234, doi:http://dx.doi.org/10.1016/j.ccr.2015.06.016 (2016).

20 Zhou, Y., Guo, Z., Hou, W., Wang, Q. & Wang, J. Polyoxometalate-based phase transfer catalysis for liquid-solid organic reactions: a review. *Catalysis Science & Technology* **5**, 4324-4335, doi:10.1039/C5CY00674K (2015).

21 Wang, X., Tian, A. & Wang, X. Architectural chemistry of polyoxometalate-based coordination frameworks constructed from flexible N-donor ligands. *RSC Advances* **5**, 41155-41168, doi:10.1039/C5RA05270J (2015).

22 Wang, S.-S. & Yang, G.-Y. Recent Advances in Polyoxometalate-Catalyzed Reactions. *Chemical Reviews* **115**, 4893-4962, doi:10.1021/cr500390v (2015).

23 Rousseau, G. *et al.* Tuning the Dimensionality of Polyoxometalate-Based Materials by Using a Mixture of Ligands. *Crystal Growth & Design* **15**, 449-456, doi:10.1021/cg501524a (2015).

24 Omwoma, S., Gore, C. T., Ji, Y., Hu, C. & Song, Y.-F. Environmentally benign polyoxometalate materials. *Coordination Chemistry Reviews* **286**, 17-29, doi:http://dx.doi.org/10.1016/j.ccr.2014.11.013 (2015).

25 Wang, X., Zhang, H., Wang, E., Han, Z. & Hu, C. Phosphomolybdate-polypyrrole composite bulk-modified carbon paste electrode for a hydrogen peroxide amperometric sensor. *Materials Letters* **58**, 1661-1664, doi:http://dx.doi.org/10.1016/j.matlet.2003.10.044 (2004).

26 Proust, A., Thouvenot, R. & Gouzerh, P. Functionalization of polyoxometalates: towards advanced applications in catalysis and materials science. *Chem Commun (Camb)*, 1837-1852, doi:10.1039/b715502f (2008).

27 Kortz, U. *et al.* Polyoxometalates: Fascinating structures, unique magnetic properties. *Coordination Chemistry Reviews* **253**, 2315-2327, doi:http://dx.doi.org/10.1016/j.ccr.2009.01.014 (2009).

28 Rhule, J. T., Hill, C. L., Judd, D. A. & Schinazi, R. F. Polyoxometalates in Medicine. *Chemical Reviews* **98**, 327-358, doi:10.1021/cr960396q (1998).

29 Joo, N. *et al.* Organosilyl/-germyl Polyoxotungstate Hybrids for Covalent Grafting onto Silicon Surfaces: Towards Molecular Memories. *Chemistry – A European Journal* **16**, 5043-5051, doi:10.1002/chem.200903336 (2010).

30 Streb, C. New trends in polyoxometalate photoredox chemistry: From photosensitisation to water oxidation catalysis. *Dalton Transactions* **41**, 1651-1659, doi:10.1039/C1DT11220A (2012).

31 Misono, M. in *Studies in Surface Science and Catalysis* Vol. Volume 75 (eds F. Solymosi L. Guczi & TÉTÉNyi P) 69-101 (Elsevier, 1993).

32 Baxter, S. M. & Wolczanski, P. T. Improved synthesis, redox chemistry, and magnetism of the mixed-valence isopolyanion of vanadate V10O264. *Inorganic Chemistry* **28**, 3263-3264, doi:10.1021/ic00315a036 (1989).

33 Hiskia, A., Mylonas, A. & Papaconstantinou, E. Comparison of the photoredox properties of polyoxometallates and semiconducting particles. *Chemical Society Reviews* **30**, 62-69, doi:10.1039/A905675K (2001).

34 Papaconstantinou, E. Photocatalytic oxidation of organic compounds using heteropoly electrolytes of molybdenum and tungsten. *Journal of the Chemical Society, Chemical Communications*, 12-13, doi:10.1039/C39820000012 (1982).

35 Mylonas, A., Hiskia, A. & Papaconstantinou, E. Contribution to water purification using polyoxometalates. Aromatic derivatives, chloroacetic acids. *Journal of Molecular Catalysis A: Chemical* **114**, 191-200, doi:http://dx.doi.org/10.1016/S1381-1169(96)00317-2 (1996).

36 Mylonas, A., Papaconstantinou, E. & Roussis, V. Photocatalytic degradation of phenol and p-cresol by polyoxotungstates. mechanistic implications. *Polyhedron* **15**, 3211-3217, doi:http://dx.doi.org/10.1016/0277-5387(96)00034-4 (1996).

37 Hiskia, A., Troupis, A., Antonaraki, S., Gkika, E. & Papaconstantinou, E. Polyoxometallate photocatalysis for decontaminating the aquatic environment from organic and inorganic pollutants. *International Journal of Environmental Analytical Chemistry* **86**, 233-242, doi:10.1080/03067310500247520 (2006).

38 Troupis, A., Triantis, T. M., Gkika, E., Hiskia, A. & Papaconstantinou, E. Photocatalytic reductive–oxidative degradation of Acid Orange 7 by polyoxometalates. *Applied Catalysis B: Environmental* **86**, 98-107, doi:http://dx.doi.org/10.1016/j.apcatb.2008.08.001 (2009).

39 Hiskia, A., Troupis, A. & Papaconstantinou, E. Environmental photocatalytic processes with POM. The photodecomposition of atrazine and photoreduction of metal ions from aqueous solutions. *International Journal of Photoenergy* **4**, 35-40, doi:10.1155/s1110662x02000065 (2002).

40 Gkika, E., Troupis, A., Hiskia, A. & Papaconstantinou, E. Photocatalytic reduction of chromium and oxidation of organics by polyoxometalates. *Applied Catalysis B: Environmental* **62**, 28-34, doi:10.1016/j.apcatb.2005.06.012 (2006).

41 Erjavec, B., Kaplan, R., Djinović, P. & Pintar, A. Catalytic wet air oxidation of bisphenol A model solution in a trickle-bed reactor over titanate nanotube-based catalysts. *Applied Catalysis B: Environmental* **132–133**, 342-352, doi:http://dx.doi.org/10.1016/j.apcatb.2012.12.007 (2013).

42 Chen, X. & Mao, S. S. Titanium Dioxide Nanomaterials: Synthesis, Properties, Modifications, and Applications. *Chemical Reviews* **107**, 2891-2959, doi:10.1021/cr0500535 (2007).

43 Legrini, O., Oliveros, E. & Braun, A. M. Photochemical processes for water treatment. *Chemical Reviews* **93**, 671-698, doi:10.1021/cr00018a003 (1993).

44 Li, X., Zheng, W., He, G., Zhao, R. & Liu, D. Morphology Control of TiO2Nanoparticle in Microemulsion and Its Photocatalytic Property. *ACS Sustainable Chemistry & Engineering* **2**, 288-295, doi:10.1021/sc400328u (2014).

45 Li, D., Chen, F., Jiang, D., Shi, W. & Zheng, W. Enhanced photocatalytic activity of N-doped TiO2 nanocrystals with exposed {001} facets. *Applied Surface Science* **390**, 689-695, doi:http://dx.doi.org/10.1016/j.apsusc.2016.07.149 (2016).

46 Kozhevnikov, I. *Catalysts for Fine Chemical Synthesis, Catalysis by Polyoxometalates*. (Wiley, 2002).

47 Jegatheesan, V. *et al.* in *Wastewater Treatment* 275-318 (CRC Press, 2012).

48 Marcì, G., García-López, E. I. & Palmisano, L. Heteropolyacid-Based Materials as Heterogeneous Photocatalysts. *European Journal of Inorganic Chemistry* **2014**, 21-35, doi:10.1002/ejic.201300883 (2014).

49 Black & Veatch providing engineering services for Singapore NEWater plant. *Journal American Water Works Association* **100**, 142-142 (2008).

50 Rao, D. G., Senthilkumar, R., Byrne, J. A. & Feroz, S. in *Wastewater Treatment* 1-10 (CRC Press, 2012).

51 *Used Water Treatment Process*, <https://www.pub.gov.sg/usedwater/treatment/usedwatertreatmentprocess> (

52 Rakshit, A., Anil, K., Punjabi, P. B. & Suresh, C. A. in *Wastewater Treatment* 61-106 (CRC Press, 2012).

53 Mezohegyi, G., Erjavec, B., Kaplan, R. & Pintar, A. Removal of Bisphenol A and its Oxidation Products from Aqueous Solutions by Sequential Catalytic Wet Air Oxidation and Biodegradation. *Industrial & Engineering Chemistry Research* **52**, 9301-9307, doi:10.1021/ie400998t (2013).

54 Wang, X., Zhuang, J., Peng, Q. & Li, Y. A general strategy for nanocrystal synthesis. *Nature* **437**, 121-124, doi:http://www.nature.com/nature/journal/v437/n7055/suppinfo/nature03968_S1.html (2005).

55 Ariga, K. *et al.* Challenges and breakthroughs in recent research on self-assembly. *Science and Technology of Advanced Materials* **9**, 014109, doi:10.1088/1468-6996/9/1/014109 (2008).

56 Lehmann, J., Gaita-Arino, A., Coronado, E. & Loss, D. Spin qubits with electrically gated polyoxometalate molecules. *Nat Nanotechnol* **2**, 312-317, doi:10.1038/nnano.2007.110 (2007).

57 Hill, C. L. & Prossermccartha, C. M. Homogeneous catalysis by transition-metal oxygen anion clusters. *Coordination Chemistry Reviews* **143**, 407-455, doi:10.1016/0010-8545(95)01141-b (1995).

58 Kozhevnikov, I. V. Catalysis by heteropoly acids and multicomponent polyoxometalates in liquid-phase reactions. *Chemical Reviews* **98**, 171-198, doi:10.1021/cr960400y (1998).

59 Sundermeyer, J. & Runge, D. The Bonding Capability of Imido Complex Fragments of Groups 5–7 with Regard to the Isolobal Relationship. *Angewandte Chemie International Edition in English* **33**, 1255-1257, doi:10.1002/anie.199412551 (1994).

60 Shiju, N. R. & Guliants, V. V. Recent developments in catalysis using nanostructured materials. *Applied Catalysis A: General* **356**, 1-17, doi:http://dx.doi.org/10.1016/j.apcata.2008.11.034 (2009).

61 Pan, D., Chen, J., Tao, W., Nie, L. & Yao, S. Polyoxometalate-Modified Carbon Nanotubes: New Catalyst Support for Methanol Electro-oxidation. *Langmuir* **22**, 5872-5876, doi:10.1021/la053171w (2006).

62 Kamata, K. *et al.* Efficient epoxidation of olefins with >= 99% selectivity and use of hydrogen peroxide. *Science* **300**, 964-966, doi:10.1126/science.1083176 (2003).

63 Mizuno, N., Yamaguchi, K. & Kamata, K. Epoxidation of olefins with hydrogen peroxide catalyzed by polyoxometalates. *Coordination Chemistry Reviews* **249**, 1944-1956, doi:http://dx.doi.org/10.1016/j.ccr.2004.11.019 (2005).

64 Long, D. L., Burkholder, E. & Cronin, L. Polyoxometalate clusters, nanostructures and materials: from self assembly to designer materials and devices. *Chem Soc Rev* **36**, 105-121, doi:10.1039/b502666k (2007).

65 Che, M., Fournier, M. & Launay, J. P. ANALOG OF SURFACE MOLYBDENYL ION IN MO-SIO2 SUPPORTED CATALYSTS - ISOPOLYANION MO6O-19(3)- STUDIED BY EPR AND UV-VISIBLE SPECTROSCOPY - COMPARISON WITH OTHER MOLYBDENYL COMPOUNDS. *Journal of Chemical Physics* **71**, 1954-1960, doi:10.1063/1.438549 (1979).

66 Yamase, T., Prokop, P. & Arai, Y. Photochemical studies of alkylammonium molybdates. Part 12. O→Mo charge-transfer triplet-states-initiated self-assembly to {Mo154} ring- and tube-molybdenum-blues. *Journal of Molecular Structure* **656**, 107-117, doi:http://dx.doi.org/10.1016/S0022-2860(03)00360-0 (2003).

67 Muller, A., Beckmann, E., Bogge, H., Schmidtmann, M. & Dress, A. Inorganic chemistry goes protein size: A Mo-368 nano-hedgehog initiating nanochemistry by symmetry breaking. *Angewandte Chemie-International Edition* **41**, 1162-+, doi:10.1002/1521-3773(20020402)41:7<1162::aid-anie1162>3.0.co;2-8 (2002).

68 Borrás-Almenar, J. J., Coronado, E., Müller, A. & Pope, M. *Polyoxometalate Molecular Science. [electronic resource]*. (Dordrecht : Springer Netherlands : Imprint: Springer, 2003., 2003).

69 Pope, M. T. & Müller, A. in *Polyoxometalate Chemistry From Topology via Self-Assembly to Applications* (eds Michael T. Pope & Achim Müller) 1-6 (Springer Netherlands, 2001).

70 Mizuno, N. & Misono, M. Heterogenous catalysis. *Chemical Reviews* **98**, 199-217, doi:10.1021/cr960401q (1998).

71 Baker, L. C. W. & Figgis, J. S. New fundamental type of inorganic complex: hybrid between heteropoly and conventional coordination complexes. Possibilities for

geometrical isomerisms in 11-, 12-, 17-, and 18-heteropoly derivatives. *Journal of the American Chemical Society* **92**, 3794-3797, doi:10.1021/ja00715a047 (1970).

72 Pope, M. T. Structural isomers of 1:12 and 2:18 heteropoly anions. Novel and unexpected chirality. *Inorganic Chemistry* **15**, 2008-2010, doi:10.1021/ic50162a063 (1976).

73 Baker, L. C. W. *et al.* A New General Structural Category of Heteropolyelectrolytes. Unusual Magnetic and Thermal Contraction Phenomenal. *Journal of the American Chemical Society* **88**, 2329-2331, doi:10.1021/ja00962a052 (1966).

74 Massart, R., Contant, R., Fruchart, J. M., Ciabrini, J. P. & Fournier, M. P-31 NMR-studies on molybdic and tungstic heteropolyanions - correlation between structure and chemical shift. *Inorganic Chemistry* **16**, 2916-2921, doi:10.1021/ic50177a049 (1977).

75 Evans, H. T. THE CRYSTAL STRUCTURES OF AMMONIUM AND POTASSIUM MOLYBDOTELLURATES. *Journal of the American Chemical Society* **70**, 1291-1292, doi:10.1021/ja01183a521 (1948).

76 Dexter, D. D. & Silverton, J. V. A new structural type for heteropoly anions. The crystal structure of (NH4)2H6(CeMo12O42).12H2O. *Journal of the American Chemical Society* **90**, 3589-3590, doi:10.1021/ja01015a067 (1968).

77 Baker, L. C. W. & Glick, D. C. Present general status of understanding of heteropoly electrolytes and a tracing of some major highlights in the history of their elucidation. *Chemical Reviews* **98**, 3-49, doi:10.1021/cr9603921 (1998).

78 Noespirlet, M. R., Brown, G. M., Busing, W. R. & Levy, W. A. NEUTRON DIFFRACTION STUDIES OF 3 HYDRATES OF PHOSPHOTUNGSTIC ACID. *Acta Crystallographica Section A* **31**, S80-S80 (1975).

79 Spirlet, M. R. & Busing, W. R. DODECATUNGSTOPHOSPHORIC ACID-21-WATER BY NEUTRON-DIFFRACTION. *Acta Crystallographica Section B-Structural Science* **34**, 907-910, doi:10.1107/s0567740878004306 (1978).

80 Fournier, M., Feumi-Jantou, C., Rabia, C., Herve, G. & Launay, S. Polyoxometalates catalyst materials: X-ray thermal stability study of phosphorus-containing heteropolyacids H3 +PM12 -VO40[middle dot]13-14H2O (M = Mo,W; x= 0-1). *Journal of Materials Chemistry* **2**, 971-978, doi:10.1039/JM9920200971 (1992).

81 Brown, G. M., Noespirlet, M. R., Busing, W. R. & Levy, H. A. DODECATUNGSTOPHOSPHORIC ACID HEXAHYDRATE, (H5O2+)3(PW12O403-) - TRUE STRUCTURE OF KEGGINS PENTAHYDRATE FROM SINGLE-CRYSTAL X-RAY AND NEUTRON-DIFFRACTION DATA. *Acta Crystallographica Section B-Structural Science Crystal Engineering and Materials* **33**, 1038-1046, doi:10.1107/s0567740877005330 (1977).

82 Zhao, P., Wang, J., Chen, G., Zhou, Y. & Huang, J. Phase-transfer hydroxylation of benzene with H2O2 catalyzed by a nitrile-functionalized pyridinium phosphovanadomolybdate. *Catalysis Science & Technology* **3**, 1394-1404, doi:10.1039/C3CY20796J (2013).

83 Bijelic, A. & Rompel, A. The use of polyoxometalates in protein crystallography – An attempt to widen a well-known bottleneck. *Coordination Chemistry Reviews* **299**, 22-38, doi:http://dx.doi.org/10.1016/j.ccr.2015.03.018 (2015).

84 Ji, Y., Huang, L., Hu, J., Streb, C. & Song, Y.-F. Polyoxometalate-functionalized nanocarbon materials for energy conversion, energy storage and sensor systems. *Energy & Environmental Science* **8**, 776-789, doi:10.1039/C4EE03749A (2015).

85 Dolbecq, A. D., E.; Mayer, C.R.; Mialane, P. Hybrid organic-inorganic polyoxometalate compounds: From structural diversity to applications. *Chemical Reviews* **110**, 6009 - 6048 (2010).

86 Kholdeeva, O. A., Maksimchuk, N. V. & Maksimov, G. M. Polyoxometalate-based heterogeneous catalysts for liquid phase selective oxidations Comparison of different strategies. *Catalysis Today* **157**, 107-113, doi:10.1016/j.cattod.2009.12.016 (2010).

87 Carraro, M., Fiorani, G., Sartorel, A. & Bonchio, M. in *Handbook of Advanced Methods and Processes in Oxidation Catalysis* 586-630 (IMPERIAL COLLEGE PRESS, 2014).

88 Maestre, J. M., Lopez, X., Bo, C., Poblet, J.-M. & Casañ-Pastor, N. Electronic and Magnetic Properties of α-Keggin Anions: A DFT Study of [XM12O40]n-, (M = W, Mo; X = AlIII, SiIV, PV, FeIII, CoII, CoIII) and [SiM11VO40]m- (M = Mo and W). *Journal of the American Chemical Society* **123**, 3749-3758, doi:10.1021/ja003563j (2001).

89 Hirao, H., Kumar, D., Chen, H., Neumann, R. & Shaik, S. The Electronic Structure of Reduced Phosphovanadomolybdates and the Implications on Their Use in Catalytic Oxidation Initiated by Electron Transfer. *The Journal of Physical Chemistry C* **111**, 7711-7719, doi:10.1021/jp068673c (2007).

90 Heravi, M. M., Benmorad, T., Bakhtiari, K., Bamoharram, F. F. & Oskooie, H. H. H3+xPMo12−xVxO40 (heteropolyacids)-catalyzed regioselective nitration of phenol to o-nitrophenol in heterogeneous system. *Journal of Molecular Catalysis A: Chemical* **264**, 318-321, doi:10.1016/j.molcata.2006.09.014 (2007).

91 La, K. *et al.* Preparation of H5PMo10V2O40 catalyst immobilized on spherical carbon and its application to the vapor-phase 2-propanol conversion reaction. *Korean J. Chem. Eng.* **25**, 710-713, doi:10.1007/s11814-008-0116-0 (2008).

92 Hong, U. G. *et al.* Preparation and Oxidation Catalysis of H5PMo10V2O40 Catalyst Immobilized on Nitrogen-Containing Spherical Carbon. *Catalysis Letters* **132**, 377-382, doi:10.1007/s10562-009-0118-5 (2009).

93 Neumann, R. & Khenkin, A. M. Molecular oxygen and oxidation catalysis by phosphovanadomolybdates. *Chem Commun (Camb)*, 2529-2538, doi:10.1039/b600711m (2006).

94 Pope, M. T. & Kortz, U. in *Encyclopedia of Inorganic and Bioinorganic Chemistry* (John Wiley & Sons, Ltd, 2011).

95 Li, M. *et al.* Facile synthesis of amphiphilic polyoxometalate-based ionic liquid supported silica induced efficient performance in oxidative desulfurization. *Journal of Molecular Catalysis a-Chemical* **406**, 23-30, doi:10.1016/j.molcata.2015.05.007 (2015).

96 Zubrzycki, R., Epping, J. D. & Ressler, T. Role of Vanadium and Phosphorus in Substituted Keggin-Type Heteropolyoxo Molybdates Supported on Silica SBA-15 in Selective Propene Oxidation. *ChemCatChem* **7**, 1112-1121, doi:10.1002/cctc.201402970 (2015).

97 Yang, X. *et al.* Fabrication of Core-Shell Structural SiO2@H3[PM12O40] Material and Its Catalytic Activity. *Journal of Nanomaterials* **2014**, 8, doi:10.1155/2014/835931 (2014).

98 Farsani, M. R. & Yadollahi, B. Synthesis, characterization and catalytic performance of a Fe polyoxometalate/silica composite in the oxidation of alcohols with hydrogen peroxide. *Journal of Molecular Catalysis A: Chemical* **392**, 8-15, doi:http://dx.doi.org/10.1016/j.molcata.2014.05.001 (2014).

99 Rafiee, E. & Eavani, S. Controlled immobilization of Keggin-type heteropoly acids on the surface of silica encapsulated γ-Fe2O3 nanoparticles and investigation of catalytic activity in the oxidative esterification of arylaldehydes with methanol. *Journal of Molecular Catalysis A: Chemical* **373**, 30-37, doi:http://dx.doi.org/10.1016/j.molcata.2013.02.024 (2013).

100 Mayani, S. V., Mayani, V. J. & Kim, S. W. Synthesis of molybdovanadophosphoric acid supported hybrid materials and their heterogeneous catalytic activity. *Materials Letters* **111**, 112-115, doi:http://dx.doi.org/10.1016/j.matlet.2013.08.078 (2013).

101 Guo, Y. *et al.* Microporous Polyoxometalates POMs/SiO2: Synthesis and Photocatalytic Degradation of Aqueous Organocholorine Pesticides. *Chemistry of Materials* **12**, 3501-3508, doi:10.1021/cm000074+ (2000).

102 Hua, Y. *et al.* Comparative Study of Homogeneous and Heterogeneous Photocatalytic Degradation of RhB under Visible Light Irradiation with Keggin-Type Manganese-

Substituted Catalysts. *Journal of Physical Chemistry C* **118**, 8877-8884, doi:10.1021/jp409082q (2014).

103 Lei, P. *et al.* Degradation of Dye Pollutants by Immobilized Polyoxometalate with H2O2 under Visible-Light Irradiation. *Environmental Science & Technology* **39**, 8466-8474, doi:10.1021/es050321g (2005).

104 Zou, F., Yu, R., Li, R. & Li, W. Microwave-Assisted Synthesis of HKUST-1 and Functionalized HKUST-1-@H3PW12O40: Selective Adsorption of Heavy Metal Ions in Water Analyzed with Synchrotron Radiation. *ChemPhysChem* **14**, 2825-2832, doi:10.1002/cphc.201300215 (2013).

105 Zhu, J., Shen, M.-n., Zhao, X.-j., Wang, P.-c. & Lu, M. Polyoxometalate-Based Metal–Organic Frameworks as Catalysts for the Selective Oxidation of Alcohols in Micellar Systems. *ChemPlusChem* **79**, 872-878, doi:10.1002/cplu.201400009 (2014).

106 Yan, A.-X. *et al.* Incorporating Polyoxometalates into a Porous MOF Greatly Improves Its Selective Adsorption of Cationic Dyes. *Chemistry – A European Journal* **20**, 6927-6933, doi:10.1002/chem.201400175 (2014).

107 Han, J. *et al.* Polyoxometalate immobilized in MIL-101(Cr) as an efficient catalyst for water oxidation. *Applied Catalysis A: General* **521**, 83-89, doi:http://dx.doi.org/10.1016/j.apcata.2015.10.015 (2016).

108 Kong, X.-J., Lin, Z., Zhang, Z.-M., Zhang, T. & Lin, W. Hierarchical Integration of Photosensitizing Metal–Organic Frameworks and Nickel-Containing Polyoxometalates for Efficient Visible-Light-Driven Hydrogen Evolution. *Angewandte Chemie International Edition* **55**, 6411-6416, doi:10.1002/anie.201600431 (2016).

109 Liu, X. *et al.* Selective adsorption of cationic dyes from aqueous solution by polyoxometalate-based metal–organic framework composite. *Applied Surface Science* **362**, 517-524, doi:http://dx.doi.org/10.1016/j.apsusc.2015.11.151 (2016).

110 Zhu, T.-T., Zhang, Z.-M., Chen, W.-L., Liu, Z.-J. & Wang, E.-B. Encapsulation of tungstophosphoric acid into harmless MIL-101(Fe) for effectively removing cationic dye from aqueous solution. *RSC Advances* **6**, 81622-81630, doi:10.1039/C6RA16716K (2016).

111 Xiao, Y. *et al.* Covalent immobilization of a polyoxometalate in a porous polymer matrix: a heterogeneous catalyst towards sustainability. *RSC Advances* **3**, 21544-21551, doi:10.1039/C3RA43373K (2013).

112 Yue, L. *et al.* Flexible single-layer ionic organic-inorganic frameworks towards precise nano-size separation. *Nature Communications* **7**, doi:10.1038/ncomms10742 (2016).

113 Yao, L., Lua, S. K., Zhang, L., Wang, R. & Dong, Z. Dye removal by surfactant encapsulated polyoxometalates. *Journal of Hazardous Materials* **280**, 428-435, doi:http://dx.doi.org/10.1016/j.jhazmat.2014.08.026 (2014).

114 Rengifo-Herrera, J. A., Blanco, M., Wist, J., Florian, P. & Pizzio, L. R. TiO2 modified with polyoxotungstates should induce visible-light absorption and high photocatalytic activity through the formation of surface complexes. *Applied Catalysis B: Environmental* **189**, 99-109, doi:http://dx.doi.org/10.1016/j.apcatb.2016.02.033 (2016).

115 Lauinger, S. M. *et al.* High Stability of Immobilized Polyoxometalates on TiO2 Nanoparticles and Nanoporous Films for Robust, Light-Induced Water Oxidation. *Chemistry of Materials* **27**, 5886-5891, doi:10.1021/acs.chemmater.5b01248 (2015).

116 Chen, Y., Yao, Z., Miras, H. N. & Song, Y.-F. Modular Polyoxometalate-Layered Double Hydroxide Composites as Efficient Oxidative Catalysts. *Chemistry – A European Journal* **21**, 10812-10820, doi:10.1002/chem.201501214 (2015).

117 Cuentas-Gallegos, A. K., Martínez-Rosales, R., Baibarac, M., Gómez-Romero, P. & Rincón, M. E. Electrochemical supercapacitors based on novel hybrid materials made of carbon nanotubes and polyoxometalates. *Electrochemistry Communications* **9**, 2088-2092, doi:http://dx.doi.org/10.1016/j.elecom.2007.06.003 (2007).

118 Li, S. *et al.* Green chemical decoration of multiwalled carbon nanotubes with polyoxometalate-encapsulated gold nanoparticles: visible light photocatalytic activities. *Journal of Materials Chemistry* **21**, 2282-2287, doi:10.1039/C0JM02683B (2011).

119 Wu, J. *et al.* Polyoxometalates Immobilized in Ordered Mesoporous Carbon Nitride as Highly Efficient Water Oxidation Catalysts. *ChemSusChem* **5**, 1207-1212, doi:10.1002/cssc.201100809 (2012).

120 Otero, T. F., Cheng, S. A., Coronado, E., Ferrero, E. M. & Gomez-Garcia, C. J. Functional hybrid materials containing polypyrrole and polyoxometalate clusters: Searching for high conductivities and specific charges. *Chemphyschem* **3**, 808-+, doi:10.1002/1439-7641(20020916)3:9<808::aid-cphc808>3.0.co;2-u (2002).

121 Uematsu, S., Quan, Z., Suganuma, Y. & Sonoyama, N. Reversible lithium charge–discharge property of bi-capped Keggin-type polyoxovanadates. *Journal of Power Sources* **217**, 13-20, doi:http://dx.doi.org/10.1016/j.jpowsour.2012.05.096 (2012).

122 Gómez-Romero, P. & Casañ-Pastor, N. Photoredox Chemistry in Oxide Clusters. Photochromic and Redox Properties of Polyoxometalates in Connection with Analog Solid State Colloidal Systems. *The Journal of Physical Chemistry* **100**, 12448-12454, doi:10.1021/jp953326g (1996).

123 Gómez-Romero, P. *et al.* Hybrid organic–inorganic nanocomposite materials for application in solid state electrochemical supercapacitors. *Electrochemistry*

Communications **5**, 149-153, doi:http://dx.doi.org/10.1016/S1388-2481(03)00010-9 (2003).

124 Cuentas-Gallegos, A. K., Lira-Cantú, M., Casañ-Pastor, N. & Gómez-Romero, P. Nanocomposite Hybrid Molecular Materials for Application in Solid-State Electrochemical Supercapacitors. *Advanced Functional Materials* **15**, 1125-1133, doi:10.1002/adfm.200400326 (2005).

125 Okuhara, T. & Nakato, T. Catalysis by porous heteropoly compounds. *Catalysis Surveys from Asia* **2**, 31-44, doi:10.1023/a:1019053719634 (1998).

126 ClementeLeon, M. *et al.* Toward new organic/inorganic superlattices: Keggin polyoxometalates in Langmuir and Langmuir-Blodgett films. *Langmuir* **13**, 2340-2347, doi:10.1021/la960576v (1997).

127 Xu, M. *et al.* Charge and Pressure-Tuned Surface Patterning of Surfactant-Encapsulated Polyoxometalate Complexes at the Air–Water Interface. *Langmuir* **28**, 14624-14632, doi:10.1021/la302888s (2012).

128 Li, H., Sun, H., Qi, W., Xu, M. & Wu, L. Onionlike hybrid assemblies based on surfactant-encapsulated polyoxometalates. *Angew Chem Int Ed Engl* **46**, 1300-1303, doi:10.1002/anie.200603934 (2007).

129 Nisar, A. & Wang, X. Surfactant-encapsulated polyoxometalate building blocks: controlled assembly and their catalytic properties. *Dalton Transactions* **41**, 9832-9845, doi:10.1039/c2dt30470h (2012).

130 Nisar, A., Zhuang, J. & Wang, X. Cluster-Based Self-Assembly: Reversible Formation of Polyoxometalate Nanocones and Nanotubes. *Chemistry of Materials* **21**, 3745-3751, doi:10.1021/cm901305r (2009).

131 Feigelson, L., Muszkat, L., Bir, L. & Muszkat, K. A. Dye photo-enhancement of TiO(2)-photocatalyzed degradation of organic pollutants: the organobromine herbicide bromacil. *Water Science and Technology* **42**, 275-279 (2000).

132 Gogate, P. R. & Pandit, A. B. A review of imperative technologies for wastewater treatment II: hybrid methods. *Advances in Environmental Research* **8**, 553-597, doi:10.1016/s1093-0191(03)00031-5 (2004).

133 Gogate, P. R. & Pandit, A. B. A review of imperative technologies for wastewater treatment I: oxidation technologies at ambient conditions. *Advances in Environmental Research* **8**, 501-551, doi:10.1016/s1093-0191(03)00032-7 (2004).

134 Pera-Titus, M., García-Molina, V., Baños, M. A., Giménez, J. & Esplugas, S. Degradation of chlorophenols by means of advanced oxidation processes: a general review. *Applied Catalysis B: Environmental* **47**, 219-256, doi:http://dx.doi.org/10.1016/j.apcatb.2003.09.010 (2004).

135 Neyens, E. & Baeyens, J. A review of classic Fenton's peroxidation as an advanced oxidation technique. *Journal of Hazardous Materials* **98**, 33-50, doi:http://dx.doi.org/10.1016/S0304-3894(02)00282-0 (2003).

136 Gogate, P. R. & Pandit, A. B. A review and assessment of hydrodynamic cavitation as a technology for the future. *Ultrasonics Sonochemistry* **12**, 21-27, doi:http://dx.doi.org/10.1016/j.ultsonch.2004.03.007 (2005).

137 Chong, M. N., Jin, B., Chow, C. W. K. & Saint, C. Recent developments in photocatalytic water treatment technology: A review. *Water Research* **44**, 2997-3027, doi:http://dx.doi.org/10.1016/j.watres.2010.02.039 (2010).

138 Carp, O., Huisman, C. L. & Reller, A. Photoinduced reactivity of titanium dioxide. *Progress in Solid State Chemistry* **32**, 33-177, doi:http://dx.doi.org/10.1016/j.progsolidstchem.2004.08.001 (2004).

139 Litter, M. I. Heterogeneous photocatalysis: Transition metal ions in photocatalytic systems. *Applied Catalysis B: Environmental* **23**, 89-114, doi:http://dx.doi.org/10.1016/S0926-3373(99)00069-7 (1999).

140 Kim, K.-H. & Ihm, S.-K. Heterogeneous catalytic wet air oxidation of refractory organic pollutants in industrial wastewaters: A review. *Journal of Hazardous Materials* **186**, 16-34, doi:http://dx.doi.org/10.1016/j.jhazmat.2010.11.011 (2011).

141 Sivakumar, R., Thomas, J. & Yoon, M. Polyoxometalate-based molecular/nano composites: Advances in environmental remediation by photocatalysis and biomimetic approaches to solar energy conversion. *Journal of Photochemistry and Photobiology C: Photochemistry Reviews* **13**, 277-298, doi:http://dx.doi.org/10.1016/j.jphotochemrev.2012.08.001 (2012).

142 Busca, G., Berardinelli, S., Resini, C. & Arrighi, L. Technologies for the removal of phenol from fluid streams: A short review of recent developments. *Journal of Hazardous Materials* **160**, 265-288, doi:http://dx.doi.org/10.1016/j.jhazmat.2008.03.045 (2008).

143 Rey, A. *et al.* Catalytic wet peroxide oxidation of phenol over Fe/AC catalysts: Influence of iron precursor and activated carbon surface. *Applied Catalysis B: Environmental* **86**, 69-77, doi:http://dx.doi.org/10.1016/j.apcatb.2008.07.023 (2009).

144 Pintar, A. Catalytic processes for the purification of drinking water and industrial effluents. *Catalysis Today* **77**, 451-465, doi:http://dx.doi.org/10.1016/S0920-5861(02)00385-1 (2003).

145 Levec, J. & Pintar, A. Catalytic wet-air oxidation processes: A review. *Catalysis Today* **124**, 172-184, doi:http://dx.doi.org/10.1016/j.cattod.2007.03.035 (2007).

146 Luck, F. Wet air oxidation: past, present and future. *Catalysis Today* **53**, 81-91, doi:http://dx.doi.org/10.1016/S0920-5861(99)00112-1 (1999).

147 Zhao, S., Wang, X. & Huo, M. Catalytic wet air oxidation of phenol with air and micellar molybdovanadophosphoric polyoxometalates under room condition. *Applied Catalysis B: Environmental* **97**, 127-134, doi:http://dx.doi.org/10.1016/j.apcatb.2010.03.032 (2010).

148 Jiang, C. *et al.* Oxidative desulfurization of dibenzothiophene with dioxygen and reverse micellar peroxotitanium under mild conditions. *Applied Catalysis B: Environmental* **106**, 343-349, doi:http://dx.doi.org/10.1016/j.apcatb.2011.05.038 (2011).

149 Shah, A. T. *et al.* Micelle directed synthesis of (C19H42N)(4)H-3(PW11O39) nanoparticles and their catalytic efficiency for oxidative degradation of azo dye. *Journal of Sol-Gel Science and Technology* **63**, 194-199, doi:10.1007/s10971-012-2779-6 (2012).

150 Wei, M. *et al.* Oxidation of SCN- with air and micellar polyoxoperoxometalates. *Chemosphere* **90**, 318-322, doi:10.1016/j.chemosphere.2012.07.015 (2013).

151 Weakley, T. J. R. & Malik, S. A. Heteropolyanions containing two different heteroatoms—I. *Journal of Inorganic and Nuclear Chemistry* **29**, 2935-2944, doi:http://dx.doi.org/10.1016/0022-1902(67)80126-X (1967).

152 Tsigdino, G. A. & Hallada, C. J. Molybdovanadophosphoric acids and their salts .1. Investigation of methods of preparation and characterization. *Inorganic Chemistry* **7**, 437-441, doi:10.1021/ic50061a009 (1968).

153 Komura, A., Hayashi, M. & Imanaga, H. Heteropolytungstates Containing Cobalt(II) or Cobalt(III). *Bulletin of the Chemical Society of Japan* **49**, 87-91, doi:10.1246/bcsj.49.87 (1976).

154 Harmalker, S. P., Leparulo, M. A. & Pope, M. T. Mixed-valence chemistry of adjacent vanadium centers in heteropolytungstate anions. I. Synthesis and electronic structures of mono-, di-, and trisubstituted derivatives of .alpha.-octadecatungstodiphosphate(6-) ion (.alpha.-[P2W18O62]6-). *Journal of the American Chemical Society* **105**, 4286-4292, doi:10.1021/ja00351a028 (1983).

155 Abbessi, M., Contant, R., Thouvenot, R. & Herve, G. Dawson type heteropolyanions. 1. Multinuclear (phosphorus-31, vanadium-51, tungsten-183) NMR structural investigations of octadeca(molybdotungstovanado)diphosphates .alpha.-1,2,3-[P2MM'2W15O62]n- (M, M' = Mo, V, W): syntheses of new related compounds. *Inorganic Chemistry* **30**, 1695-1702, doi:10.1021/ic00008a006 (1991).

156 Errington, R. J. *General strategies for non-aqueous polyoxometalate synthesis*. Vol. 98 (Springer, 2003).

157 Errington, R. J. in *Polyoxometalate Chemistry From Topology via Self-Assembly to Applications* (eds Michael T. Pope & Achim Müller) 7-22 (Springer Netherlands, 2001).

158 Howarth, O. W., Pettersson, L. & Andersson, I. in *Polyoxometalate Chemistry From Topology via Self-Assembly to Applications* (eds Michael T. Pope & Achim Müller) 145-159 (Springer Netherlands, 2001).

159 Gouzerh, P. & Proust, A. Main-group element, organic, and organometallic derivatives of polyoxometalates. *Chemical Reviews* **98**, 77-111, doi:10.1021/cr960393d (1998).

160 Cadot, E., Salignac, B., Dolbecq, A. & Sécheresse, F. in *Polyoxometalate Chemistry From Topology via Self-Assembly to Applications* (eds Michael T. Pope & Achim Müller) 39-53 (Springer Netherlands, 2001).

161 Müller, A., Reuter, H. & Dillinger, S. Supramolecular Inorganic Chemistry: Small Guests in Small and Large Hosts. *Angewandte Chemie International Edition in English* **34**, 2328-2361, doi:10.1002/anie.199523281 (1995).

162 Muller, A., Shah, S. Q. N., Bogge, H. & Schmidtmann, M. Molecular growth from a Mo176 to a Mo248 cluster. *Nature* **397**, 48-50 (1999).

163 Keggin, J. F. The Structure and Formula of 12-Phosphotungstic Acid. *Proceedings of the Royal Society of London. Series A* **144**, 75-100, doi:10.1098/rspa.1934.0035 (1934).

164 Diak, M. *et al.* Photoactivity of decahedral TiO2 loaded with bimetallic nanoparticles: Degradation pathway of phenol-1-13C and hydroxyl radical formation. *Applied Catalysis B: Environmental* **200**, 56-71, doi:http://dx.doi.org/10.1016/j.apcatb.2016.06.067 (2017).

165 Peng, J.-D. *et al.* Hierarchically assembled microspheres consisting of nanosheets of highly exposed (001)-facets TiO2 for dye-sensitized solar cells. *RSC Advances* **6**, 14178-14191, doi:10.1039/C5RA26307G (2016).

166 Meng, A., Zhang, J., Xu, D., Cheng, B. & Yu, J. Enhanced photocatalytic H2-production activity of anatase TiO2 nanosheet by selectively depositing dual-cocatalysts on {101} and {001} facets. *Applied Catalysis B: Environmental* **198**, 286-294, doi:http://dx.doi.org/10.1016/j.apcatb.2016.05.074 (2016).

167 Banerjee, B., Amoli, V., Maurya, A., Sinha, A. K. & Bhaumik, A. Green synthesis of Pt-doped TiO2 nanocrystals with exposed (001) facets and mesoscopic void space for photo-splitting of water under solar irradiation. *Nanoscale* **7**, 10504-10512, doi:10.1039/C5NR02097B (2015).

168 Cheng, X.-L., Hu, M., Huang, R. & Jiang, J.-S. HF-Free Synthesis of Anatase TiO2 Nanosheets with Largely Exposed and Clean {001} facets and Their Enhanced Rate

Performance As Anodes of Lithium-Ion Battery. *Acs Applied Materials & Interfaces* **6**, 19176-19183, doi:10.1021/am504971h (2014).

169 Sun, C. H. *et al.* Higher charge/discharge rates of lithium-ions across engineered TiO2 surfaces leads to enhanced battery performance. *Chemical Communications* **46**, 6129-6131, doi:10.1039/C0CC00832J (2010).

170 Nisar, A., Xu, X., Shen, S., Hu, S. & Wang, X. Noble Metal Nanocrystal-Incorporated Fullerene-Like Polyoxometalate Based Microspheres. *Advanced Functional Materials* **19**, 860-865, doi:10.1002/adfm.200801580 (2009).

171 Yin, J., Qi, L. & Wang, H. Polyoxometalate-Assisted Synthesis of TiO2 Nanoparticles and Their Applications in Aqueous Hybrid Electrochemical Capacitors. *ACS Applied Materials & Interfaces* **3**, 4315-4322, doi:10.1021/am200988q (2011).

172 Wang, Y. & Weinstock, I. A. in *Polyoxometalate Chemistry* Vol. Volume 8 *World Scientific Series in Nanoscience and Nanotechnology* 1-47 (WORLD SCIENTIFIC, 2013).

173 Cheng, F., Sajedin, S. M., Kelly, S. M., Lee, A. F. & Kornherr, A. UV-stable paper coated with APTES-modified P25 TiO2 nanoparticles. *Carbohydrate Polymers* **114**, 246-252, doi:http://dx.doi.org/10.1016/j.carbpol.2014.07.076 (2014).

174 Lee, K. S., Park, S., Lee, W. & Yoon, Y. S. Hollow Nanobarrels of α-Fe2O3 on Reduced Graphene Oxide as High-Performance Anode for Lithium-Ion Batteries. *ACS Applied Materials & Interfaces* **8**, 2027-2034, doi:10.1021/acsami.5b10342 (2016).

175 Fu, Y. *et al.* Porous hollow [small alpha]-Fe2O3@TiO2 core-shell nanospheres for superior lithium/sodium storage capability. *Journal of Materials Chemistry A* **3**, 13807-13818, doi:10.1039/C5TA02994E (2015).

176 Kim, I. T., Magasinski, A., Jacob, K., Yushin, G. & Tannenbaum, R. Synthesis and electrochemical performance of reduced graphene oxide/maghemite composite anode for lithium ion batteries. *Carbon* **52**, 56-64, doi:http://dx.doi.org/10.1016/j.carbon.2012.09.004 (2013).

177 Yang, Y. *et al.* Carbon dots supported upon N-doped TiO2 nanorods applied into sodium and lithium ion batteries. *Journal of Materials Chemistry A* **3**, 5648-5655, doi:10.1039/C4TA05611F (2015).

178 Yang, H. *et al.* Polyaniline/Polyoxometalate Hybrid Nanofibers as Cathode for Lithium Ion Batteries with Improved Lithium Storage Capacity. *The Journal of Physical Chemistry C* **117**, 17376-17381, doi:10.1021/jp401989j (2013).

179 Huang, Z. *et al.* Preparation, Characterization, and Lithium Intercalation Behavior of LiVO3 Cathode Material for Lithium-Ion Batteries. *The Journal of Physical Chemistry C* **120**, 3242-3249, doi:10.1021/acs.jpcc.5b12666 (2016).

180 Xie, A., Ma, C.-A., Wang, L. & Chu, Y. Li6V10O28, a novel cathode material for Li-ion battery. *Electrochimica Acta* **52**, 2945-2949, doi:http://dx.doi.org/10.1016/j.electacta.2006.08.069 (2007).

181 Ni, E., Uematsu, S., Quan, Z. & Sonoyama, N. Improved electrochemical property of nanoparticle polyoxovanadate K7NiV13O38 as cathode material for lithium battery. *Journal of Nanoparticle Research* **15**, 1-10, doi:10.1007/s11051-013-1732-0 (2013).

182 Chevrier, V. L. & Ceder, G. Challenges for Na-ion Negative Electrodes. *Journal of The Electrochemical Society* **158**, A1011-A1014, doi:10.1149/1.3607983 (2011).

183 Li, S. *et al.* Surface capacitive contributions: Towards high rate anode materials for sodium ion batteries. *Nano Energy* **12**, 224-230, doi:http://dx.doi.org/10.1016/j.nanoen.2014.12.032 (2015).

184 Blanco, M. & Pizzio, L. Influence of the thermal treatment on the physicochemical properties and photocatalytic degradation of 4-chlorophenol in aqueous solutions with tungstophosphoric acid-modified mesoporous titania. *Applied Catalysis A: General* **405**, 69-78, doi:http://dx.doi.org/10.1016/j.apcata.2011.07.030 (2011).

185 Brückman, K., Che, M., Haber, J. & Tatibouet, J. M. On the physicochemical and catalytic properties of H5PV2Mo10O40 supported on silica. *Catalysis Letters* **25**, 225-240, doi:10.1007/bf00816303 (1994).

186 Li, H.-l. *et al.* Improved Silanization Modification of a Silica Surface and Its Application to the Preparation of a Silica-Supported Polyoxometalate Catalyst. *Langmuir* **19**, 10409-10413, doi:10.1021/la035280l (2003).

187 Kasuga, T., Hiramatsu, M., Hoson, A., Sekino, T. & Niihara, K. Formation of Titanium Oxide Nanotube. *Langmuir* **14**, 3160-3163, doi:10.1021/la9713816 (1998).

188 Lin, C.-H., Wong, D. S.-H. & Lu, S.-Y. Layered Protonated Titanate Nanosheets Synthesized with a Simple One-Step, Low-Temperature, Urea-Modulated Method as an Effective Pollutant Adsorbent. *ACS Applied Materials & Interfaces* **6**, 16669-16678, doi:10.1021/am5035335 (2014).

189 Entradas, T. J. *et al.* Synthesis of titanate nanofibers co-sensitized with ZnS and Bi2S3 nanocrystallites and their application on pollutants removal. *Materials Research Bulletin* **72**, 20-28, doi:http://dx.doi.org/10.1016/j.materresbull.2015.07.008 (2015).

190 Harsha, N., Krishna, K. V. S., Renuka, N. K. & Shukla, S. Facile synthesis of [gamma]-Fe2O3 nanoparticles integrated H2Ti3O7 nanotubes structure as a magnetically recyclable dye-removal catalyst. *RSC Advances* **5**, 30354-30362, doi:10.1039/C5RA03722K (2015).

191 Al-Amrani, W. A., Lim, P. E., Seng, C. E. & Wan Ngah, W. S. Bioregeneration of azo dyes-loaded mono-amine modified silica in batch system: Effects of particle size and

biomass acclimation condition. *Chemical Engineering Journal* **251**, 175-182, doi:10.1016/j.cej.2014.04.070 (2014).

192 Maria Chong, A. S. & Zhao, X. S. Functionalization of SBA-15 with APTES and Characterization of Functionalized Materials. *The Journal of Physical Chemistry B* **107**, 12650-12657, doi:10.1021/jp035877+ (2003).

193 Liu, G. *et al.* Surface functionalization of zirconium dioxide nano-adsorbents with 3-aminopropyl triethoxysilane and promoted adsorption activity for bovine serum albumin. *Materials Chemistry and Physics* **176**, 129-135, doi:http://dx.doi.org/10.1016/j.matchemphys.2016.03.042 (2016).

194 She, J. *et al.* Visible light-triggered vanadium-substituted molybdophosphoric acids to catalyze liquid phase oxygenation of cyclohexane to KA oil by nitrous oxide. *Applied Catalysis B: Environmental* **182**, 392-404, doi:http://dx.doi.org/10.1016/j.apcatb.2015.09.048 (2016).

195 Arruda, L. B., Santos, C. M., Orlandi, M. O., Schreiner, W. H. & Lisboa-Filho, P. N. Formation and evolution of TiO2 nanotubes in alkaline synthesis. *Ceramics International* **41**, 2884-2891, doi:http://dx.doi.org/10.1016/j.ceramint.2014.10.113 (2015).

196 Landers, J., Gor, G. Y. & Neimark, A. V. Density functional theory methods for characterization of porous materials. *Colloids and Surfaces A: Physicochemical and Engineering Aspects* **437**, 3-32, doi:http://dx.doi.org/10.1016/j.colsurfa.2013.01.007 (2013).

197 Wei, M., Zhang, L., Xiong, Y., Li, J. & Peng, P. a. Nanopore structure characterization for organic-rich shale using the non-local-density functional theory by a combination of N2 and CO2 adsorption. *Microporous and Mesoporous Materials* **227**, 88-94, doi:http://dx.doi.org/10.1016/j.micromeso.2016.02.050 (2016).

198 Tang, Y. *et al.* Visible-light plasmonic photocatalyst anchored on titanate nanotubes: a novel nanohybrid with synergistic effects of adsorption and degradation. *RSC Advances* **2**, 9406-9414, doi:10.1039/C2RA21300A (2012).

199 Kaniou, S., Pitarakis, K., Barlagianni, I. & Poulios, I. Photocatalytic oxidation of sulfamethazine. *Chemosphere* **60**, 372-380, doi:http://dx.doi.org/10.1016/j.chemosphere.2004.11.069 (2005).

200 Hallada, C. J., Tsigdino.Ga & Hudson, B. S. Molybdovanadophosphoric acids and their salts .2. Investigation of solution properties. *Journal of Physical Chemistry* **72**, 4304-&, doi:10.1021/j100858a062 (1968).

201 Zhao, M., Ou, S. & Wu, C.-D. Porous Metal–Organic Frameworks for Heterogeneous Biomimetic Catalysis. *Accounts of Chemical Research* **47**, 1199-1207, doi:10.1021/ar400265x (2014).

202 Yanagie, H. *et al.* Anticancer activity of polyoxomolybdate. *Biomedicine & Pharmacotherapy* **60**, 349-352, doi:10.1016/j.biopha.2006.06.018 (2006).

203 Lin, C. J. *et al.* Chromate reduction by zero-valent Al metal as catalyzed by polyoxometalate. *Water research* **43**, 5015-5022 (2009).

204 Hill, C. L. Progress and challenges in polyoxometalate-based catalysis and catalytic materials chemistry. *Journal of Molecular Catalysis A: Chemical* **262**, 2-6 (2007).

205 Mylonas, A., Hiskia, A. & Papaconstantinou, E. Contribution to water purification using polyoxometalates. Aromatic derivatives, chloroacetic acids. *Journal of Molecular Catalysis a-Chemical* **114**, 191-200, doi:10.1016/s1381-1169(96)00317-2 (1996).

206 Antonaraki, S., Androulaki, E., Dimotikali, D., Hiskia, A. & Papaconstantinou, E. Photolytic degradation of all chlorophenols with polyoxometallates and H2O2. *Journal of Photochemistry and Photobiology a-Chemistry* **148**, 191-197, doi:10.1016/s1010-6030(02)00042-4 (2002).

207 Mirzaei, M., Eshtiagh-Hosseini, H., Alipour, M. & Frontera, A. Recent developments in the crystal engineering of diverse coordination modes (0–12) for Keggin-type polyoxometalates in hybrid inorganic–organic architectures. *Coordination Chemistry Reviews* **275**, 1-18, doi:http://dx.doi.org/10.1016/j.ccr.2014.03.012 (2014).

208 Liu, S. & Tang, Z. Polyoxometalate-based functional nanostructured films: Current progress and future prospects. *Nano Today* **5**, 267-281, doi:10.1016/j.nantod.2010.05.006 (2010).

209 Long, D. L., Tsunashima, R. & Cronin, L. Polyoxometalates: Building Blocks for Functional Nanoscale Systems. *Angewandte Chemie-International Edition* **49**, 1736-1758, doi:10.1002/anie.200902483 (2010).

210 Neumann, R. & Khenkin, A. M. Molecular oxygen and oxidation catalysis by phosphovanadomolybdates. *Chemical communications*, 2529-2538, doi:10.1039/b600711m (2006).

211 Khenkin, A. M. & Neumann, R. Desulfurization of Hydrocarbons by Electron Transfer Oxidative Polymerization of Heteroaromatic Sulfides Catalyzed by H5PV2Mo10O40 Polyoxometalate. *Chemsuschem* **4**, 346-348, doi:10.1002/cssc.201000402 (2011).

212 Ettedgui, J. & Neumann, R. Phenanthroline Decorated by a Crown Ether as a Module for Metallorganic-Polyoxometalate Hybrid Catalysts: The Wacker Type Oxidation of Alkenes with Nitrous Oxide as Terminal Oxidant. *Journal of the American Chemical Society* **131**, 4, doi:10.1021/ja808523n (2009).

213 Kim, K. H. & Ihm, S. K. Heterogeneous catalytic wet air oxidation of refractory organic pollutants in industrial wastewaters: A review. *Journal of Hazardous Materials* **186**, 16-34, doi:10.1016/j.jhazmat.2010.11.011 (2011).

214 Rocchiccioli-Deltcheff, C., Fournier, M., Franck, R. & Thouvenot, R. Vibrational investigations of polyoxometalates. 2. Evidence for anion-anion interactions in molybdenum(VI) and tungsten(VI) compounds related to the Keggin structure. *Inorganic Chemistry* **22**, 207-216, doi:10.1021/ic00144a006 (1983).

215 Okuyama, K. *et al.* Molecular and Crystal Structure of the Lipid-Model Amphiphile, Dioctadecyldimethylammonium Bromide Monohydrate. *Bulletin of the Chemical Society of Japan* **61**, 1485-1490, doi:10.1246/bcsj.61.1485 (1988).

216 Molinari, J. E., Nakka, L., Kim, T. & Wachs, I. E. Dynamic Surface Structures and Reactivity of Vanadium-Containing Molybdophosphoric Acid (H3+xPMo12–xVxO40) Keggin Catalysts during Methanol Oxidation and Dehydration. *ACS Catalysis* **1**, 1536-1548, doi:10.1021/cs2001362 (2011).

217 Ressler, T., Timpe, O., Girgsdies, F., Wienold, J. & Neisius, T. In situ investigations of the bulk structural evolution of vanadium-containing heteropolyoxomolybdate catalysts during thermal activation. *Journal of Catalysis* **231**, 279-291, doi:10.1016/j.jcat.2005.01.004 (2005).

218 Neumann, R. Activation of Molecular Oxygen, Polyoxometalates, and Liquid-Phase Catalytic Oxidation. *Inorganic Chemistry* **49**, 3594-3601, doi:10.1021/ic9015383 (2010).

219 Zhang, Y., Li, D. L., Chen, Y., Wang, X. H. & Wang, S. T. Catalytic wet air oxidation of dye pollutants by polyoxomolybdate nanotubes under room condition. *Applied Catalysis B-Environmental* **86**, 182-189, doi:10.1016/j.apcatb.2008.08.010 (2009).

220 Lu, T. *et al.* The loading of coordination complex modified polyoxometalate nanobelts on activated carbon fiber: a feasible strategy to obtain visible light active and highly efficient polyoxometalate based photocatalysts. *Dalton Transactions* **44**, 2267-2275, doi:10.1039/C4DT03092C (2015).

221 Lefebvre, F. in *New and Future Developments in Catalysis: Hybrid Materials, Composites, and Organocatalysts* 265-288 (2013).

222 Omwoma, S., Chen, W., Tsunashima, R. & Song, Y.-F. Recent advances on polyoxometalates intercalated layered double hydroxides: From synthetic approaches to functional material applications. *Coordination Chemistry Reviews* **258-259**, 58-71, doi:10.1016/j.ccr.2013.08.039 (2014).

223 Hasannia, S. & Yadollahi, B. Zn-Al LDH nanostructures pillared by Fe substituted Keggin type polyoxometalate: Synthesis, characterization and catalytic effect in green oxidation of alcohols. *Polyhedron* **99**, 260-265, doi:10.1016/j.poly.2015.08.020 (2015).

224 Liu, K., Yao, Z., Miras, H. N. & Song, Y. F. Facile Immobilization of a Lewis Acid Polyoxometalate onto Layered Double Hydroxides for Highly Efficient N-Oxidation of Pyridine-Based Derivatives and Denitrogenation. *ChemCatChem* **7**, 3903-3910, doi:10.1002/cctc.201500594 (2015).

225 Li, T., Wang, Z., Chen, W., Miras, H. N. & Song, Y. F. Rational Design of a Polyoxometalate Intercalated Layered Double Hydroxide: Highly Efficient Catalytic Epoxidation of Allylic Alcohols under Mild and Solvent-Free Conditions. *Chemistry - A European Journal*, doi:10.1002/chem.201604180 (2016).

226 Liu, K., Xu, Y., Yao, Z., Miras, H. N. & Song, Y. F. Polyoxometalate-Intercalated Layered Double Hydroxides as Efficient and Recyclable Bifunctional Catalysts for Cascade Reactions. *ChemCatChem* **8**, 929-937, doi:10.1002/cctc.201501365 (2016).

227 Nisar, A., Zhuang, J. & Wang, X. Construction of Amphiphilic Polyoxometalate Mesostructures as a Highly Efficient Desulfurization Catalyst. *Advanced Materials* **23**, 1130-1135, doi:10.1002/adma.201003520 (2011).

228 Ma, Z., Jin, B. & Qiu, Y. Gemini surfactants and polyoxometalates hybrid assemblies: Spacer controlled oxidative desulfurization activity. *Journal of Nanoscience and Nanotechnology* **16**, 8387-8395, doi:10.1166/jnn.2016.11770 (2016).

229 Qiao, Y. & Hou, Z. Polyoxometalate-based solid and liquid salts for catalysis. *Current Organic Chemistry* **13**, 1347-1365, doi:10.2174/138527209789055144 (2009).